# COLDz: A High Space Density of Massive Dusty Starburst Galaxies ∼1 Billion Years after the Big Bang

Dominik A. Riechers[1,2] , Jacqueline A. Hodge[3] , Riccardo Pavesi[1] , Emanuele Daddi[4] , Roberto Decarli[5] ,
Rob J. Ivison[6] , Chelsea E. Sharon[7] , Ian Smail[8] , Fabian Walter[2,9] , Manuel Aravena[10] , Peter L. Capak[11] ,
Christopher L. Carilli[9,12] , Pierre Cox[13] , Elisabete da Cunha[14,15,16] , Helmut Dannerbauer[17,18] , Mark Dickinson[19] ,
Roberto Neri[20] , and Jeff Wagg[21]

[1] Department of Astronomy, Cornell University, Space Sciences Building, Ithaca, NY 14853, USA; riechers@cornell.edu
[2] Max-Planck-Institut für Astronomie, Königstuhl 17, D-69117 Heidelberg, Germany
[3] Leiden Observatory, Leiden University, P.O. Box 9513, NL2300 RA Leiden, The Netherlands
[4] Laboratoire AIM, CEA/DSM-CNRS-Univ. Paris Diderot, Irfu/Service d'Astrophysique, CEA Saclay, Orme des Merisiers, F-91191 Gif-sur-Yvette cedex, France
[5] INAF—Osservatorio di Astrofisica e Scienza dello Spazio, via Gobetti 93/3, I-40129, Bologna, Italy
[6] European Southern Observatory, Karl-Schwarzschild-Straße 2, D-85748 Garching, Germany
[7] Yale-NUS College, #01-220, 16 College Avenue West, 138527, Singapore
[8] Centre for Extragalactic Astronomy, Department of Physics, Durham University, South Road, Durham DH1 3LE, UK
[9] National Radio Astronomy Observatory, Pete V. Domenici Array Science Center, P.O. Box O, Socorro, NM 87801, USA
[10] Núcleo de Astronomía, Facultad de Ingeniería y Ciencias, Universidad Diego Portales, Av. Ejército 441, Santiago, Chile
[11] Spitzer Science Center, California Institute of Technology, MC 220-6, 1200 East California Boulevard, Pasadena, CA 91125, USA
[12] Cavendish Astrophysics Group, University of Cambridge, Cambridge, CB3 0HE, UK
[13] Sorbonne Université, UPMC Université Paris 6 and CNRS, UMR 7095, Institut d'Astrophysique de Paris, 98bis boulevard Arago, F-75014 Paris, France
[14] Research School of Astronomy and Astrophysics, Australian National University, Canberra, ACT 2611, Australia
[15] International Centre for Radio Astronomy Research, University of Western Australia, 35 Stirling Hwy, Crawley, WA 6009, Australia
[16] ARC Centre of Excellence for All Sky Astrophysics in 3 Dimensions (ASTRO 3D), Australia
[17] Instituto de Astrofísica de Canarias, E-38205 La Laguna, Tenerife, Spain
[18] Universidad de La Laguna, Departamento de Astrofísica, E-38206 La Laguna, Tenerife, Spain
[19] NSF's National Optical-Infrared Astronomy Research Laboratory, 950 North Cherry Avenue, Tucson, AZ 85719, USA
[20] Institut de RadioAstronomie Millimétrique, 300 Rue de la Piscine, Domaine Universitaire, F-38406 Saint Martin d'Héres, France
[21] SKA Organization, Lower Withington, Macclesfield, Cheshire SK11 9DL, UK

## Abstract

We report the detection of $CO(J = 2 \rightarrow 1)$ emission from three massive dusty starburst galaxies at $z > 5$ through molecular line scans in the NSF's Karl G. Jansky Very Large Array (VLA) CO Luminosity Density at High Redshift (COLDz) survey. Redshifts for two of the sources, HDF 850.1 ($z = 5.183$) and AzTEC-3 ($z = 5.298$), were previously known. We revise a previous redshift estimate for the third source GN10 ($z = 5.303$), which we have independently confirmed through detections of CO $J = 1 \rightarrow 0$, $5 \rightarrow 4$, $6 \rightarrow 5$, and [C II] 158 $\mu$m emission with the VLA and the NOrthern Extended Millimeter Array. We find that two currently independently confirmed CO sources in COLDz are "optically dark", and that three of them are dust-obscured galaxies at $z > 5$. Given our survey area of $\sim$60 arcmin$^2$, our results appear to imply a $\sim$6–55 times higher space density of such distant dusty systems within the first billion years after the Big Bang than previously thought. At least two of these $z > 5$ galaxies show star formation rate surface densities consistent with so-called "maximum" starbursts, but we find significant differences in CO excitation between them. This result may suggest that different fractions of the massive gas reservoirs are located in the dense, star-forming nuclear regions—consistent with the more extended sizes of the [C II] emission compared to the dust continuum and higher [C II]-to-far-infrared luminosity ratios in those galaxies with lower gas excitation. We thus find substantial variations in the conditions for star formation between $z > 5$ dusty starbursts, which typically have dust temperatures that are $\sim$57% ± 25% warmer than starbursts at $z = 2–3$ due to their enhanced star formation activity.

*Unified Astronomy Thesaurus concepts:* Active galaxies (17); Galaxy evolution (594); Starburst galaxies (1570); High-redshift galaxies (734); Infrared excess galaxies (789); Observational cosmology (1146); Interstellar line emission (844); Submillimeter astronomy (1647); Millimeter astronomy (1061)

## 1. Introduction

Luminous dusty star-forming galaxies (DSFGs) represent the most intense episodes of star formation throughout cosmic history (see, e.g., Blain et al. 2002; Casey et al. 2014 for reviews). While the bulk of the population likely existed at redshifts $z \sim 1$ to 3.5 (e.g., Greve et al. 2005; Bothwell et al. 2013), a tail in their redshift distribution has been discovered over the past decade (e.g., Capak et al. 2008; Daddi et al. 2009b; Coppin et al. 2010; Smolčić et al. 2012), found to be reaching out to $z > 5$ (Riechers et al. 2010; Capak et al. 2011)

and, subsequently, $z > 6$ (Riechers et al. 2013). Dust emission in moderately luminous galaxies[22] has now been detected at $z > 8$ (Tamura et al. 2019), but no luminous DSFG is currently known at $z \geqslant 7$ (e.g., Strandet et al. 2017).

DSFGs in the $z > 5$ tail are thought to be rare, but their level of rarity is subject to debate (e.g., Béthermin et al. 2015, 2017; Asboth et al. 2016; Ivison et al. 2016; see also Simpson et al. 2014, 2020;

---

[22] In this work, galaxies with infrared luminosities of $10^{11} < L_{IR} < 10^{12} L_\odot$ are considered to be moderately luminous, and those above are considered to be luminous.

Dudzevičiūtė et al. 2020). A significant challenge in determining the space density of such sources is the difficulty in finding them in the first place. Given their distance, classical techniques combining optical and radio identifications have been largely unsuccessful due to the faintess or lack of detection at these wavelengths, commonly leading to misidentifications given the significant positional uncertainties of the classical sub/millimeter single-dish surveys in which they are the most easily seen (e.g., Chapman et al. 2005; Cowie et al. 2009, and references therein). Also, due to the strong negative K correction at sub/millimeter wavelengths (e.g., Blain et al. 2002), it remained challenging to pick out the most distant DSFGs among the much more numerous specimens at $z < 3.5$. Over the past decade, many of these challenges were overcome through new observational capabilities and selection techniques, such as direct identifications based on interferometric observations of the dust continuum emission (e.g., Younger et al. 2007; Smolčić et al. 2012; Simpson et al. 2014, 2015; Brisbin et al. 2017; Stach et al. 2018; see also earlier works by, e.g., Downes et al. 1999; Dannerbauer et al. 2002), redshift identifications through targeted molecular line scans (e.g., Weiß et al. 2009; Riechers 2011), and target selection based on sub/millimeter colors or flux limits (e.g., Cox et al. 2011; Riechers et al. 2013, 2017; Dowell et al. 2014; Vieira et al. 2010; Weiß et al. 2013 ). Nevertheless, all of the current studies only provide incomplete censuses of the $z > 5$ DSFG population due to biases in the selection, limited sensitivity in the parent sub/millimeter surveys, and incomplete redshift confirmations of existing samples.

Here, we aim to follow a complementary approach to more traditional studies that builds on the finding that all luminous DSFGs appear to contain large molecular gas reservoirs that fuel their star formation, and to be significantly metal-enriched, leading to bright CO line emission. As such, these systems are preferentially picked up by panoramic molecular line scan surveys, and they may even dominate among detections at the highest redshifts, where most other galaxy populations may exhibit only weak CO emission (e.g., Pavesi et al. 2019) due to a combination of lower characteristic galaxy masses at earlier epochs, lower metallicity (which is thought to lead to an increase in the $\alpha_{CO}$ conversion factor, i.e., a lower CO luminosity per unit molecular gas mass; see Bolatto et al. 2013 for a review), and possibly lower CO line excitation (e.g., Daddi et al. 2015). Support for this idea was provided by the detection of the "optically dark"[23] $z = 5.183$ DSFG HDF 850.1 in a molecular line scan in the *Hubble* Deep Field North (Walter et al. 2012), but the survey area of $\sim0.5$ arcmin$^2$ was too small to make more quantitative statements regarding the broader properties and space density of such sources.[24]

To build upon this encouraging finding, and to provide a better understanding of the true space densities of the most distant DSFGs, we here study the properties of dusty starbursts at $z > 5$ found in sensitive molecular line scans, based on the $\sim60$ arcmin$^2$ Very Large Array (VLA) CO Luminosity Density at High Redshift (COLDz) survey data (Pavesi et al. 2018b; Riechers et al. 2019, hereafter P18, R19).[25] We report the detection of CO($J = 2 \rightarrow 1$) emission from three systems

initially detected in 850 $\mu$m and 1.1 mm continuum surveys, HDF 850.1, AzTEC-3, and GN10 (Hughes et al. 1998; Pope et al. 2005; Scott et al. 2008), two of which had previous correct redshift identifications through CO measurements (AzTEC-3 and HDF 850.1; Riechers et al. 2010; Capak et al. 2011; Walter et al. 2012). We also report higher-resolution observations of AzTEC-3 and HDF 850.1 and detailed follow-up observations of the third system, the "optically dark" galaxy GN10, as well as CO line excitation modeling for the sample. Our analysis is used to constrain the evolution of dust temperature with redshift and the space density of $z > 5$ DSFGs. In Section 2, we describe all observations, the results of which are given in Section 3. Section 4 provides a detailed analysis of our findings for the COLDz $z > 5$ DSFG sample, which are discussed in the context of all currently known $z > 5$ DSFGs in Section 5. A summary and conclusions are provided in Section 6. We provide additional line parameters and an alternative spectral energy distribution fit for GN10 and additional observations of two $z > 4$ dusty starbursts, GN20.2a and b, in Appendices A–C, respectively. We use a concordance, flat $\Lambda$CDM cosmology throughout, with $H_0 = 69.6$ km s$^{-1}$ Mpc$^{-1}$, $\Omega_M = 0.286$, and $\Omega_\Lambda = 0.714$ (Bennett et al. 2014).

## 2. Data

### 2.1. Very Large Array

#### 2.1.1. COLDz Survey Data

CO($J = 2 \rightarrow 1$) line emission ($\nu_{rest} = 230.5380$ GHz) toward HDF 850.1, AzTEC-3, and GN10 was detected in molecular line scans with the VLA within the COLDz survey data (project IDs: 13A-398 and 14A-214; PI: Riechers). A detailed description of the data is given by P18. In brief, COLDz targeted two regions in the COSMOS and GOODS-North survey fields at 35 and 34 GHz (corresponding to $\sim$8.7 mm), covering areas of $\sim$9 and 51 arcmin$^2$ in 7- and 57-point mosaics with the VLA, respectively. Observations were carried out under good *Ka* band weather conditions for a total of 324 hr between 2013 January 26 and 2015 December 18 in the D and DnC array configurations, as well as reconfigurations between the C, DnC, and D arrays. The correlator was set up with two intermediate frequency bands (IFs) of 4 GHz bandwidth (dual polarization) each in 3-bit mode, centered at the frequencies indicated above. Gaps between individual 128 MHz sub-bands were mitigated through frequency switching. The radio quasars J1041+0610 and J1302+5748 were observed for complex gain calibration and regular pointing corrections in the COSMOS and GOODS-North fields, respectively. The absolute flux scale was derived based on observations of 3C 286.

Data reduction and imaging were performed with the CASA 4.1 package,[26] using the data pipeline version 1.2.0. Imaging the data with natural baseline weighting yields typical clean beam sizes of 2″5, with variations between individual pointings and across the large bandwidth. Typical rms noise levels are 60 and 100–200 $\mu$Jy beam$^{-1}$ per 4 MHz ($\sim$35 km s$^{-1}$) binned channel in the COSMOS and GOODS-North fields, respectively. At the positions of GN10 and AzTEC-3 (for which maps based on these data are shown in the

---

[23] See, e.g., Calabrò et al. (2019) and references therein for a more detailed discussion of the nature of such sources at lower redshifts.

[24] Also, while its redshift was not known at the time, the telescope pointing was chosen to include HDF 850.1. As such, this measurement did not constitute an unbiased discovery of an "optically dark" source.

[25] See http://coldz.astro.cornell.edu for additional information.

[26] https://casa.nrao.edu

following sections), the rms noise is 51 and 18 $\mu$Jy beam$^{-1}$ per 76 and 60 MHz ($\sim$623 and 491 km s$^{-1}$) binned channel at beam sizes of $1\rlap{.}''95 \times 1\rlap{.}''67$ and $2\rlap{.}''46 \times 2\rlap{.}''26$, respectively.

### 2.1.2. GN10 CO(J = 1 → 0) Follow-up

We observed CO($J = 1 \rightarrow 0$) line emission toward GN10 using the VLA (project ID: 16A-015; PI: Riechers). Observations were carried out under good Ku band weather conditions for a total of 11 hr during five tracks in the C array between 2016 February 2 and March 6. Two IFs with 1 GHz bandwidth (dual polarization) each in 8-bit mode were centered at 13.977 and 17.837 GHz (corresponding to 2.1 and 1.7 cm, respectively) to cover the redshifted HCN, HCO$^+$, and HNC($J = 1 \rightarrow 0$) and CO($J = 1 \rightarrow 0$) lines in GN10 ($\nu_{\rm rest} = 88.6318$, 89.1885, 90.6636, and 115.2712 GHz). Observations were carried out in short cycles, spending between $\sim$330 and $\sim$470 s on source, bracketed by scans spending $\sim$75 s on the gain calibrator J1302 +5748. Pointing was performed on the gain calibrator approximately once per hour. The absolute flux scale was derived based on observations of 3C 286.

Data reduction and imaging were performed with the CASA 5.4.2 package. Imaging the data with natural baseline weighting yields a clean beam size of $1\rlap{.}''75 \times 1\rlap{.}''28$ at an rms noise level of 21 $\mu$Jy beam$^{-1}$ over 40 MHz (656 km s$^{-1}$) at the CO($J = 1 \rightarrow 0$) line frequency. The rms noise near the HCN($J = 1 \rightarrow 0$) frequency is $\sim$27 $\mu$Jy beam$^{-1}$ over 4 MHz (85 km s$^{-1}$). Imaging the data over the entire line-free bandwidth of 2.012 GHz yields an rms noise level of 1.49 $\mu$Jy beam$^{-1}$ at a beam size of $2\rlap{.}''10 \times 1\rlap{.}''54$.

### 2.1.3. GN10 1.3 cm and 6.6 mm Continuum Follow-up

We observed continuum emission at 22.8649 GHz ($K$ band) and 45.6851 GHz ($Q$ band) toward GN10 (corresponding to 1.3 cm and 6.6 mm, respectively), using the VLA (project ID: AR693; PI: Riechers).[27] Observations were carried out under good K and $Q$ band observing conditions for a total of 44 hr between 2009 July 19 and 2010 January 5. $K$-band observations were conducted for four tracks in the C array, totaling 28 hr, and $Q$-band observations were conducted for two tracks in the D array, totaling 16 hr. All observations used the previous generation correlator, covering two IFs of 50 MHz bandwidth (dual polarization) each at the tuning frequency and 300 MHz ($K$ band) or 50 MHz ($Q$ band) above, respectively, in quasi-continuum mode. Observations in the C (D) array were carried out in short cycles, spending 150 s (200 s) on source, bracketed by scans spending 60 s on the gain calibrator J13028 +57486. Pointing was performed on the gain calibrator approximately once per hour. The absolute flux scale was derived based on observations of 3C 286.

Data reduction and imaging were performed with the AIPS package.[28] Imaging the data with natural baseline weighting yields clean beam sizes of $1\rlap{.}''15 \times 1\rlap{.}''01$ and $1\rlap{.}''82 \times 1\rlap{.}''68$ at rms noise levels of 44 and 58 $\mu$Jy beam$^{-1}$ over 100 MHz in the K and $Q$ bands, respectively.

### 2.1.4. HDF 850.1 CO(J = 2 → 1) High-resolution Follow-up

We observed CO($J = 2 \rightarrow 1$) line emission toward HDF 850.1 at higher spatial resolution using the VLA (project

ID: 16A-014; PI: Riechers). Observations were carried out under good $Ka$ band weather conditions for a total of 8.8 hr during four tracks in the C array between 2016 February 3 and 20. Two IFs with 4 GHz bandwidth (dual polarization) each in 3-bit mode were centered at 34 GHz (corresponding to 8.8 mm) to cover the same frequency range as the D array observations of the main survey. Gaps between sub-bands were mitigated through frequency switching, using the same two setups with a relative shift of 16 MHz, as in the D array. Observations were carried out in short cycles, spending $\sim$300 s on source, bracketed by scans spending $\sim$100 s on the gain calibrator J1302+5748. Pointing was performed on the gain calibrator approximately once per hour. The absolute flux scale was derived based on observations of 3C 286.

Data reduction and imaging were performed with the CASA 5.4.2 package. Imaging the data with natural baseline weighting yields a clean beam size of $0\rlap{.}''71 \times 0\rlap{.}''68$ at an rms noise level of 32.4 $\mu$Jy beam$^{-1}$ over 66 MHz (530 km s$^{-1}$) at the CO($J = 2 \rightarrow 1$) line frequency.

## 2.2. NOrthern Extended Milllimeter Array (NOEMA)

### 2.2.1. GN10 CO(J = 6 → 5) Follow-up

We observed CO($J = 6 \rightarrow 5$) line emission ($\nu_{\rm rest} = 691.4731$ GHz) toward GN10 using NOEMA (project ID: X–5; PI: Riechers). Observations were carried out under good 3 mm weather conditions for four tracks in the A configuration between 2014 February 18 and 24, using six antennas (baseline range: 67–760 m). This yielded a total time of 13.8 hr (16500 visibilities) on source. Receivers were tuned to 109.7037 GHz (corresponding to 2.7 mm). The correlator was set up with a bandwidth of 3.6 GHz (dual polarization).

Data reduction and imaging were performed with the GILDAS package. Imaging the data with natural or uniform baseline weighting yields clean beam sizes of $0\rlap{.}''82 \times 0\rlap{.}''71$ or $0\rlap{.}''63 \times 0\rlap{.}''59$ at rms noise levels of 73 or 90 $\mu$Jy beam$^{-1}$ over 700 MHz (1912 km s$^{-1}$), respectively. Imaging the data with natural weighting over the entire line-free bandwidth of 2.9 GHz yields an rms noise level of 31.6 $\mu$Jy beam$^{-1}$.

### 2.2.2. GN10 [CII]($^2P_{3/2}$ → $^2P_{1/2}$) Follow-up

We observed [C II] 158 $\mu$m line emission ($\nu_{\rm rest} = 1900.5369$ GHz) toward GN10 using NOEMA (project ID: W14FH; PI: Riechers). Observations were carried out under good 0.9 mm weather conditions for one track in the C configuration on 2015 April 15, using six antennas (baseline range: 21–172 m). This yielded a total time of 1.9 hr (2249 visibilities) on source. Receivers were tuned to 301.524 GHz (corresponding to 1.0 mm). The correlator was set up with a bandwidth of 3.6 GHz (dual polarization).

Data reduction and imaging were performed with the GILDAS package. Imaging the data with natural or uniform baseline weighting yields clean beam sizes of $1\rlap{.}''01 \times 0\rlap{.}''84$ or $0\rlap{.}''81 \times 0\rlap{.}''76$ at rms noise levels of 0.62 or 0.71 mJy beam$^{-1}$ over 800 MHz (795 km s$^{-1}$), respectively. Imaging the data with natural or uniform weighting over the entire line-free bandwidth of 2.31 GHz yields rms noise levels of 324 or 365 $\mu$Jy beam$^{-1}$.

---

[27] These observations were tuned to the CO($J = 1 \rightarrow 0$) and CO($J = 2 \rightarrow 1$) emission lines at the previous, incorrect redshift estimate.
[28] https://www.iram.fr/IRAMFR/GILDAS/

### 2.2.3. GN10 1.2 and 2 mm Continuum Follow-up

We observed continuum emission at 137.057 GHz (2.2 mm)[29] and 250.5 GHz (1.2 mm) toward GN10 using NOEMA (project IDs: T047 and T0B7; PI: Riechers). Observations were carried out under good weather conditions for three tracks between 2009 June 4 and September 21 in the D configuration with five antennas (baseline range: 19–94 m) at 2 mm and for two tracks on 2011 January 23 and 24 in the A configuration with six antennas (baseline range: 51–665 m) at 1.2 mm. This yielded a total of 7.1 and 3.7 hr (17,040 and 8940 visibilities) six-antenna-equivalent on-source time at 2 and 1.2 mm, respectively. Observations at 2 mm were carried out with the previous generation correlator with a bandwidth of 1 GHz (dual polarization). Observations at 1.2 mm were carried out with a bandwidth of 3.6 GHz (dual polarization).

Data reduction and imaging were performed with the GILDAS package. Imaging the 2 mm data with natural baseline weighting yields a clean beam size of $3\rlap{.}''7 \times 3\rlap{.}''2$ at an rms noise level of 95 $\mu$Jy beam$^{-1}$ over 1 GHz bandwidth. Imaging the 1.2 mm data with natural or uniform baseline weighting yields clean beam sizes of $0\rlap{.}''45 \times 0\rlap{.}''38$ or $0\rlap{.}''38 \times 0\rlap{.}''33$ at rms noise levels of 0.35 or 0.43 mJy beam$^{-1}$ over 3.6 GHz, respectively.

### 2.2.4. Archival: GN10 CO(J = 5 → 4)

Serendipitous CO(J = 5 → 4) line emission ($\nu_{\rm rest}$ = 576.2679 GHz) was observed toward GN10 using NOEMA. These observations, taken from Daddi et al. (2009a), did not target GN10, which was offset by $9\rlap{.}''7$ or $19\rlap{.}''7$ from the phase center for different tracks, yielding primary beam attenuation factors of 1.08 or 1.30, respectively. Observations were carried out under good 3 mm weather conditions for four tracks in the B, C, and D configurations between 2008 May 4 and 2009 January 5, using six antennas (baseline range: 15–411 m). This yielded a total time of 14.6 hr (25186 visibilities) on source. Receivers were tuned to 91.375 GHz (corresponding to 3.3 mm). The correlator was set up with a bandwidth of 1 GHz (dual polarization).

We adopted the data reduction performed by Daddi et al. (2009a) but re-imaged the data with the GILDAS package. Imaging the data with natural baseline weighting yields a clean beam size of $2\rlap{.}''64 \times 1\rlap{.}''90$ at an rms noise level of 66.6 $\mu$Jy beam$^{-1}$ over 365.753 MHz (1200 km s$^{-1}$) at the phase center (96 $\mu$Jy beam$^{-1}$ at the position of GN10). Imaging the data over the line-free bandwidth yields an rms noise level of 55 $\mu$Jy beam$^{-1}$.

### 2.2.5. AzTEC-3 CO(J = 5 → 4) High-resolution Follow-up

We observed CO(J = 5 → 4) line emission ($\nu_{\rm rest}$ = 576.2679 GHz) toward AzTEC-3 using NOEMA (project ID: U0D0; PI: Riechers). Observations were carried out under good 3 mm weather conditions for two tracks in the A configuration between 2011 January 19 and February 4, using six antennas (baseline range: 100–760 m). We also used previous observations (project ID: T–F; PI: Riechers) carried out for one track in the C configuration on 2010 April 1, using six antennas (baseline range: 15–176 m; see Riechers et al. 2010 for additional details). This yielded a total time of 8.8 hr

(10560 visibilities; 5340 in A configuration) on source. Receivers were tuned to 91.558 GHz (corresponding to 3.3 mm). The correlator was set up with a bandwidth of 3.6 GHz (dual polarization).

Data reduction and imaging were performed with the GILDAS package. Imaging the combined data with natural baseline weighting yields a clean beam size of $2\rlap{.}''21 \times 1\rlap{.}''43$ at an rms noise level of 64 $\mu$Jy beam$^{-1}$ over 280 MHz (917 km s$^{-1}$). Imaging the A configuration data only with uniform baseline weighting yields a clean beam size of $1\rlap{.}''39 \times 0\rlap{.}''85$ at an rms noise level of 96 $\mu$Jy beam$^{-1}$ over 260 MHz (852 km s$^{-1}$). Imaging the A (A+C) configuration data with natural weighting over the entire line-free bandwidth of 3.34 GHz yields an rms noise level of 24.8 (18.8) $\mu$Jy beam$^{-1}$.

### 2.2.6. AzTEC-3 1.2 mm Continuum Follow-up

We observed continuum emission at 250.0 GHz (1.2 mm) toward AzTEC-3 using NOEMA (project ID: U0D0; PI: Riechers). Observations were carried out under good weather conditions for three tracks between 2011 January 25 and February 03 in the A configuration with six antennas (baseline range: 100–760 m) at 1.2 mm. This yielded a total of 9.3 hr (11160 visibilities) on source. Observations were carried out with a bandwidth of 3.6 GHz (dual polarization).

Data reduction and imaging were performed with the GILDAS package. Imaging the data with natural or uniform baseline weighting yields clean beam sizes of $0\rlap{.}''62 \times 0\rlap{.}''25$ or $0\rlap{.}''53 \times 0\rlap{.}''24$ at rms noise levels of 162 or 187 $\mu$Jy beam$^{-1}$ over 3.6 GHz, respectively.

## 3. Results
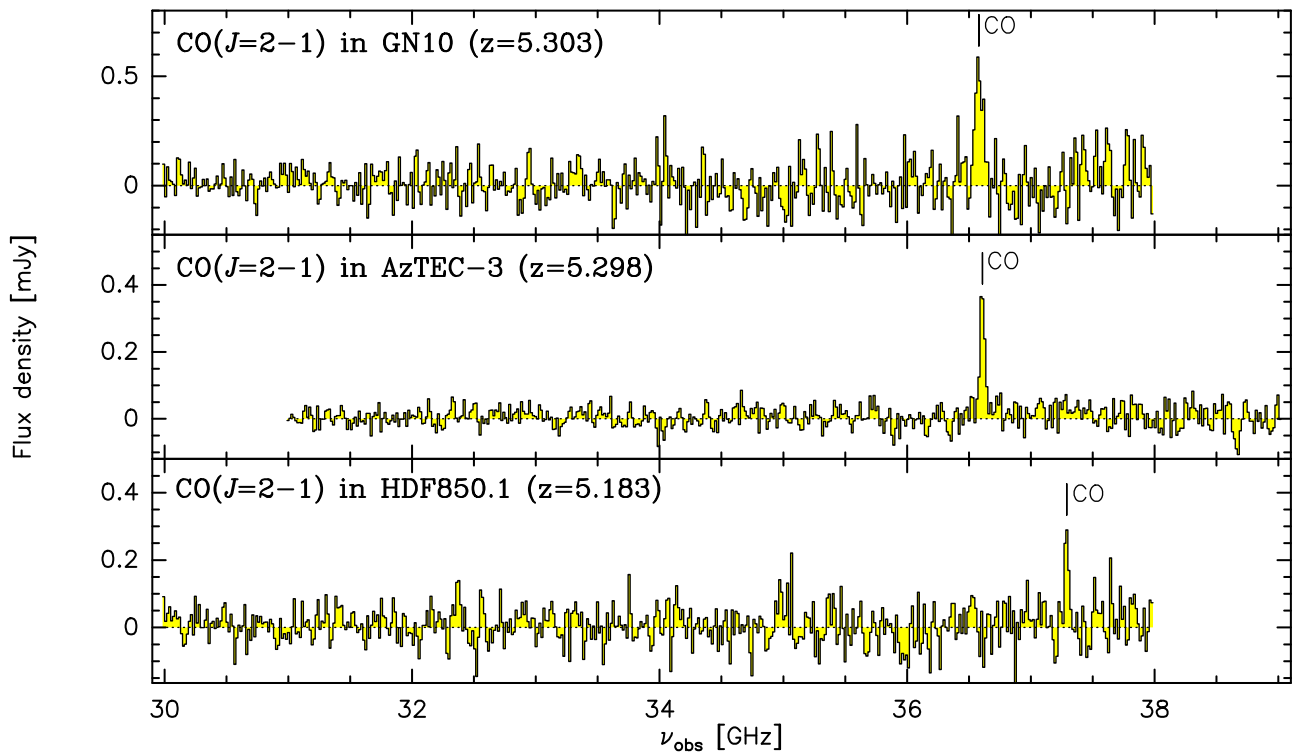
### 3.1. COLDz Molecular Line Scan CO(J = 2 → 1) Detections

Our CO search in the COSMOS and GOODS-North fields carried out as part of the COLDz molecular line scan survey (P18, R19) yielded four matches[30] with massive dusty star-forming galaxies initially selected in single-dish bolometer surveys with the JCMT at 850 $\mu$m or 1.1 mm. One of the matches at 6.1$\sigma$ significance corresponds to CO(J = 1 → 0) emission associated with the z = 2.488 DSFG GN19 (Pope et al. 2005; Riechers et al. 2011a; Ivison et al. 2011; see P18) and will not be discussed further here. Two of the matches correspond to CO(J = 2 → 1) emission in the z = 5.183 and z = 5.298 DSFGs HDF 850.1 and AzTEC-3 (Figure 1 and Table 1), which are detected at 5.3$\sigma$ and 14.7$\sigma$ significance, respectively. From Gaussian fits to the line spectra and moment-0 maps, we find CO(J = 2 → 1) line FWHM of d$v_{\rm FWHM}$ = (490 ± 140) and (424 ± 44) km s$^{-1}$ for HDF 850.1 and AzTEC-3, yielding line fluxes of $I_{\rm CO(2-1)}$ = (0.148 ± 0.057) and (0.199 ± 0.018) Jy km s$^{-1}$, respectively. These flux levels are consistent with previous, lower-significance detections within the relative uncertainties (Riechers et al. 2010; Walter et al. 2012).

Unexpectedly at the time of observation, we also detect an emission line at 8.6$\sigma$ significance toward the DSFG GN10 (Figure 1), previously thought to be at z = 4.042 based on a single line detection at 3 mm and photometric redshift information (Daddi et al. 2009a). We identify this line with

---

[29] These observations were tuned to the CO(J = 6 → 5) emission line at the previous, incorrect redshift estimate.

[30] One match was found in the COSMOS field, and three matches were found in the ~5.7 times larger GOODS-North field.

**Figure 1.** COLDz molecular line scan CO($J = 2 \rightarrow 1$) spectra (histograms) of $z > 5$ DSFGs, shown at 16 MHz ($\sim$130 km s$^{-1}$) spectral resolution. Line emission in GN10, AzTEC-3, and HDF 850.1 is detected at 8.6$\sigma$, 14.7$\sigma$, and 5.3$\sigma$ significance, respectively.

CO($J = 2 \rightarrow 1$) emission at $z = 5.303$, which implies that the line detected by Daddi et al. (2009a) corresponds to CO($J = 5 \rightarrow 4$) emission, rather than CO($J = 4 \rightarrow 3$) emission. This identification was confirmed through the successful detection of CO($J = 1 \rightarrow 0$), CO($J = 6 \rightarrow 5$), and [C II] emission at the same redshift, as described in detail below (see Figures 2 and 3). This explains why our earlier attempts to detect CO($J = 1 \rightarrow 0$), CO($J = 2 \rightarrow 1$), and CO($J = 6 \rightarrow 5$) emission at $z = 4.042$ (see Section 2) were unsuccessful.

### 3.2. GN10 Follow-up

#### 3.2.1. Continuum Emission

We detect strong continuum emission toward GN10 at 1.2 and 1.0 mm and weak emission between 2.2 mm and 1.9 cm (see Figure 4 and Table 2). The flux keeps decreasing between 0.9 and 1.9 cm and is >4–8 times lower than at 21 cm. This suggests that the emission detected up to 0.9 cm (i.e., rest frame 1.4 mm) likely still corresponds to thermal emission, but nonthermal emission may start to significantly contribute at 1.9 cm (i.e., rest frame 3.0 mm; see Figure 8). The continuum emission is spatially resolved along the major axis at 1.2 mm by our observations with a synthesized beam size of $\sim$0.″35. By fitting two-dimensional Gaussian profiles to the emission in the visibility plane, we find a size of (0.″25 ± 0.″07) × (0.″10 ± 0.″11), which corresponds to (1.6 ± 0.4) × (0.6 ± 0.6) kpc$^2$. A circular Gaussian fit provides a full width at half power (FWHP) diameter of 0.″18 ± 0.″05, or (1.1 ± 0.3) kpc. Due to the agreement of the 1.2 mm flux with a previous measurement at lower spatial resolution at a close wavelength (Dannerbauer et al. 2008; see Table 2), and given the baseline coverage down to $\sim$50 m, it appears unlikely that the 1.2 mm size measurement is biased toward low values due to missing emission. Fits to the lower-

resolution ($\sim$0.″75 beam size) data at 1.0 mm however suggest a size of (0.″58 ± 0.″12) × (0.″50 ± 0.″10), corresponding to (3.6 ± 0.7) × (3.1 ± 0.6) kpc$^2$, or a circular FWHP diameter of 0.″53 ± 0.″08 (3.3 ± 0.5 kpc$^2$). The uncertainties for this measurement may be limited by interferometric seeing due to phase noise (which is not factored into the fitting errors), such that we treat the 1.0 mm size measurement as an upper limit only in the following sections. We however note that, in principle, the dust emission at shorter wavelengths could appear more extended due to an increasing dust optical depth as well, as discussed further in Section 4. Also, the source shape could significantly deviate from a Gaussian shape (such as a higher-index Sérsic profile; see, e.g., discussion by Hodge et al. 2016), such that more complex fitting procedures could yield different findings.

Despite its strong dust continuum emission at sub/millimeter wavelengths, GN10 remains undetected up to an observed-frame wavelength of 2.2 $\mu$m, rendering it a "$K$-band dropout" (also see discussion by Wang et al. 2009; Daddi et al. 2009a, and references therein). Even sensitive space-based imaging up to 1.6 $\mu$m with the WFC3 camera on the Hubble Space Telescope (HST) from the CANDELS survey (Grogin et al. 2011) yields no hint of emission due to dust obscuration (Figure 4), but mid-infrared continuum emission is detected with Spitzer/IRAC longward of 3.6 $\mu$m (corresponding to $\sim$5700 Å in the rest frame; Dickinson & GOODS Team 2004; Giavalisco et al. 2004) at the position of the millimeter-wave dust continuum emission (Figure 4). Thus, the stellar light in the "optically dark" galaxy GN10 is not entirely obscured by dust.[31]

---

[31] Contributions to the rest-frame optical light by a dust-obscured active galactic nucleus in GN10 cannot be ruled out; see discussion in Section 4.

**Table 1**
Line Fluxes and Line Luminosities for COLDz $z > 5$ DSFGs

| Line | GN10 | | AzTEC-3 | | HDF 850.1 | | References |
|---|---|---|---|---|---|---|---|
| | COLDz.GN.0 | | COLDz.COS.0[d] | | COLDz.GN.31 | | |
| (J2000.0)[a] | (12:36:33.45,+62:14:08.85) | | (10:00:20.70,+02:35:20.50) | | (12:36:52.07,+62:12:26.49) | | |
| | $I_{\rm line}$ (Jy km s$^{-1}$) | $L'_{\rm line}$ ($10^{10}$ K km s$^{-1}$ pc$^2$) | $I_{\rm line}$ (Jy km s$^{-1}$) | $L'_{\rm line}$ ($10^{10}$ K km s$^{-1}$ pc$^2$) | $I_{\rm line}$ (Jy km s$^{-1}$) | $L'_{\rm line}$ ($10^{10}$ K km s$^{-1}$ pc$^2$) | |
| CO($J = 1 \rightarrow 0$) | $0.054 \pm 0.017$[b] | $5.44 \pm 1.68$ | | | <0.09 | <8.9 | 1, 2 |
| CO($J = 2 \rightarrow 1$) | $0.295 \pm 0.035$ | $7.47 \pm 0.90$ | $0.199 \pm 0.018$ | $5.02 \pm 0.44$ | $0.148 \pm 0.057$ | $3.62 \pm 1.39$ | 1, 3 |
| | | | $0.23 \pm 0.04$ | $5.84 \pm 0.37$ | $0.17 \pm 0.04$ | $4.15 \pm 0.98$ | 4, 5 |
| CO($J = 5 \rightarrow 4$) | $0.86 \pm 0.20$ | $3.46 \pm 0.81$ | $0.97 \pm 0.09$ | $3.92 \pm 0.38$ | $0.50 \pm 0.10$ | $1.96 \pm 0.39$ | 1, 6, 5 |
| | | | $0.92 \pm 0.09$ | $3.70 \pm 0.37$ | | | 4 |
| CO($J = 6 \rightarrow 5$) | $0.52 \pm 0.11$ | $1.46 \pm 0.31$ | $1.36 \pm 0.19$ | $3.82 \pm 0.45$ | $0.39 \pm 0.10$ | $1.06 \pm 0.27$ | 1, 4, 5 |
| CO($J = 7 \rightarrow 6$) | | | | | $0.35 \pm 0.05$ | $0.70 \pm 0.10$ | 7 |
| CO($J = 16 \rightarrow 15$) | | | <0.22 | <0.09 | | | 8 |
| OH($^2\Pi_{1/2}\, J = 3/2 \rightarrow 1/2$) | | | $1.44 \pm 0.13$ | $0.57 \pm 0.05$ | | | 8 |
| [CI]($^3P_2 \rightarrow {}^3P_1$) | | | | | $0.14 \pm 0.05$ | $0.28 \pm 0.10$ | 7 |
| [CII]($^2P_{3/2} \rightarrow {}^2P_{1/2}$) | $17.6 \pm 1.9$ | $6.55 \pm 0.71$ | $8.21 \pm 0.29$ | $3.05 \pm 0.11$ | $9.9 \pm 1.0$ | $3.56 \pm 0.36$ | 1, 8, 9 |
| | $16.2 \pm 1.4$[c] | $6.01 \pm 0.53$ | $7.8 \pm 0.4$ | $2.90 \pm 0.15$ | $14.6 \pm 0.3$ | $5.25 \pm 0.11$ | 1, 10, 5 |
| [NII]($^3P_1 \rightarrow {}^3P_0$) | | | $0.46 \pm 0.16$ | $0.31 \pm 0.11$ | | | 10 |

**Notes.**
[a] CO($J = 2 \rightarrow 1$) centroid positions adopted from P18.
[b] A Gaussian fit to the line profile formally suggests $0.054 \pm 0.010$ Jy km s$^{-1}$, but we consider these uncertainties to be somewhat optimistic due to the increasing noise level toward the blue edge of the bandpass. We thus adopt more conservative error bars based on the signal-to-noise ratio of the detection in the moment-0 map.
[c] Main component only.
[d] Alternative ID: AS2COS0059.1 (Simpson et al. 2020).

**References**—[1] this work; [2] Wagg et al. (2007); [3] Pavesi et al. (2018b); [4] Riechers et al. (2010); [5] Walter et al. (2012); [6] Daddi et al. (2009a); [7] Decarli et al. (2014); [8] Riechers et al. (2014a); [9] Neri et al. (2014); [10] Pavesi et al. (2016).
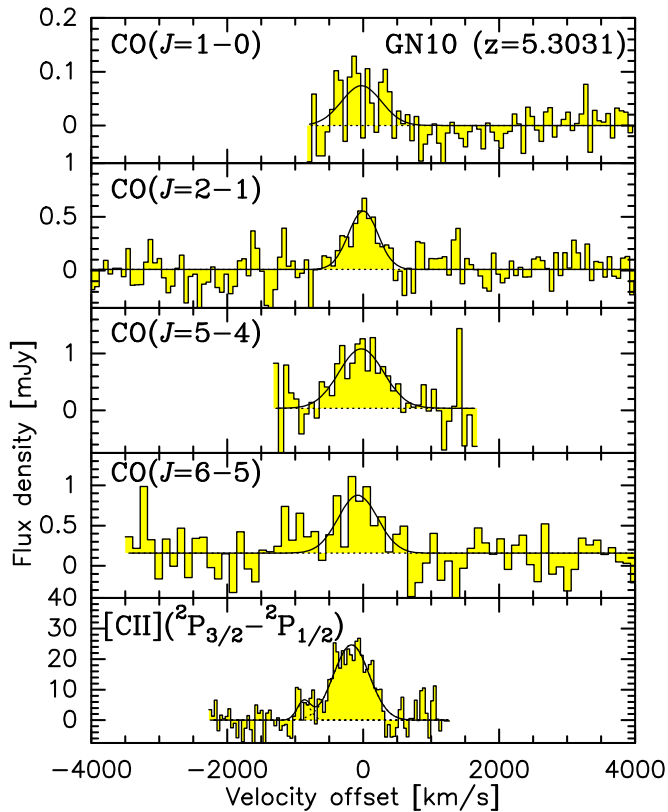
**Figure 2.** VLA and NOEMA line spectra of GN10 ($z = 5.3031$; histograms) and Gaussian fits to the line profiles (black curves). Spectra are shown at resolutions of 66, 66, 75, 109, and 40 km s$^{-1}$ (4, 8, 23, 40, and 40 MHz; *top to bottom*), respectively. Continuum emission ($9.55 \pm 0.73$ mJy) has been subtracted from the [C II] spectrum only.

### 3.2.2. Line Emission

We successfully detect CO($J = 1 \rightarrow 0$), CO($J = 2 \rightarrow 1$), CO($J = 5 \rightarrow 4$), CO($J = 6 \rightarrow 5$), and [C II] emission toward GN10 at $3.3\sigma$, $8.6\sigma$, $6.9\sigma$, $7.3\sigma$, and $18.1\sigma$ peak significance, respectively (Figures 2 and 3 and Table 1; see Appendix A for further details). In combination, these lines provide an unambiguous redshift identification. We extract the parameters of all emission lines from Gaussian fitting to the line profiles. All CO lines are fit with single Gaussian functions (see Appendix A for further details). We find line peak fluxes of $S_{\text{line}} = (74 \pm 13)$, $(544 \pm 63)$, $(1046 \pm 205)$, and $(719 \pm 144)\,\mu$Jy at FWHM line widths of $dv_{\text{FWHM}} = (687 \pm 144)$, $(512 \pm 72)$, $(772 \pm 220)$, and $(681 \pm 173)$ km s$^{-1}$ for the CO $J = 1 \rightarrow 0$, $2 \rightarrow 1$, $5 \rightarrow 4$, and $6 \rightarrow 5$ lines, respectively. The [C II] line is fit with two Gaussian components, yielding $S_{\text{line}} = (24.7 \pm 1.6)$ and $(6.0 \pm 4.2)$ mJy and $dv_{\text{FWHM}} = (617 \pm 67)$ and $(227 \pm 243)$ km s$^{-1}$ for the red- and blueshifted components, respectively. The parameters of the secondary component thus are only poorly constrained, and we report [C II] fluxes including and excluding this component in the following. It may correspond to a gas outflow, or a close-by minor companion galaxy to the DSFG.[32] Considering only the main [C II] component, the widths of all lines are consistent within the relative uncertainties.

Assuming the same widths as for the CO($J = 2 \rightarrow 1$) line, we find $3\sigma$ upper limits of $<0.017$ Jy km s$^{-1}$ for the HCN, HCO$^+$, and HNC($J = 1 \rightarrow 0$) lines.[33] This implies HCN, HCO$^+$, and HNC to CO line luminosity ratio limits of the order of $<40\%$, which are only modestly constraining given the expectation of a few percent to $\sim20\%$ ratios for distant starburst galaxies (see, e.g., Riechers et al. 2007; Oteo et al. 2017b, and references therein).

The integrated line fluxes and line luminosities derived from these measurements are summarized in Table 1, together with those of AzTEC-3 and HDF 850.1, including values from the literature. The CO($J = 2 \rightarrow 1$) flux of GN10 reported here is somewhat lower than that found by P18 using a different extraction method. Here, we adopt our updated value for consistency. Given the more complex velocity profile of the [C II] line in GN10, we adopt the CO($J = 2 \rightarrow 1$)-based redshift of $z = 5.3031 \pm 0.0006$ in the following. This measurement agrees within $1\sigma$ with the CO($J = 1 \rightarrow 0$), CO($J = 5 \rightarrow 4$), and CO($J = 6 \rightarrow 5$)-based measurements.[34] The systemic velocity centroid of the [C II] line is slightly blueshifted, but emission is detected across the same velocity range as in the CO $J = 1 \rightarrow 0$ to $6 \rightarrow 5$ lines. The line peak offset thus is likely mainly due to internal variations in the [C II]/CO ratio.

By fitting two-dimensional Gaussian profiles to the [C II] emission, we find a size of $(1.\!''04 \pm 0.\!''30) \times (0.\!''19 \pm 0.\!''10)$. This corresponds to $(6.5 \pm 1.9) \times (1.2 \pm 0.6)$ kpc$^2$. Attempting to fit the CO($J = 6 \rightarrow 5$) emission observed at a comparable spatial resolution yields a size of $0.\!''42 \times < 0.\!''25$ ($2.6 \times < 1.6$ kpc$^2$), but the fit does not converge well due to the moderate signal-to-noise ratio of the detection. A circular fit is consistent with a point source within the uncertainties. This suggests that the [C II] emission is resolved at least along the major axis and that it appears to be more spatially extended than the mid-$J$ CO and dust emission, which are consistent with having a comparable spatial extent within the current uncertainties. The [C II] emission shows a significant spatial velocity gradient across the line emission in the main component alone (see Figure 3).

### 3.3. AzTEC-3 Follow-up

#### 3.3.1. Continuum Emission

We detect strong continuum emission toward AzTEC-3 at 1.2 mm and weak emission at 3.3 mm at the same peak position (Figure 5). We measure a continuum flux of $(118 \pm 25)\,\mu$Jy at 3.3 mm (i.e., rest frame 520 $\mu$m) from the A configuration data, which is consistent with the $3\sigma$ upper limit of $<0.12$ mJy obtained from the C configuration data (Riechers et al. 2010). The emission appears unresolved in the A configuration data. Combining both data sets, we find a final 3.3 mm flux of $(126 \pm 19)\,\mu$Jy. The continuum emission is spatially resolved along the major axis at 1.2 mm by our observations with a synthesized beam size of $\sim0.\!''25$. By fitting two-dimensional Gaussian profiles in the image plane, we find a size of $(0.\!''45 \pm 0.\!''14) \times (0.\!''05^{+0.\!''21}_{-0.\!''05})$, which corresponds to $(2.8 \pm 0.9) \times (0.3^{+1.3}_{-0.3})$ kpc$^2$, and we measure

---

[32] The CO($J = 6 \rightarrow 5$) spectrum shows an excess positive signal at velocities comparable to the secondary [C II] component, but its significance is too low to permit further analysis.

---

[33] The observations also cover the CCH($N = 1 \rightarrow 0$) line, which is not detected down to a comparable limit (see Appendix A).

[34] The redshift uncertainties for the CO($J = 1 \rightarrow 0$), CO($J = 2 \rightarrow 1$), CO($J = 5 \rightarrow 4$), CO($J = 6 \rightarrow 5$), and [C II] lines from fitting Gaussian functions to the line profiles are 60, 30, 71, 70, and 24 km s$^{-1}$, respectively.
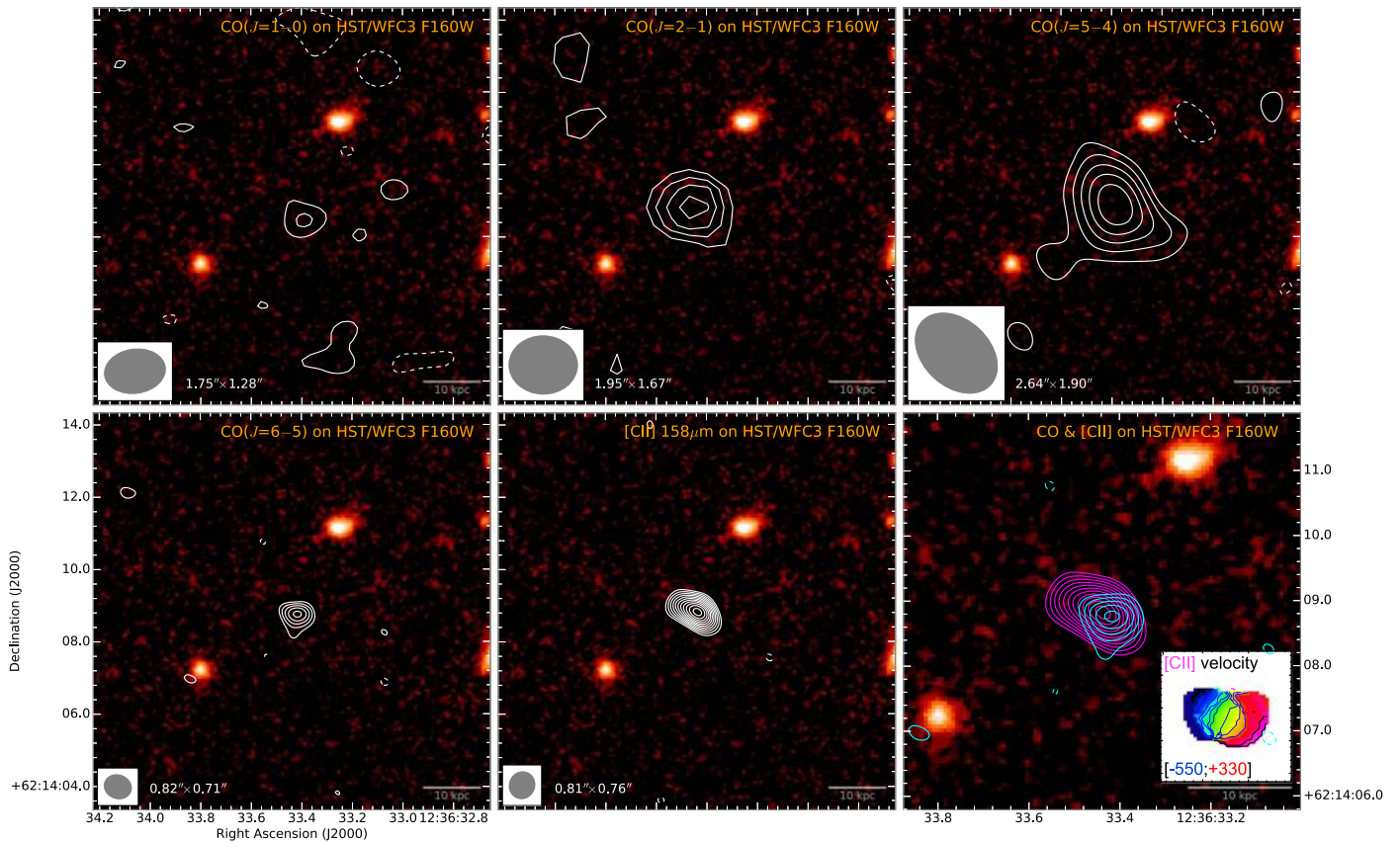
**Figure 3.** Velocity-integrated line contour maps overlaid on an HST/WFC3 F160W continuum image from the CANDELS survey toward GN10. Contour maps are averaged over 656, 623, 1199, 1913, and 795 km s$^{-1}$, respectively. Contours start at $\pm 2\sigma$, $3\sigma$, $2\sigma$, $3\sigma$, and $4\sigma$, and they are shown in steps of $1\sigma = 21$, 51, 96, 73, and 710 $\mu$Jy beam$^{-1}$ for the first five panels, respectively. The synthesized beam size is indicated in the bottom left corner of each panel where applicable. The last panel shows CO($J = 6 \rightarrow 5$) (cyan) and [C II] (magenta) contours and is zoomed-in by a factor of 1.8 compared to all other panels. The inset in the last panel shows a velocity map over the central 880 km s$^{-1}$ of the [C II] emission (created from 80 km s$^{-1}$ velocity channels and adopting a detection threshold of 9 mJy beam$^{-1}$). Velocity contours are shown in steps of 50 km s$^{-1}$.

a 1.2 mm flux of $(3.67 \pm 0.56)$ mJy. This is consistent with the size of the 1.0 mm continuum emission of $(0.''40 \pm 0.''04) \times (0.''17^{+0.''08}_{-0.''17})$ and the dust spectral energy distribution shape found by Riechers et al. (2014a). A circular Gaussian fit in the visibility plane (which gives more weight to the longer baseline data) yields an FWHP diameter of $0.''14 \pm 0.''04$, or $(0.9 \pm 0.2)$ kpc, but a flux of only $(2.75 \pm 0.29)$ mJy. Taken at face value, this appears to suggest that $\sim$75% of the emission emerges from a compact region within the 2.5–3 kpc diameter dust reservoir.[35]
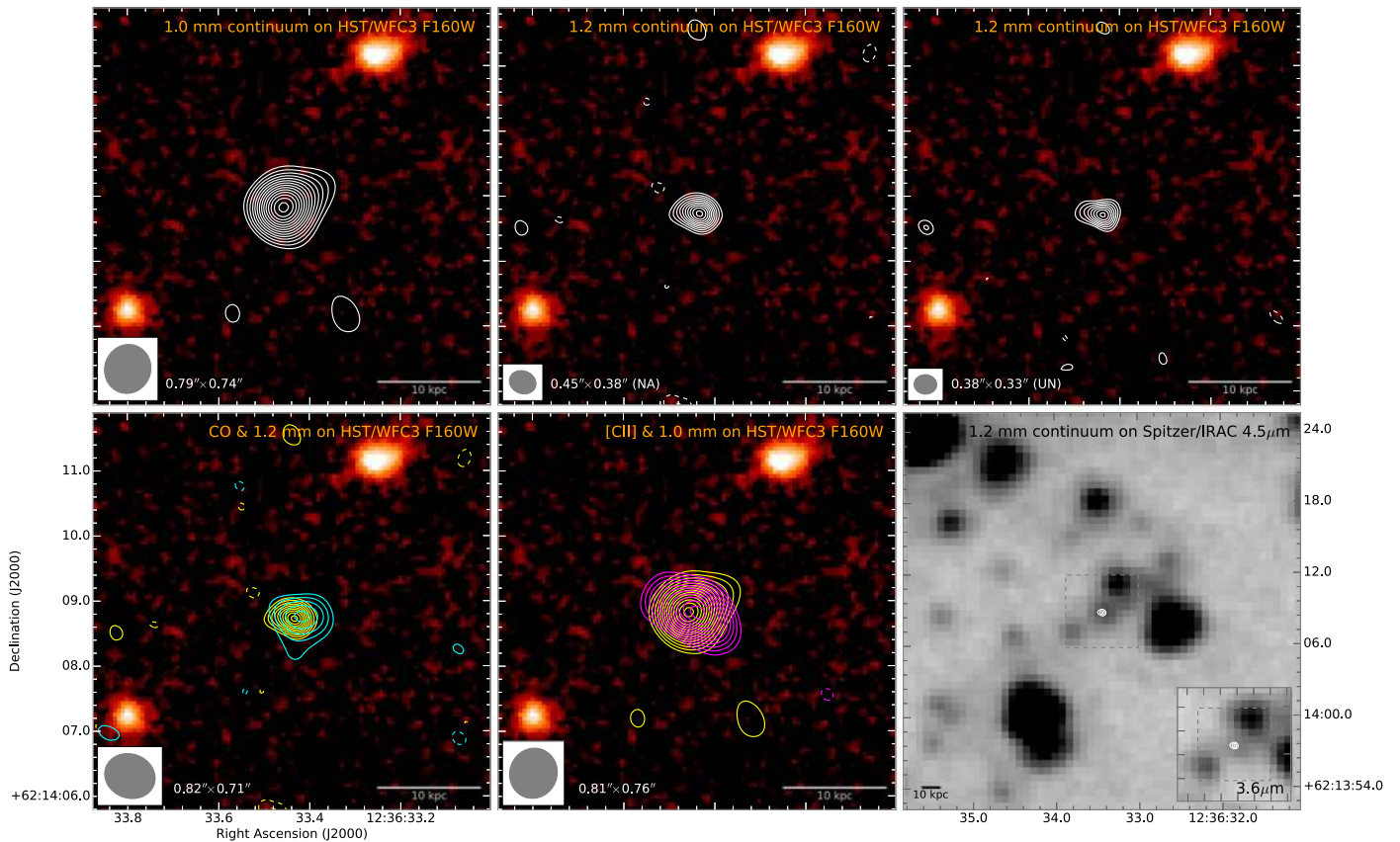
### 3.3.2. Line Emission

We detect CO($J = 5 \rightarrow 4$) emission toward AzTEC-3 at $15.0\sigma$ peak significance (Figure 5; CO $J = 2 \rightarrow 1$ and $6 \rightarrow 5$ are also shown for reference). From a circular Gaussian fit in the visibility plane to the moment-0 map, we find a line flux of $I_{CO(5-4)} = (0.97 \pm 0.09)$ Jy km s$^{-1}$, which is consistent with a previous measurement by Riechers et al. (2010). From Gaussian fitting to the line profile (Figure 6; CO $J = 2 \rightarrow 1$ and $6 \rightarrow 5$ and [C II] are also shown for reference), we obtain a peak flux of $S_{CO(5-4)} = (1.88 \pm 0.14)$ mJy and an FWHM of $dv_{FWHM} = (396 \pm 37)$ km s$^{-1}$, which is consistent with the

---

[35] We caution that the source shape could significantly deviate from a Gaussian shape, such that the structure and size of the dust emission could be more complex than indicated by these findings.

previously measured values and those found for the CO($J = 2 \rightarrow 1$) and [C II] lines (Riechers et al. 2014a). The line may show an excess in its red wing that is not captured well by the Gaussian fit, but the significance of this feature is only moderate. A circular Gaussian fit in the visibility plane over the entire width of the emission of 917 km s$^{-1}$ (280 MHz) suggests an FWHP source diameter of $0.''44 \pm 0.''17$, which corresponds to $(2.8 \pm 1.1)$ kpc. This is comparable to the size of the 1.0 and 1.2 mm continuum emission. Fitting the source over 524 km s$^{-1}$ (160 MHz) to capture only the main component of the emission, we find $0.''57 \pm 0.''15$, which corresponds to $(3.5 \pm 0.9)$ kpc. This is comparable to the size of the [C II] emission of $(0.''63 \pm 0.''09) \times (0.''34^{+0.''10}_{-0.''15})$ found by Riechers et al. (2014a) over a similar velocity range (466 km s$^{-1}$). There appears to be a small spatial offset between the peaks of the CO($J = 5 \rightarrow 4$) and [C II] emission (which is consistent with the dust continuum peak; Figure 5). However, this offset becomes insignificant ($\lesssim 1\sigma$) when excluding the red CO line wing, i.e., when considering comparable velocity ranges, which results in a shift of the peak position by $\sim 0.''1$ ($\lesssim 2\sigma$ significance shift) relative to the broader velocity range. If confirmed, the emission in the red line wing thus may correspond to a spatially offset kinematic component, but additional data are required to investigate this finding in more detail.

**Figure 4.** Rest-frame far-infrared (FIR) continuum contour maps at an observed-frame wavelength of 1.0 (top left panel) and 1.2 mm (top middle and right panels; imaged using natural and uniform baseline weighting, respectively), overlaid on an HST/WFC3 F160W continuum image toward GN10. Contours start at $\pm\,4\sigma$, $3\sigma$, and $3\sigma$, and they are shown in steps of $1\sigma = 365$, 352, and 421 $\mu$Jy beam$^{-1}$, respectively. The synthesized beam size is indicated in the bottom left corner of each panel where applicable. The $4\sigma$ peaks south of GN10 in the top left panel are due to sidelobe residuals given imperfections in the calibration. The bottom panels show overlays of 1.2 and 1.0 mm continuum (yellow) with CO($J = 6 \rightarrow 5$) and [C II] emission (bottom left and middle panels; same contours as in Figure 3) and 1.2 mm contours (natural weighting; shown in steps of $\pm\,4\sigma$) on Spitzer/IRAC 3.6 (inset) and 4.5 $\mu$m images (bottom right panel). The dashed gray box in the last panel indicates the same area as shown in the other panels.

## 3.4. HDF 850.1 Follow-up

We have imaged the CO($J = 2 \rightarrow 1$) emission in HDF 850.1 at $\sim$3 times higher resolution than in the COLDz main survey data and previous observations by Walter et al. (2012). At a linear resolution of $\sim$4.3 kpc, the emission is detected at $4.5\sigma$ peak significance, and also spatially resolved (Figure 7). A two-dimensional Gaussian fit to the emission in the image plane suggests a deconvolved size of $(1.''06 \pm 0.''23) \times (0.''49 \pm 0.''05)$, which corresponds to $(6.7 \pm 1.5) \times (3.1 \pm 0.3)$ kpc$^2$. Given the moderate signal-to-noise ratio of the detection, the real uncertainty on the minor axis extent of the emission is likely of the order of 50%. The orientation and size of the emission are consistent with that seen in the rest-frame 158 $\mu$m dust continuum emission (Neri et al. 2014), and the peak positions agree to within one synthesized beam size. No stellar light is detected at the position of the CO emission even in deep HST/WFC3 imaging at an observed-frame of 1.6 $\mu$m due to dust obscuration, which independently confirms HDF 850.1 as an "optically dark" galaxy. It is strongly blended with a bright foreground elliptical galaxy in Spitzer/IRAC imaging longward of 3.6 $\mu$m, such that only moderately constrained upper limits can be obtained (see also discussion by Pope et al. 2006).

## 4. Analysis of Individual Sources

### 4.1. Properties of GN10

Given the new redshift identification of GN10, here, we describe in detail the determination of its key physical properties.

#### 4.1.1. Spectral Energy Distribution

To extract physical parameters from the spectral energy distribution (SED) of GN10, we have followed two approaches, as summarized in Figure 8 and Table 3. First, we have fit the far-infrared (FIR) peak of the SED with a modified blackbody (MBB) routine, where the MBB is joined to a smooth power law with slope $\alpha$ toward observed-frame mid-infrared wavelengths (e.g., Blain et al. 2003, and references therein). The dust temperature $T_{\rm dust}$, dust emissivity parameter $\beta_{\rm IR}$, and the wavelength $\lambda_0$, where the optical depth becomes unity, are used as fitting parameters. In addition, the flux $f_{158\mu\rm m}^{\rm rest}$ at rest frame 158 $\mu$m is used as a normalization parameter. The Markov Chain Monte Carlo (MCMC) and nested sampling package EMCEE (Foreman-Mackey et al. 2013) is used to explore the posterior parameter distribution. By integrating the fitted functions, we obtain far-infrared ($L_{\rm FIR}$) and total infrared ($L_{\rm IR}$) luminosities, which we then use to

**Table 2**
GN10 Continuum Photometry

| Wavelength ($\mu$m) | Flux Density[a] (mJy) | Telescope | Reference |
|---|---|---|---|
| 0.435 | $<12 \times 10^{-6}$ | HST/ACS | 1 |
| 0.606 | $<9 \times 10^{-6}$ | HST/ACS | 1 |
| 0.775 | $<18 \times 10^{-6}$ | HST/ACS | 1 |
| 0.850 | $<27 \times 10^{-6}$ | HST/ACS | 1 |
| 1.25 | $<42 \times 10^{-6}$ | Subaru/MOIRCS | 1 |
| 1.60 | $<15 \times 10^{-6}$ | HST/NICMOS | 1 |
| 2.15 | $<42 \times 10^{-6}$ | Subaru/MOIRCS | 1 |
| 3.6 | $(1.29 \pm 0.13) \times 10^{-3}$ | Spitzer/IRAC | 2 |
| 4.5 | $(2.07 \pm 0.21) \times 10^{-3}$ | Spitzer/IRAC | 2 |
| 5.8 | $(2.96 \pm 0.37) \times 10^{-3}$ | Spitzer/IRAC | 2 |
| 8.0 | $(5.30 \pm 0.53) \times 10^{-3}$ | Spitzer/IRAC | 2 |
| 16 | $(17.5 \pm 6.3) \times 10^{-3}$ | Spitzer/IRS | 2 |
| 24 | $(33.4 \pm 7.9) \times 10^{-3}$ | Spitzer/MIPS | 2 |
| 70 | $<2.0$ | Spitzer/MIPS | 3 |
| 110 | $<1.52$ | Herschel/PACS | 2 |
| 160 | $<5.3$ | Herschel/PACS | 2 |
| 160 | $<30$ | Spitzer/MIPS | 3 |
| 250[b] | $9.8 \pm 4.1$ | Herschel/SPIRE | 2 |
| 350[b] | $8.9 \pm 4.2$ | Herschel/SPIRE | 2 |
| 500[b] | $12.4 \pm 2.8$ | Herschel/SPIRE | 2 |
| 850 | $12.9 \pm 2.1$ | JCMT/SCUBA | 3 |
|  | $11.3 \pm 1.6$ | JCMT/SCUBA | 3 |
| 870 | $12.0 \pm 1.4$ | SMA | 3 |
| 995 | $9.55 \pm 0.73$ | NOEMA | 4 |
| 1200 | $5.25 \pm 0.60$ | NOEMA | 4 |
| 1250 | $5.0 \pm 1.0$ | NOEMA | 3 |
| 2187 | $0.28 \pm 0.17$ | NOEMA | 4 |
| 2733 | $0.148 \pm 0.032$ | NOEMA | 4 |
| 3280 | $<0.27$ | NOEMA | 5 |
| 6560 | $<0.174$ | VLA | 4 |
| 8820 | $(8.1 \pm 4.2) \times 10^{-3}$ | VLA | 4 |
| 13100 | $<0.132$ | VLA | 4 |
| 18850 | $(4.3 \pm 1.5) \times 10^{-3}$ | VLA | 4 |
| 210000 | $(35.8 \pm 4.1) \times 10^{-3}$ | VLA | 2, 3 |

**Notes.**
[a] Limits are $3\sigma$.
[b] De-blended fluxes. Uncertainties do not account for confusion noise, which formally is 5.9, 6.3, and 6.8 mJy ($1\sigma$) at 250, 350, and 500 $\mu$m, respectively (Nguyen et al. 2010), but also is reduced though the de-blending process.
**References**—[1] Wang et al. (2009) and references therein; [2] Liu et al. (2018); [3] Dannerbauer et al. (2008) and references therein; [4] this work; [5] Daddi et al. (2009a).

determine dust-obscured star formation rates, SFR$_{IR}$, under the assumption of a Kennicutt (1998) conversion for a Chabrier (2003) stellar initial mass function. By adopting a mass absorption coefficient of $\kappa_\nu = 2.64\ \mathrm{m^2\ kg^{-1}}$ at 125 $\mu$m (Dunne et al. 2003), we also estimate a dust mass $M_{dust}$ from the fits, finding a high value in excess of $10^9\ M_\odot$ (see Table 3).

We also fit the full optical to radio wavelength photometry of GN10 using the Code Investigating GALaxy Emission (CIGALE; Noll et al. 2009; Serra et al. 2011), using a broad range of star formation histories and metallicities and a standard dust attenuation law (Calzetti 2001). We find parameters that are broadly consistent with the MBB fitting where applicable. Due to its high level of dust obscuration, GN10 remains undetected shortward of an observed-frame of 3.6 $\mu$m (rest frame $\sim$5700 Å), which leaves some parameters only poorly constrained. Thus, we only adopt the stellar mass

$M_\star$ from the CIGALE fit in the following sections. We find a high value in excess of $10^{11}\ M_\odot$, i.e., $\sim$100 times the dust mass, which we consider to be reliable to within a factor of a few (see Table 3).[36]

From our MBB fits, we find that the dust turns optically thick at $\sim$170 $\mu$m (i.e., between an observed-frame wavelength of 1.0 and 1.2 mm; see Table 3), similar to the values found for other $z > 4$ DSFGs (see, e.g., Riechers et al. 2013, 2014a; Simpson et al. 2017), such that dust extinction may impact the observed [C II] line luminosity at 158 $\mu$m. This would be in agreement with a larger apparent dust emission size at 1.0 mm than at 1.2 mm, as found above due to dust optical depth effects, but higher-resolution 1.0 mm imaging is required to further investigate this finding. We also find a moderately high dust temperature of $(50 \pm 9)$ K.[37]

### 4.1.2. Star Formation Rate Surface Density

Based on the 1.2 mm size of GN10, we find a source surface area of $(0.79 \pm 0.44)\ \mathrm{kpc^2}$ $(0.99 \pm 0.30\ \mathrm{kpc^2}$; second quoted values indicate results from circular Gaussian fits). Its flux thus corresponds to a source-averaged rest-frame brightness temperature of $T_b = (24.9 \pm 8.1)$ K $(20.0 \pm 2.9$ K) at rest frame 190 $\mu$m, or $50\% \pm 18\%$ $(40\% \pm 9\%)$ of the dust temperature obtained from SED fitting. This suggests that the dust emission is likely at least moderately optically thick and that it fills the bulk of the source surface area within its inferred size. From our SED fit, we determine a dust optical depth of $\tau_{190\ \mu m} = 0.69 \pm 0.29$ (i.e., $1 - \exp(-\tau_{190\ \mu m}) = 50\%^{+13\%}_{-17\%}$), which is consistent with this finding. Using the value of $L_{IR}$ derived in the previous subsection, this size corresponds to an IR luminosity surface density of $\Sigma_{IR} = (7.5 \pm 4.4) \times 10^{12}\ L_\odot\ \mathrm{kpc^{-2}}$ $(6.0 \pm 2.0 \times 10^{12}\ L_\odot\ \mathrm{kpc^{-2}})$ or an SFR surface density of $\Sigma_{SFR} = (750 \pm 440)\ M_\odot\ \mathrm{yr^{-1}\ kpc^{-2}}$ $(600 \pm 210\ M_\odot\ \mathrm{yr^{-1}\ kpc^{-2}})$.

### 4.1.3. Dynamical Mass Estimate

To obtain a dynamical mass estimate from our resolved line emission map, we have fitted visibility-plane dynamical models of a rotating disk to the [C II] emission from GN10 (Figure 9; see Pavesi et al. 2018a for further details on the modeling approach). Rotating circular disk models of the [C II] emission are generated through the *KinMSpy* code (Davis et al. 2013), super-imposed on continuum emission, which is fitted by a circular two-dimensional Gaussian function.[38] The fitting parameters are the disk center position, systemic velocity, gas dispersion, FWHM size of the spatial light profile of the Gaussian disk, maximum velocity, velocity scale length, inclination, position angle, and line flux. The continuum flux and FWHM size are determined based on the emission in the line-free channels. The fitting method employs the MCMC and nested sampling techniques as implemented in EMCEE (Foreman-Mackey et al. 2013) and MULTINEST for python

---

[36] See Appendix B for an alternative $M_\star$ value obtained with the MAGPHYS code, which we consider to be consistent within the uncertainties. See also Liu et al. (2018) for a discussion of the potential uncertainties associated with the determination of $M_\star$ for the most distant DSFGs, and see Simpson et al. (2014, 2017) for a more detailed discussion of the uncertainties of $M_\star$ estimates for DSFGs in general.
[37] See Appendix B for an alternative, luminosity-averaged $T_{dust}$ value obtained by fitting multiple dust components with the MAGPHYS code.
[38] We include the continuum emission in the fitting to properly account for uncertainties associated with continuum modeling and subtraction.
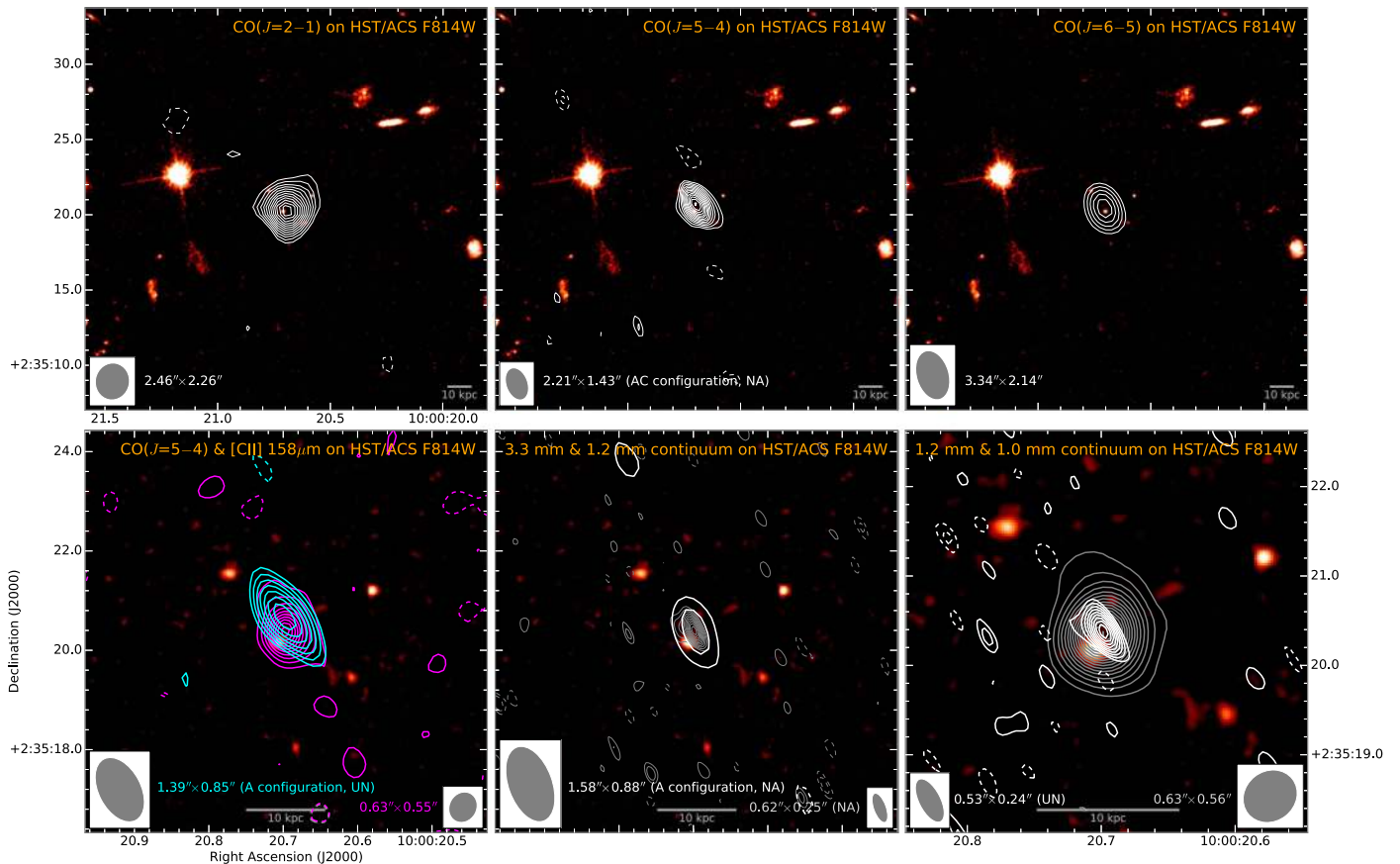
**Figure 5.** Velocity-integrated line and rest-frame far-infrared continuum contour maps overlaid on an HST/ACS F814W continuum image from the COSMOS survey toward AzTEC-3. CO($J = 6 \rightarrow 5$), [C II], and 1.0 mm continuum data are adopted from Riechers et al. (2010, 2014a). Data are imaged with natural (NA) baseline weighting unless mentioned otherwise. Line contour maps in the top row panels include all available data and are averaged over 491, 917, and 874 km s$^{-1}$ (left to right), respectively. Contours start at $\pm 3\sigma$, and they are shown in steps of $1\sigma = 18$, 64, and 224 $\mu$Jy beam$^{-1}$, respectively. The line contour map in the bottom left panel includes only A configuration CO($J = 5 \rightarrow 4$) data (cyan; imaged with uniform weighting). Contours are averaged over 852 (CO) and 466 km s$^{-1}$ (magenta; [C II]), start at $\pm 3$ and $4\sigma$, and they are shown in steps of $1\sigma$ and $4\sigma$, where $1\sigma = 96$ and 200 $\mu$Jy beam$^{-1}$, respectively. Continuum contour maps in the bottom middle panel include only A configuration 3.3 mm continuum data (white). Contours start at $\pm 3\sigma$, and they are shown in steps of $1\sigma = 24.8$ (3.3 mm) and 162 $\mu$Jy beam$^{-1}$ (1.2 mm; gray), respectively. Contours in the bottom right panel start at $\pm 3$ and $5\sigma$, and they are shown in steps of 1 (1.2 mm; white, imaged with uniform weighting) and $5\sigma$ (1.0 mm; gray), where $1\sigma = 187$ and 58 $\mu$Jy beam$^{-1}$, respectively. The synthesized beam size is indicated in the bottom left (white or cyan contours) or right (magenta or gray) corner of each panel. The bottom panels are zoomed-in by a factor of 3.3, except the last panel, which is zoomed-in by a factor of $\sim$6.

(Feroz et al. 2009; Buchner et al. 2014) to sample the posterior distribution of the model parameters and to calculate the model evidence. To optimize the parameter sampling, non-constraining, uniform priors are chosen for additive parameters, logarithmic priors for scale parameters, and a sine prior for the inclination angle. The data are fitted well by the disk model, leaving no significant residuals in the moment-0 map or spectrum. The results for all parameters are given in Table 4. We find a median dynamical mass of $M_{\rm dyn} = 8.6^{+3.6}_{-2.8}(4.5^{+2.1}_{-1.5}) \times 10^{10} M_\odot$ out to a radial distance of 5.5 (3.7) kpc from the center. Given the FWHM diameter of the [C II] emission of $6.4^{+0.7}_{-0.7}$ kpc, the derived values are barely sufficient to host the estimated stellar mass of $\sim 1.2 \times 10^{11} M_\odot$ if the stellar component has a similar extent as the [C II] emission. This could either indicate that the stellar mass in GN10 is overestimated, e.g., due to the model fitting a solution that has a stellar population that is too old or the contribution of a dust-obscured active galactic nucleus (AGN) to the mid-infrared emission (see, e.g., Riechers et al. 2014b); or perhaps, that the kinematic structure of GN10 is not dominated by rotation (such that the dynamical mass is underestimated). Observations of the stellar and gas

components at higher spatial resolution are required to distinguish between these scenarios.

#### 4.1.4. "Underluminous" CO(J = 1 → 0) Emission?

Assuming optically thick emission, the integrated CO($J = 2 \rightarrow 1$) to CO($J = 1 \rightarrow 0$) brightness temperature ratio $r_{21} = 1.37 \pm 0.45$ (compared to $1.84 \pm 0.38$ in line profile peak brightness temperature) toward GN10 suggests that the CO($J = 1 \rightarrow 0$) line could be underluminous compared to expectations for thermalized or sub-thermal gas excitation. Given the comparable spatial resolution of the CO($J = 2 \rightarrow 1$) and CO($J = 1 \rightarrow 0$) observations, this is unlikely to be due to resolution effects. If significant, this effect may be due to the high cosmic microwave background (CMB) temperature at $z = 5.3$ ($T_{\rm CMB} \simeq 17.2$ K), compared to the excitation potential above the ground level of the CO($J = 1 \rightarrow 0$) transition (which corresponds to an excitation temperature of $T_{\rm ex} = 5.5$ K). The CMB acts as both a source of excitation and as a background for the CO emission.

Studies at $z \sim 2$–3 have found evidence for enhanced CO($J = 1 \rightarrow 0$) line widths and line strengths in some DSFGs
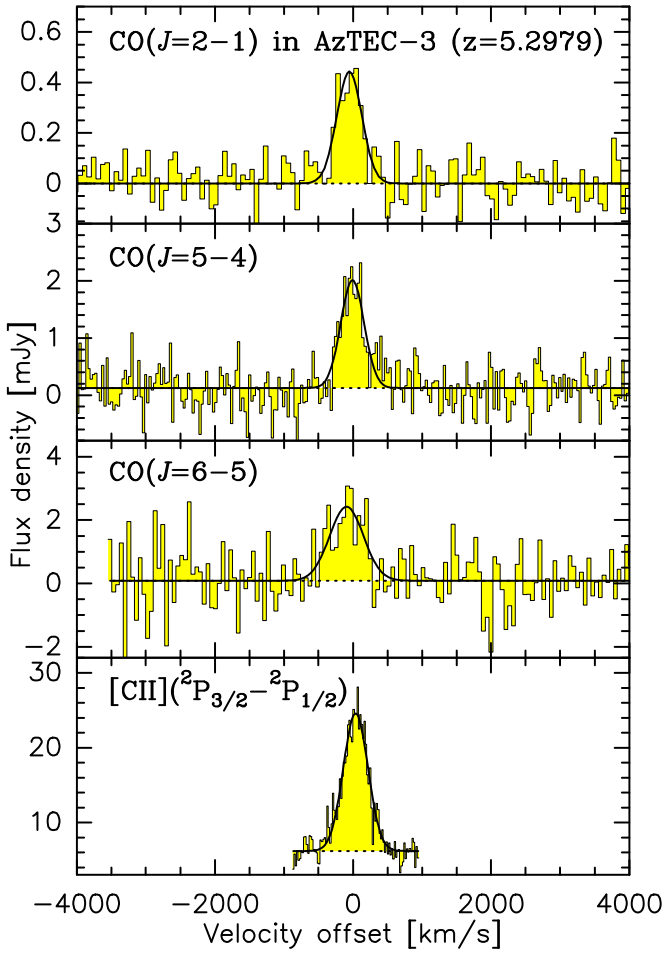
**Figure 6.** VLA, NOEMA, and ALMA line spectra of AzTEC-3 ($z = 5.2979$; histograms) and Gaussian fits to the line profiles (black curves). $CO(J = 6 \rightarrow 5)$ and [C II] data are adopted from Riechers et al. (2010, 2014a). Spectra are shown at resolutions of 66, 33 55, and 20 km s$^{-1}$ (8, 10, 20, and 20 MHz; top to bottom panels), respectively.
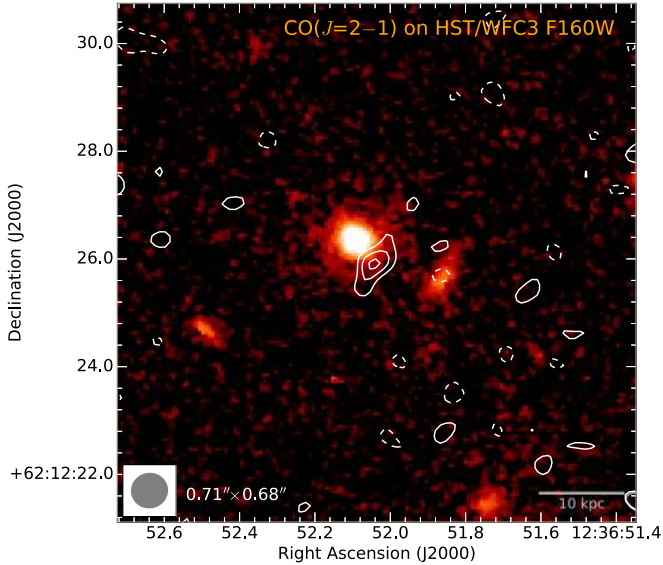


**Figure 7.** Velocity-integrated $CO(J = 2 \rightarrow 1)$ line contour map (VLA C array data only) overlaid on an HST/WFC3 F160W continuum image from the CANDELS survey toward HDF 850.1. The contour map is averaged over 530 km s$^{-1}$. Contours start at $\pm 2\sigma$, and they are shown in steps of $1\sigma = 32.4$ $\mu$Jy beam$^{-1}$. The synthesized beam size is indicated in the bottom left corner.

due to the presence of low-density, low surface brightness gas, for which a low-$T_{ex}$ line like $CO(J = 1 \rightarrow 0)$ is an ideal tracer (e.g., Ivison et al. 2011; Riechers et al. 2011c). The CO brightness temperature itself is measured as a contrast to the CMB. Thus, low surface brightness emission as traced by $CO(J = 1 \rightarrow 0)$ may be disproportionately affected by CMB effects toward higher redshifts (e.g., by heating colder gas to $T_{CMB}$, thereby reducing the observable brightness temperature contrast), such that a preferential impact toward weakened $CO(J = 1 \rightarrow 0)$ line emission may be expected (e.g., da Cunha et al. 2013; Zhang et al. 2016).[39] Thus, a reduced $CO(J = 1 \rightarrow 0)$ line flux compared to higher-$J$ lines due to the CMB appears plausible to explain the observed line spectra toward GN10. However, while not affected as strongly, some impacts on the $CO(J = 2 \rightarrow 1)$ line (having an excitation potential above the ground level of the corresponding $T_{ex} = 16.6$ K, i.e., $\sim T_{CMB}(z = 5.3)$) would also be expected in this scenario, yielding a reduced impact on $r_{21}$.

Apart from effects due to the CMB, another possible scenario is that the low-$J$ CO line emission may not be optically thick in some regions. Given the higher expected optical depth in the $CO(J = 2 \rightarrow 1)$ line compared to $CO(J = 1 \rightarrow 0)$, $r_{21} > 1$ would be possible in this scenario. In principle, self absorption due to cold gas in the foreground of the warmer gas located in the star-forming regions could also disproportionately affect the strength of low-$J$ CO lines in some source geometries. While this finding is intriguing, higher signal-to-noise measurements in the future are desirable to further investigate this effect and its origin based on a detailed comparison of the line profiles.

### 4.2. Properties of AzTEC-3

Here, we update some of the key properties on AzTEC-3, based on the new information available in this work.
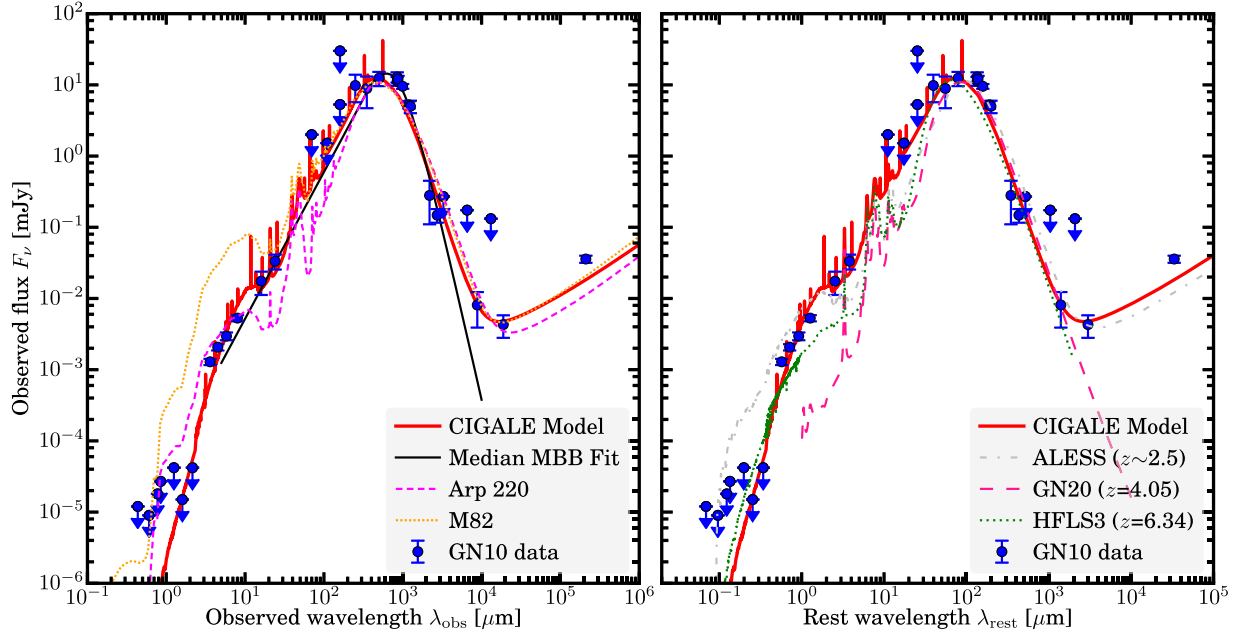
#### 4.2.1. Spectral Energy Distribution

Using the new and updated 1–3 mm photometry from this work, Pavesi et al. (2016) and Magnelli et al. (2019), we have re-fit the SED of AzTEC-3 with the same routine as used by Riechers et al. (2014a), which is similar to that used for GN10 above. We find $T_{dust} = 92^{+15}_{-16}$ K, $\beta_{IR} = 2.09 \pm 0.21$, $\lambda_0^{rest} = 181^{+33}_{-34}$, $\alpha = 10.65^{+6.69}_{-6.42}$, and $L_{FIR} = (1.12 \pm 0.16) \times 10^{13}$ $L_\odot$. These values are consistent with those found by Riechers et al. (2014a). We also find a total infrared luminosity of $L_{IR} = (2.55^{+0.73}_{-0.74}) \times 10^{13}$ $L_\odot$. The relatively large uncertainties compared to $L_{FIR}$ are due to the limited reliability of the Herschel/SPIRE 250–500 $\mu$m photometry near the peak of the SED. Taken at face value, this suggests that $SFR_{IR} = (2500 \pm 700)$ $M_\odot$ yr$^{-1}$.[40]

#### 4.2.2. Star Formation Rate Surface Density

Based on the 1.2 mm size of AzTEC-3, we find a source surface area of $< (2.95 \pm 0.45)$ kpc$^2$ ($0.62 \pm 0.17$ kpc$^2$; second quoted

---

[39] In this scenario, a disproportional impact on emission from cold dust due to a reduced contrast toward and increased heating by the CMB would also be expected, resulting in a higher apparent dust temperature due to changes in the SED shape. This would be consistent with the relatively high measured $T_{dust}$ of GN10.

[40] Given the uncertainties in deriving $L_{IR}$, previous works adopted $L_{FIR}$ to determine the SFR of AzTEC-3. We adopt this updated value here for internal consistency of the analysis presented in this work.

**Figure 8.** Spectral energy distribution of GN10 compared to well-known starbursts and a sample composite from the literature, showing its unusual rest-frame optical/infrared colors even when compared to other dust-obscured galaxies. Left panel: continuum photometry (points), overlaid with median modified blackbody fit (MBB; black line) and CIGALE (red line) models. Literature SED fits for the nearby starbursts M82 (dotted orange line) and Arp 220 (dashed magenta line) are shown for comparison (Silva et al. 1998), normalized to the 500 $\mu$m flux of GN10. Right panel: same points and red line but also showing SED fits for the $z = 4.06$ and $z = 6.34$ DSFGs GN20 (dashed pink line) and HFLS3 (dotted green line), as well as a composite fit to DSFGs in the ALESS survey (dashed–dotted gray line) for comparison (Magdis et al. 2011; Riechers et al. 2013; Swinbank et al. 2014), normalized in the same way.

values indicate the results from circular Gaussian fits, which account for the compact component only). Its flux thus corresponds to a source-averaged rest-frame brightness temperature of $T_b > (4.7 \pm 0.7)$ K $(16.8 \pm 2.2$ K) at rest frame 190 $\mu$m, or $>5\% \pm 1\%$ $(18\% \pm 4\%)$ of the dust temperature obtained from SED fitting. This suggests that AzTEC-3 has significant structure on scales significantly smaller than the $\sim$0″25 beam of our 1.2 mm observations. Using the value of $L_{IR}$ derived in the previous section, this size corresponds to $\Sigma_{IR} > (5.0 \pm 1.6) \times 10^{12} L_\odot$ kpc$^{-2}$ $(18.0 \pm 7.1 \times 10^{12} L_\odot$ kpc$^{-2})$, or $\Sigma_{SFR} > (500 \pm 160) M_\odot$ yr$^{-1}$ kpc$^{-2}$ $(1800 \pm 700 M_\odot$ yr$^{-1}$ kpc$^{-2})$.[41]

### 4.3. Properties of HDF 850.1

The new high-resolution CO($J = 2 \rightarrow 1$) data and a combination of constraints from the literature allow us to determine some additional key properties of HDF 850.1, as detailed in the following subsections.

#### 4.3.1. CO Luminosity Surface Density

For HDF 850.1, the size of the gas reservoir measured from the high-resolution CO($J = 2 \rightarrow 1$) observations at its observed $L'_{CO(2-1)}$ implies a CO luminosity surface density of $\Sigma_{CO(2-1)} = (4.8 \pm 1.8) \times 10^5 L_\odot$ kpc$^{-2}$. We also find a rest-frame CO($J = 2 \rightarrow 1$) peak brightness temperature of $T_b^{CO} = 1.6 \pm 0.4$ K at the $\sim$0″7 resolution of our observations, which agrees to within $\sim$7% with the source-averaged value. This modest value is consistent with the fact that the source is resolved over less than two beams in our current data.

**Table 3**
GN10 MBB and CIGALE SED Modeling Parameters

| Fit Parameter | Unit | Value[a] |
|---|---|---|
| $T_{dust}$ | K | $50.1^{+9.1}_{-9.1}$ |
| $\beta_{IR}$ | | $2.98^{+0.18}_{-0.17}$ |
| $\lambda_0^{rest}$ | $\mu$m | $168^{+22}_{-25}$ |
| $\alpha$ | | $2.06^{+0.15}_{-0.11}$ |
| $f_{158\mu m}^{rest}$ [b] | mJy | $8.3^{+0.5}_{-0.5}$ |
| $M_{dust}$ | $10^9 M_\odot$ | $1.11^{+0.44}_{-0.27}$ |
| $L_{FIR}$ [c] | $10^{13} L_\odot$ | $0.58^{+0.11}_{-0.09}$ |
| $L_{IR}$ [d] | $10^{13} L_\odot$ | $1.03^{+0.19}_{-0.15}$ |
| $SFR_{IR}$ | $M_\odot$ yr$^{-1}$ | $1030^{+190}_{-150}$ |
| $M_\star$ [e] | $10^{11} M_\odot$ | $1.19(\pm 0.06)$ |

**Notes.**
[a] Values as stated are the 50th percentiles. The lower and upper error bars are stated as the 16th and 84th percentiles, respectively.
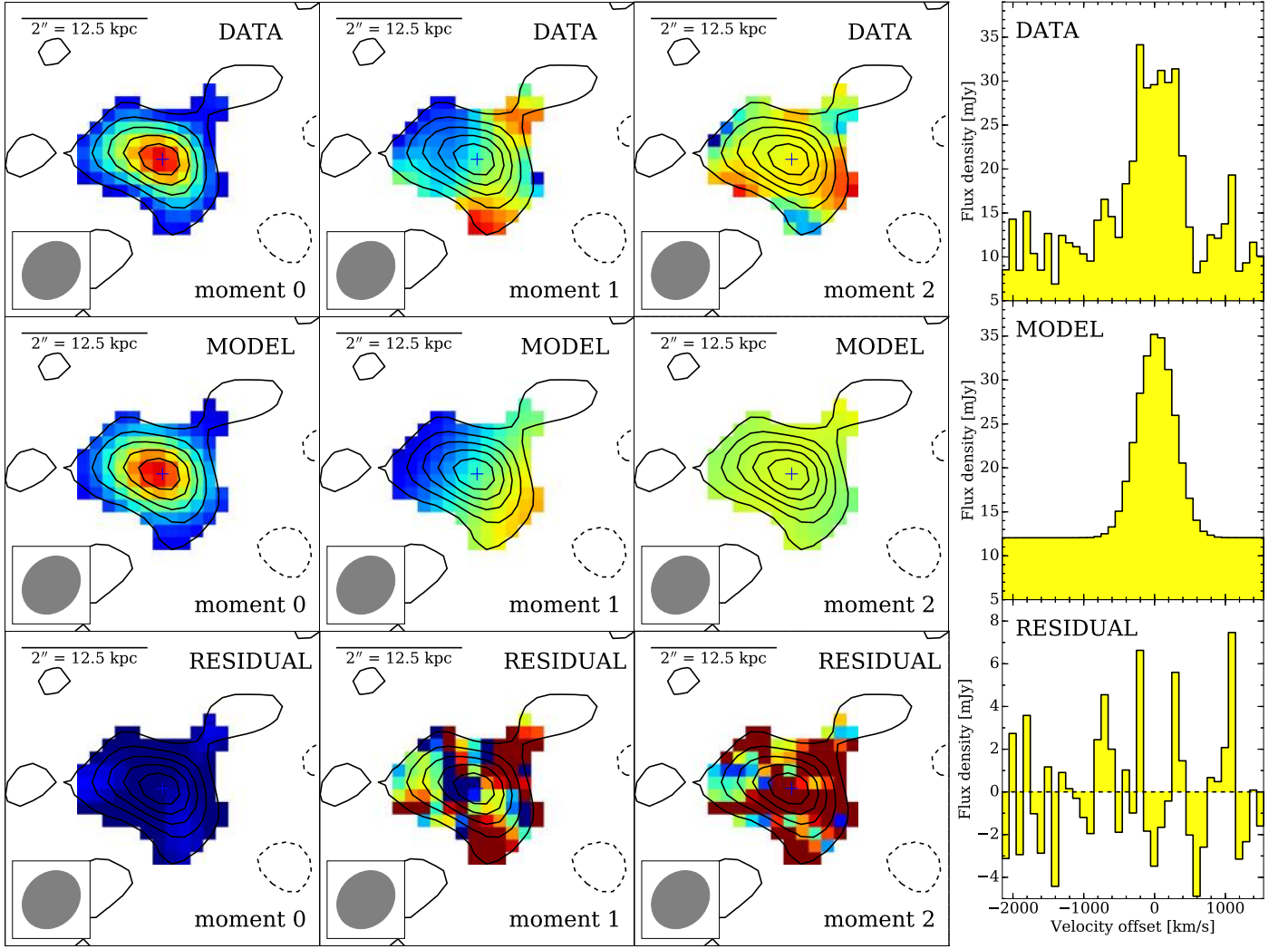[b] Fit normalization parameter.
[c] Integrated between rest frame 42.5 and 122.5 $\mu$m.
[d] Integrated between rest frame 8 and 1000 $\mu$m.
[e] Parameter adopted from CIGALE. Quoted fitting uncertainties underestimate systematic effects and, thus, are not adopted to make any conclusions.

#### 4.3.2. Star Formation Rate Surface Density

Adopting the apparent $L_{IR} = (8.7 \pm 1.0) \times 10^{12} L_\odot$ reported by Walter et al. (2012) and the rest-frame 158 $\mu$m dust continuum size of $(0''9 \pm 0''1) \times (0''3 \pm 0''1)$ reported by Neri et al. (2014), we find an apparent physical source size of $(5.7 \pm 0.6) \times (1.9 \pm 0.6)$ kpc$^2$ and a source-averaged $\Sigma_{IR} = 6.0 \pm 0.9 \times 10^{11} L_\odot$ kpc$^{-2}$ for HDF 850.1. This

---

[41] We here assume that the fraction of the flux contained by the compact component at 1.2 mm is constant with wavelength, which may yield a lower limit on $\Sigma_{IR}$ if this component is warmer than the rest of the source or yield an upper limit if it has a higher optical depth.

**Figure 9.** Visibility space dynamical modeling results for the [C II] emission toward GN10. Intensity (moment-0), velocity (moment-1), and velocity dispersion (moment-2) maps (left panels) for the data (top panels), model (middle panels), and "data–model" residuals (bottom panels), and spectra (histograms; right panels). The median model fits and residuals are shown. Moment-0 contours are overlaid on all panels, and they are shown in steps of $\pm 2\sigma$. Data are imaged with "natural" baseline weighting. Beam size is shown in the bottom left corner of each map panel. Continuum emission was included as part of the additional fitting parameters for the rotating disk model.

**Table 4**
GN10 [C II] Dynamical Modeling Parameters

| Fit Parameter | Unit | Value[a] |
|---|---|---|
| [C II] FWHM diameter | arcsec | $1.03^{+0.11}_{-0.10}$ |
|  | kpc | $6.4^{+0.7}_{-0.7}$ |
| Velocity scale length | arcsec | $0.25^{+0.29}_{-0.18}$ |
|  | kpc | $1.6^{+1.8}_{-1.1}$ |
| Disk inclination | degrees | $80^{+7}_{-8}$ |
| Position angle | degrees | $206^{+5}_{-5}$ |
| Maximum Velocity | km s$^{-1}$ | $320^{+100}_{-80}$ |
| Gas dispersion | km s$^{-1}$ | $220^{+25}_{-25}$ |
| Dust FWHM diameter | arcsec | $0.56^{+0.05}_{-0.05}$ |
|  | kpc | $3.5^{+0.3}_{-0.3}$ |
| $M_{\rm dyn}$ ($r = 3.66$ kpc) | $10^{10}\,M_\odot$ | $4.5^{+2.1}_{-1.5}$ |
| $M_{\rm dyn}$ ($r = 5.49$ kpc) | $10^{10}\,M_\odot$ | $8.6^{+3.6}_{-2.8}$ |

**Note.**
[a] Values as stated are the 50th percentiles. The lower and upper error bars are stated as the 16th and 84th percentiles, respectively.

corresponds to $\Sigma_{\rm SFR} \sim (60 \pm 10)\,M_\odot\,{\rm yr}^{-1}\,{\rm kpc}^{-2}$.[42] We also find a source-averaged rest-frame dust brightness temperature of $T_{\rm b} = 1.4 \pm 0.3$ K at rest frame 158 $\mu$m, or $\sim 4\% \pm 1\%$ of its dust temperature. This suggests that the dust has significant substructure on scales much smaller than the $\sim 0\rlap{.}''35$ beam of the observations presented by Neri et al. (2014). It also is comparable to the CO brightness temperature on comparable scales.

## 5. Discussion of the COLDz $z > 5$ DSFG sample

In this Section, we describe the COLDz $z > 5$ DSFG sample in more detail and place it into context with other known $z > 5$ DSFGs and the space densities and clustering properties of DSFGs at highest redshifts. The key properties are summarized in Tables 5 and 6.

---

[42] The lensing magnification factor cancels out of the surface density calculations, such that the resulting properties are conserved under lensing, barring potential differential lensing effects.

**Table 5**
Derived Properties for COLDz $z > 5$ DSFGs

| Quantity | Unit | GN10 | AzTEC-3 | HDF 850.1 |
|---|---|---|---|---|
| $D_{\rm dust}$ (major × minor axis) | kpc$^2$ | $(1.6 \pm 0.4) \times (0.6 \pm 0.6)$ | $(2.8 \pm 0.9) \times (0.3^{+1.3}_{-0.3})$ | $(5.7 \pm 0.6) \times (1.9 \pm 0.6)$ |
| SFR$_{\rm IR}$ | $M_\odot$ yr$^{-1}$ | $1030^{+190}_{-150}$ | $2500 \pm 700$ | $870 \pm 100$ |
| $\Sigma_{\rm SFR}$ | $M_\odot$ yr$^{-1}$ kpc$^{-2}$ | $600 \pm 210$ | $>500 \pm 160$ | $60 \pm 10$ |
| $\Sigma_{\rm SFR}^{\rm peak}$ | $M_\odot$ yr$^{-1}$ kpc$^{-2}$ | $750 \pm 440$ | $1800 \pm 700$ | |
| $M_{\rm gas}$ | $10^{10}M_\odot$ | $7.1 \pm 0.9$ | $5.7 \pm 0.5$ | $2.2 \pm 0.8$ |
| $M_{\rm dust}$ | $10^8 M_\odot$ | $11.1^{+4.4}_{-2.7}$ | $2.66^{+0.74}_{-0.80}$ | $1.72 \pm 0.31$ |
| GDR $= M_{\rm gas}/M_{\rm dust}$ | | $65^{+20}_{-25}$ | $215^{+65}_{-65}$ | $130 \pm 50$ |
| $M_{\rm dyn}$ | $10^{10}M_\odot$ | $8.6^{+3.6}_{-2.8}$ | $9.7 \pm 1.6$ | $7.5 \pm 3.7$ |
| $f_{\rm gas} = M_{\rm gas}/M_{\rm dyn}$ | | $83\%^{+29\%}_{-36\%}$ | $59\% \pm 11\%$ | $29\% \pm 18\%$ |
| $\alpha_{\rm CO}^{\rm dyn}$ | $M_\odot({\rm K\ km\ s}^{-1}\ {\rm pc}^2)^{-1}$ | $<1.2$ | $<1.7$ | $<3.4$ |
| $\tau_{\rm dep} = M_{\rm gas}/{\rm SFR}_{\rm IR}$ | Myr | $70 \pm 15$ | $22 \pm 7$ | $40 \pm 15$ |
| $L_{\rm C\ II}/L_{\rm FIR}$ | $10^{-3}$ | $2.5 \pm 0.5$ | $0.6 \pm 0.1$ | $1.3 \pm 0.3$ |
| $L_{\rm C\ II}/L_{\rm CO(1-0)}$ | | $4150 \pm 650$ | $2400 \pm 300$ | $4500 \pm 1800$ |

### 5.1. Star Formation Rate Surface Densities

The SFR surface densities of $\Sigma_{\rm SFR} = (750 \pm 440)$ and $(1800 \pm 700)\,M_\odot$ yr$^{-1}$ kpc$^{-2}$ found above for GN10 and the central region of AzTEC-3 are even higher than the values found for some other compact starbursts like ADFS-27 ($z = 5.66$; $430 \pm 90\,M_\odot$ yr$^{-1}$ kpc$^{-2}$) and HFLS3 ($z = 6.34$; $480 \pm 30\,M_\odot$ yr$^{-1}$ kpc$^{-2}$; Riechers et al. 2013, 2017). The source-averaged value of $>(500 \pm 160)\,M_\odot$ yr$^{-1}$ kpc$^{-2}$ for AzTEC-3 is comparable to these sources. Like these systems, GN10 and AzTEC-3 thus show the properties expected for so-called "maximum starbursts". At face value, the peak $\Sigma_{\rm SFR}$ in AzTEC-3 may slightly exceed the expected Eddington limit for starburst disks that are supported by radiation pressure (e.g., Thompson et al. 2005; Andrews & Thompson 2011), but it is potentially consistent under the assumption of a more complex source geometry. On the other hand, the high $\Sigma_{\rm SFR}$ value of GN10 could be boosted by an obscured AGN contribution to the dust heating. GN10 exhibits strong 0.5–8 keV X-ray emission.[43] Using Equation (15) of Ranalli et al. (2003), its observed (absorption-corrected)[44] rest-frame 2–10 keV X-ray luminosity of $L_X = 5.6(12.5) \times 10^{42}$ erg s$^{-1}$ (Laird et al. 2010) corresponds to an SFR$_X$ of $1100(2500)\,M_\odot$ yr$^{-1}$. Given its SFR$_{\rm IR} = 1030^{+190}_{-150}\,M_\odot$ yr$^{-1}$, its $L_X$ remains consistent with intense star formation, but a contribution from a modestly luminous obscured AGN cannot be ruled out, depending on the (relatively uncertain) absorption correction required. This would also be consistent with a possible excess mid-infrared emission due to an obscured AGN, which may be favored by some of the SED fits.

In contrast, the source-averaged $\Sigma_{\rm SFR}$ in HDF 850.1 is only $\sim(60 \pm 10)\,M_\odot$ yr$^{-1}$ kpc$^{-2}$, i.e., $\sim$12 times lower than in GN10, and $\sim$30 times lower than the peak value in AzTEC-3. On the other hand, the values for GN10 and HDF 850.1 would become comparable when assuming the larger 1.0 mm continuum size limit for GN10 instead of the smaller 1.2 mm continuum size adopted above. As such, the source-averaged $\Sigma_{\rm SFR}$ may be more

similar when accounting for potentially extended dust emission if present and, thus, significantly lower than in AzTEC-3, on average. Such more modest, "sub-Eddington" $\Sigma_{\rm SFR}$ on few-kiloparsec scales would be consistent with what is found from high-resolution studies of lower-$z$ DSFG samples, on average (e.g., Simpson et al. 2015; Hodge et al. 2016, 2019). For reference, using the sizes and SFRs for $z > 4$ DSFGs in the AS2UDS sample (Gullberg et al. 2019; Dudzevičiūtė et al. 2020), we find a median $\Sigma_{\rm SFR} = (200 \pm 100)\,M_\odot$ yr$^{-1}$ kpc$^{-2}$, where the error corresponds to the bootstrap uncertainty on the median. Extending the sample down to $z > 3.5$ yields $\Sigma_{\rm SFR} = (170 \pm 20)\,M_\odot$ yr$^{-1}$ kpc$^{-2}$. However, a more precise measurement of the 1.0 mm continuum morphology of GN10 is required to make firm statements about extended dust emission. The intriguingly high peak $\Sigma_{\rm SFR}$ of AzTEC-3 will be explored further in future work.

### 5.2. CO Large Velocity Gradient Modeling

To constrain the line radiative transfer properties of the three COLDz $z > 5$ DSFGs based on the observed CO line excitation, we calculated a series of large velocity gradient (LVG) models, which treat the gas kinetic temperature $T_{\rm kin}$ and the gas density $\rho_{\rm gas}$ as free parameters (Figure 10). For all calculations, the H$_2$ ortho-to-para ratio was fixed to 3:1, the CMB temperature was set to the values appropriate for our targets (16.85–17.18 K at $z = 5.183$ to 5.303), and the Flower (2001) CO collision rates were adopted. We also used a ratio between the CO abundance and velocity gradient of $10^{-5}$ pc (km s$^{-1}$)$^{-1}$ (see, e.g., Weiß et al. 2005b, 2007; Riechers et al. 2006).

Our model of GN10 consists of a single LVG component with $T_{\rm kin} = 40$ K and $\rho_{\rm gas} = 10^{3.6}$ cm$^{-3}$, suggesting the presence of gas at moderate excitation.[45] This model would imply that the CO emission should fill the bulk of the [C II]-emitting region, which perhaps suggests that the warm, compact nucleus traced by the 190 $\mu$m dust emission is embedded in a more extended cold gas reservoir.[46]

For AzTEC-3, we adopt the LVG model discussed by Riechers et al. (2010). This model consists of a low-excitation component with $T_{\rm kin} = 30$ K and $\rho_{\rm gas} = 10^{2.5}$ cm$^{-3}$ and a

---

[43] AzTEC-3 is not detected at X-ray wavelengths.
[44] From fitting a Galactic absorption plus power-law model, an effective photon index $\Gamma = 1.40^{+1.46}_{-1.36}$ was found for GN10, but it was not possible to simultaneously fit the absorbing column $N_H$ and $\Gamma$ due to the limited photon counts. The data are consistent with no intrinsic absorption within the uncertainties, such that the absorption-corrected $L_X$ could be considered an upper limit (Laird et al. 2010) or, alternatively, a lower limit, in the case that it is heavily absorbed.

[45] The model is consistent with a high optical depth in all CO lines.
[46] Both radial variations in temperature and optical depth may contribute to the observed effect; see also discussion by Calistro Rivera et al. (2018).

**Table 6**
Properties of Known $z > 5$ DSFGs

| Name | Redshift | Lensed? | $\mu_L$[a] | Selection[b] | $S_{500}$ (mJy) | $S_{870}$[c] (mJy) | $T_{dust}$[d] (K) | $\mu_L L_{FIR}$[e] ($10^{13} L_\odot$) | $L_{FIR}$ ($10^{12} L_\odot$) | References |
|---|---|---|---|---|---|---|---|---|---|---|
| HXMM-30 | 5.094 | strongly | $\cdots$ | 250–500 $\mu$m | $55 \pm 7$ | $28 \pm 2$ | $\cdots$ | $\cdots$ | $\cdots$ | 1, 2 |
| HELMS_RED_4 | 5.1612 | strongly | $\cdots$ | 250–500 $\mu$m | $116.3 \pm 6.6$ | $52.4 \pm 4.4$ | $66.8 \pm 5.9$ | $9.7^{+2.3}_{-2.1}$ | $\cdots$ | 3, 1 |
| **HDF 850.1** | 5.1833 | weakly | $1.6$[f] | 850 $\mu$m | $<14$ | $7.8 \pm 1.0$ | $35 \pm 5$ | $0.6 \pm 0.1$ | $3.8 \pm 1.0$ | 4, 5 |
| HLS0918 | 5.2430 | strongly | $8.9 \pm 1.9$ | 250–500 $\mu$m | $212 \pm 15$ | $125 \pm 8$ | $38 \pm 3$ | $10.0 \pm 0.6$ | $11.2 \pm 2.5$ | 6 |
| HLock-102 | 5.2915 | strongly | $12.5 \pm 1.2$ | 250–500 $\mu$m | $140 \pm 7$ | $55 \pm 4$ | $54.7 \pm 5.0$ | $9.9 \pm 1.2$ | $7.9 \pm 1.2$ | 7, 8, 1 |
| SPT 2319–55 | 5.2929 | strongly | $6.9 \pm 0.6/13.9 \pm 1.8$ | 1.4 + 2.0 mm | $49.0 \pm 6.6$ | $38.1 \pm 2.9$ | $42.1 \pm 2.1$ | $2.9^{+0.1}_{-0.2}$ | $3.7 \pm 0.8$ | 9 |
| **AzTEC-3** | 5.2980 | no | $\cdots$ | 1.1 mm | $14.4 \pm 8.0$ | $8.7 \pm 1.5$[g] | $92^{+15}_{-16}$ | $1.1 \pm 0.2$ | $11 \pm 2$ | 10, 5 |
| **GN10** | 5.3031 | no | $\cdots$ | 850 $\mu$m | $12.4 \pm 2.8$ | $12.0 \pm 1.4$ | $50.1 \pm 9.1$ | $0.58^{+0.11}_{-0.09}$ | $5.8 \pm 1.0$ | 5 |
| SPT 2353–50 | 5.576 | cluster | $\cdots$ | 1.4 + 2.0 mm | $56.2 \pm 7.1$ | $40.6 \pm 3.8$ | $46.3 \pm 2.3$ | $3.5 \pm 0.2$ | $\cdots$ | 9 |
| ADFS-27 | 5.6550 | weakly? | $\cdots$ | 250–870 $\mu$m | $24.0 \pm 2.7$ | $25.4 \pm 1.8$ | $55.3^{+7.8}_{-7.6}$ | $1.6 \pm 0.3$ | $\lesssim 16 \pm 3$ | 11 |
| SPT 0346–52 | 5.6559 | strongly | $5.6 \pm 0.1$ | 1.4 + 2.0 mm | $203.7 \pm 8.3$ | $130.8 \pm 7.6$ | $50.5 \pm 1.9$ | $13.1^{+0.3}_{-0.6}$ | $23 \pm 1$ | 9 |
| CRLE | 5.6666 | weakly | $1.09 \pm 0.02$ | serendipitous[h] | $31.1 \pm 1.4$ | $16.7 \pm 2.0$ | $41.2^{+6.3}_{-2.2}$ | $1.6 \pm 0.1$ | $15 \pm 1$ | 12 |
| SPT 0243–49 | 5.699 | strongly | $6.7 \pm 0.5/3.1 \pm 0.1$ | 1.4 + 2.0 mm | $57.5 \pm 6.9$ | $84.5 \pm 5.0$ | $32.7 \pm 1.6$ | $3.7 \pm 0.2$ | $7.3 \pm 1.7$ | 9 |
| SPT 2351–57 | 5.811 | cluster | $\cdots$ | 1.4 + 2.0 mm | $73.8 \pm 5.7$ | $34.6 \pm 3.1$ | $53.5 \pm 2.8$ | $4.6^{+0.2}_{-0.3}$ | $\cdots$ | 9 |
| ID 85001929 | 5.847 | no? | $\cdots$ | SED template[i] | $14.6 \pm 2.1$ | $5.3 \pm 0.8$ | $59.0^{+7.7}_{-16.7}$[j] | $0.58^{+0.08}_{-0.07}$[j] | $5.8 \pm 0.8$ | 13 |
| HeLMS-54ab | 5.880 | no? | $\cdots$ | 250–500 $\mu$m | $97 \pm 9$[k] | $36 \pm 4$[k] | $\cdots$ | $\cdots$ | $\cdots$ | 1, 2 |
| G09-83808 | 6.0269 | strongly | $8.2 \pm 0.3$ | 250–500 $\mu$m | $44.0 \pm 8.2$ | $36.2 \pm 9.1$ | $35.9 \pm 1.5$ | $2.1 \pm 0.3$ | $2.6 \pm 0.4$ | 14, 15 |
| HFLS3 | 6.3369 | weakly | $1.8 \pm 0.6$[l] | 250–500 $\mu$m | $47.3 \pm 2.8$ | $33.0 \pm 2.4$ | $55.9^{+9.3}_{-12.0}$ | $2.9 \pm 0.3$ | $16 \pm 5$ | 7, 1 |
| SPT 0311–58 | 6.900 | weakly | $2.0$[f] | 1.4 + 2.0 mm | $51.8 \pm 8.2$ | $36.9 \pm 7.4$ | $45.6 \pm 3.3$ | $4.4^{+0.4}_{-0.3}$ | $22 \pm 5$ | 16 |

**Notes.** Sources in bold are sources described in the previous sections. Uncertainties in $T_{dust}$ are the statistical uncertainties from the fitting procedures adopted by different authors and do not account for systematic uncertainties due to differences between the procedures (see references provided for additional details). The method adopted here for GN10 is virtually identical to those used for fitting HELMS_RED_4, HLock-102, AzTEC-3, ADFS-27, CRLE, ID 85001929, and HFLS3.

[a] Lensing magnification factor. Modeled with two source components when multiple values are given. The uncertainties of full SED-based quantities for strongly lensed sources (i.e., those with $\mu_L > 2$ and/or evidence for multiple lensed images) may be limited by systematic effects, given that magnification factors are typically derived at a single wavelength only and that the regions within the galaxies that are brightest at the selection wavelength could be preferentially magnified.

[b] Sources identified as "red" between the 250 and 500 $\mu$m bands were typically preferentially followed up if they showed high 850 $\mu$m–1.3 mm fluxes.

[c] $S_{850}$ or $S_{890}$ is used where $S_{870}$ is not available.

[d] Dust temperatures with small uncertainties typically are due to keeping $\beta_{IR}$, $\lambda_0$, or both fixed in the fitting process. HLS0918 was fitted with an optically thin model only, which may underestimate $T_{dust}$. HDF 850.1 was fitted with a MAGPHYS-based model, and its dust peak is only constrained by upper limits shortward of 850 $\mu$m.

[e] Apparent FIR luminosity, i.e., not corrected for lensing magnification where applicable.

[f] No uncertainties are quoted in the original works. Here, we assume 20% uncertainty for the calculation of derived quantities.

[g] Simpson et al. (2020) report an updated value of $8.3 \pm 0.3$ mJy, which is consistent with the original measurement.

[h] Source was also independently identified as "red" at 250–500 $\mu$m (D. Riechers et al. 2020, in preparation).

[i] Source was selected at 850 $\mu$m (originally reported at 1.2 mm; Bertoldi et al. 2007) but followed up based on a photometric redshift obtained by fitting a template SED based on HFLS3 (Riechers et al. 2013).

[j] Values obtained by fitting the de-blended fluxes at 100 $\mu$m–3 mm using a method virtually identical to that adopted for GN10. The $T_{dust}$ is compatible with the value of $61 \pm 8$ K reported by Jin et al. (2019).

[k] Blended with a lower-$z$ source that contributes $\sim$30% of the flux at 870 $\mu$m and likely a higher fraction at 500 $\mu$m.

[l] Updated value based on visibility-plane lens modeling of the dust and gas emission.

**References**—[1] D. Riechers et al. (2020, in preparation); [2] Oteo et al. (2017a); [3] Asboth et al. (2016); [4] Walter et al. (2012); [5] this work; [6] Rawle et al. (2014); [7] Riechers et al. (2013); [8] Dowell et al. (2014); [9] Strandet et al. (2016); [10] Riechers et al. (2014a); [11] Riechers et al. (2017); [12] Pavesi et al. (2018a); [13] Jin et al. (2019); [14] Fudamoto et al. (2017); [15] Zavala et al. (2018); [16] Strandet et al. (2017).
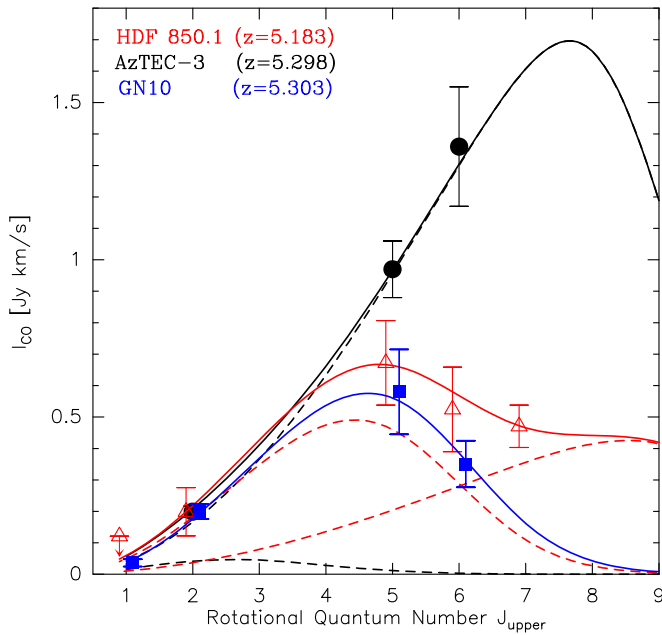
**Figure 10.** CO excitation ladders (points) and LVG modeling (lines) of the three COLDz $z > 5$ DSFGs analyzed in this work. The line fluxes are normalized to the strength of the CO($J = 2 \rightarrow 1$) line in AzTEC-3. The sources are slightly offset from each other in $J_{\mathrm{upper}}$ to improve clarity. The models (solid lines) of AzTEC-3 and HDF 850.1 consist of two gas components each (dashed lines).

high-excitation component with $T_{\mathrm{kin}} = 45$ K and $\rho_{\mathrm{gas}} = 10^{4.5}$ cm$^{-3}$. Based on the updated CO($J = 2 \rightarrow 1$) flux, we reduce the area filling factor of the lower-temperature component. This component now contributes only $\sim 20\%$ to the CO($J = 2 \rightarrow 1$) line flux. This model suggests an expected CO($J = 1 \rightarrow 0$) flux of 0.057 Jy km s$^{-1}$ or a CO($J = 2 \rightarrow 1$) to CO($J = 1 \rightarrow 0$) line ratio of $r_{21} = 0.91$. If the high-excitation gas were distributed over the same $3.9 \times 2.1$ kpc$^2$ area as the [C II] emission imaged by Riechers et al. (2014a), the LVG model would imply an area filling factor of close to 50%. Assuming the extent of the main CO($J = 5 \rightarrow 4$) component determined above instead would imply a filling factor of just above 30%. The low-excitation gas, on the other hand, would need to be distributed over an area at least twice as large in linear extent as the [C II] emission, corresponding to an area approximately half as large as the current observed limit on the CO($J = 2 \rightarrow 1$) diameter of $\sim 8$ kpc. In light of these findings, we will re-visit these models in future work, once more observational constraints are available.

The bulk emission in HDF 850.1 can be modeled with an LVG component with the same parameters as for GN10 (suggesting an expected CO $J = 1 \rightarrow 0$ flux of 0.036 Jy km s$^{-1}$), but the model does not reproduce the ratio between the CO($J = 6 \rightarrow 5$) and CO($J = 7 \rightarrow 6$) lines well. Thus, to improve the model fit, it is necessary to add a second, high-excitation gas component with $T_{\mathrm{kin}} = 70$ K and $\rho_{\mathrm{gas}} = 10^{4.5}$ cm$^{-3}$.[47] The moderate- and high-excitation components in this model fill $\sim 20\%$ and $\sim 1.4\%$ of the [C II]-emitting area imaged by Neri et al. (2014), respectively. If we were to assume the CO($J = 2 \rightarrow 1$) size determined above instead, we would find $\sim 7.5\%$ lower values. These values are

indistinguishable from those based on the [C II] size within the uncertainties.

With current observational constraints, these LVG model solutions are not unique, but they illustrate that the gas excitation in all sources can be modeled with parameters that span a range similar that of the parameters found in nearby spiral galaxies and starbursts (e.g., Weiß et al. 2005b; Güsten et al. 2006). Moreover, we find clear differences in the gas excitation between $z > 5$ DSFGs, showing that AzTEC-3 is likely in a more extreme phase of its evolution as reflected in its high molecular gas excitation, perhaps due to a high gas density in its nuclear region or due to contributions from a buried AGN to the gas excitation. All of the sources in our sample follow the CO($J = 5 \rightarrow 4$)—FIR luminosity relation for star-forming galaxies (Figure 11; e.g., Daddi et al. 2015; Liu et al. 2015), which shows that their level of star formation activity (as traced by $L_{\mathrm{FIR}}$) is consistent with what is expected based on the properties of the warm, dense molecular gas (as traced by CO $J = 5 \rightarrow 4$). This is in agreement with the idea that a lower inferred CO excitation among galaxies in our sample is likely related to a lower fraction of dense molecular gas in the star-forming regions.

### 5.3. Gas Masses, Gas Surface Densities, Gas Fractions, Gas-to-dust Ratios, Gas Depletion Times, and Conversion Factor

Adopting the CO($J = 1 \rightarrow 0$) fluxes from the LVG modeling and $\alpha_{\mathrm{CO}} = 1\, M_{\odot}$(K km s$^{-1}$ pc$^2$)$^{-1}$ to convert the resulting CO($J = 1 \rightarrow 0$) luminosities to molecular gas masses $M_{\mathrm{gas}}$, we find $M_{\mathrm{gas}} = (7.1 \pm 0.9), (5.7 \pm 0.5)$, and $(2.2 \pm 0.8) \times 10^{10}\, M_{\odot}$ for GN10, AzTEC-3, and HDF 850.1,[48] respectively, where the overall uncertainties are dominated by systematic uncertainties in $\alpha_{\mathrm{CO}}$.[49] For GN10, this corresponds to $83\%^{+29\%}_{-36\%}$ of the dynamical mass estimate, which is representative under the assumption that the CO($J = 1 \rightarrow 0$) emission is as extended as the [C II] emission on which the dynamical modeling was carried out. Adopting the dynamical mass estimate of $M_{\mathrm{dyn}} = (9.7 \pm 1.6) \times 10^{10}\, M_{\odot}$ found for AzTEC-3 by Riechers et al. (2014a), its updated gas mass corresponds to $59\% \pm 11\%$ of the dynamical mass under the same assumptions. Using an isotropic virial estimator (e.g., Engel et al. 2010) and the [C II] sizes and line widths of its two components derived by Neri et al. (2014), we find a combined dynamical mass of $M_{\mathrm{dyn}} = 7.5 \times 10^{10}\, M_{\odot}$ for HDF850.1.[50] As such, its gas mass corresponds to $29\% \pm 18\%$ of the dynamical mass under the same assumptions as for GN10. Conversely, based on their observed $L'_{\mathrm{CO}}$, the dynamical masses of GN10, AzTEC-3, and HDF 850.1 at face value imply upper limits of $\alpha_{\mathrm{CO}} < 1.2$, $< 1.7$, and $< 3.4\, M_{\odot}$(K km s$^{-1}$ pc$^2$)$^{-1}$, respectively. For HDF 850.1, the size of the gas reservoir measured from the high-resolution CO($J = 2 \rightarrow 1$) observations implies a molecular gas mass surface density of $\Sigma_{\mathrm{gas}} = (1.3 \pm 0.5) \times 10^3\, M_{\odot}$ pc$^{-2}$. This suggests that HDF 850.1 follows the spatially resolved star formation law, which has been determined at lower redshifts (e.g., Hodge et al. 2015).

Given the dust masses of $(11.1^{+4.4}_{-2.7})$, $(2.66^{+0.74}_{-0.80})$, and $(1.72 \pm 0.31) \times 10^8\, M_{\odot}$ for GN10, AzTEC-3, and HDF 850.1

---

[47] Since no detections above $J_{\mathrm{upper}} = 7$ exist, we caution that the parameters of this second component are only poorly constrained by the data.

[48] Gas and dust masses and sizes for HDF 850.1 are corrected by a factor of $\mu_{\mathrm{L}} = 1.6$ to account for gravitational lensing magnification (Neri et al. 2014).
[49] Statistical uncertainties in $r_{21}$ from the LVG modeling likely contribute only at the 10%–15% level.
[50] The uncertainties of this estimate are dominated by systematic effects due to the choice of fitting method, which corresponds to at least 50%.
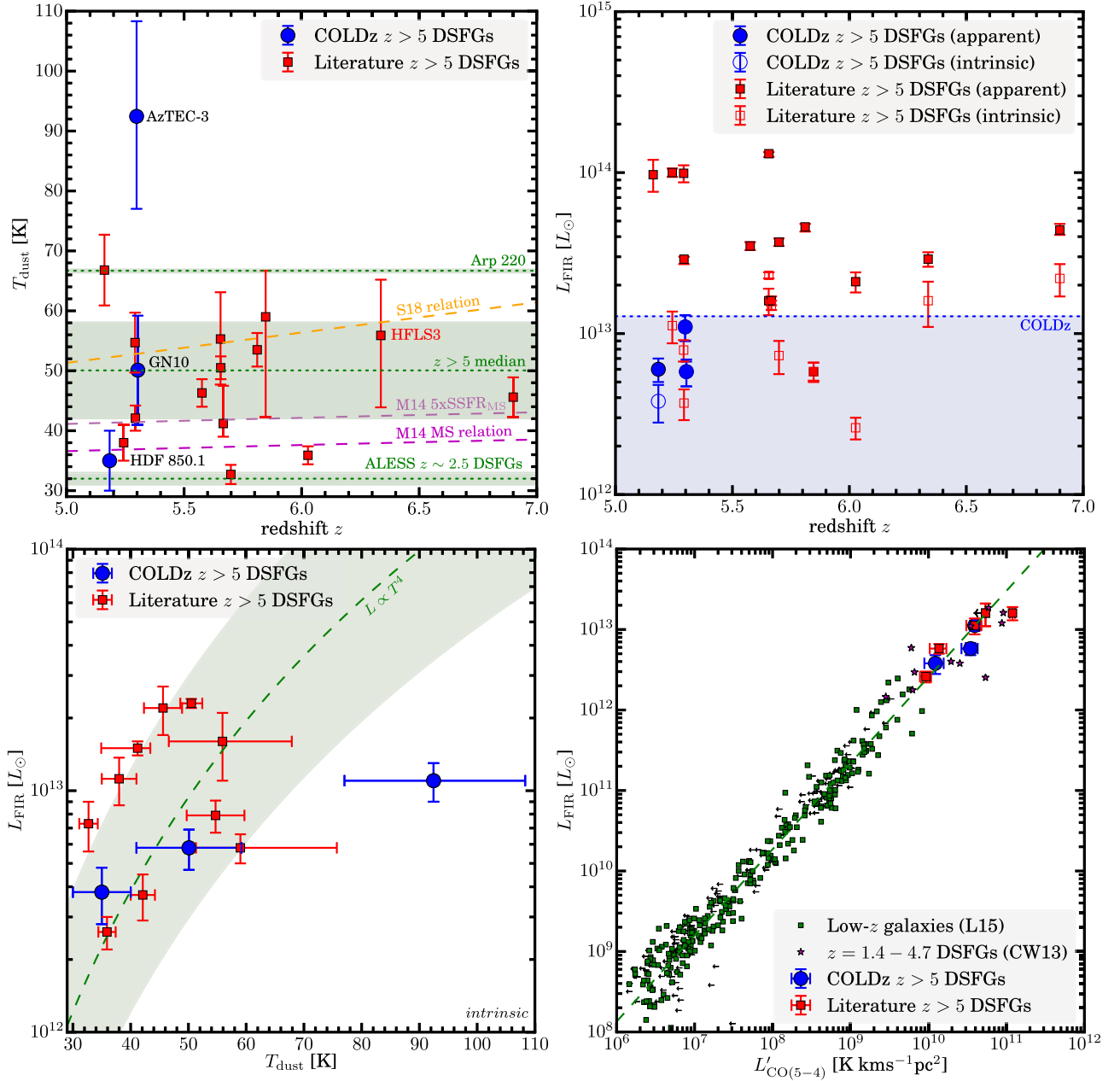
**Figure 11.** Dust temperature (top left panel) and FIR luminosity (top right panel) of COLDz $z > 5$ DSFGs, compared to literature DSFGs, showing that they cover a broad range in dust temperatures and that they are less luminous than other DSFGs known at $z > 5$. They also probe a luminosity range that is only accessible through gravitational lensing in other current samples with spectroscopic redshifts (dotted dividing line in the top right panel; see Table 6 for references), with the exception of one source discovered recently from de-blended single-dish catalogs (Jin et al. 2019). There is a weak trend between dust temperature and FIR luminosity within the current sample, which is largely consistent with a standard $L \propto T^4$ scaling (dashed line in the bottom left panel, shown scaled to the median values and with $\pm 0.5$ dex scatter as the shaded region for reference). The dotted lines and shaded regions in the top left panel show representative dust temperatures and uncertainty ranges for ALESS $z \sim 2.5$ DSFGs (Swinbank et al. 2014), the $z > 5$ sample median, and the nearby dusty starburst Arp 220. The dashed orange line shows the relation proposed by Schreiber et al. (2018). The lower and upper dashed magenta lines show the relation proposed by Magnelli et al. (2014) for "main-sequence" (MS) galaxies and for galaxies with specific star formation rates five times higher than the MS, respectively. The COLDz $z > 5$ DSFGs also closely follow the CO($J = 5 \rightarrow 4$)—FIR luminosity relation of nearby galaxies (bottom right panel; the green symbols, upper limit arrows without symbols, and dashed line show the Herschel/SPIRE spectroscopy sample and relation by Liu et al. 2015), suggesting that the properties of the dense, warm gas in their star-forming regions are as expected for starburst galaxies. The magenta stars show a lower-redshift comparison DSFG sample, updated from the compilation of Carilli & Walter (2013), featuring data from Andreani et al. (2000), Weiß et al. (2005a, 2009), Carilli et al. (2010), Riechers et al. (2011a, 2011b), Cox et al. (2011), Danielson et al. (2011), and Salomé et al. (2012). Values are corrected for gravitational magnification unless mentioned otherwise.

(this work; Riechers et al. 2014a; Walter et al. 2012), the gas masses correspond to gas-to-dust ratios of $\sim 65^{+20}_{-25}$, $215^{+65}_{-65}$, and $130 \pm 50$, respectively, which are in the range of values found for nearby infrared-luminous galaxies (e.g., Wilson et al. 2008). Given the SFRs of $(1030^{+190}_{-150})$, $(2500 \pm 700)$, and

$(870 \pm 80) \, M_\odot \, \mathrm{yr}^{-1}$, (this work; Riechers et al. 2014a; Walter et al. 2012; Neri et al. 2014), they also yield gas depletion times of $\tau_{\mathrm{dep}} = (70 \pm 15)$, $(22 \pm 7)$, and $(40 \pm 15) \, \mathrm{Myr}$, respectively. This is consistent with short, $\lesssim 100 \, \mathrm{Myr}$ starburst phases, as also typically found for
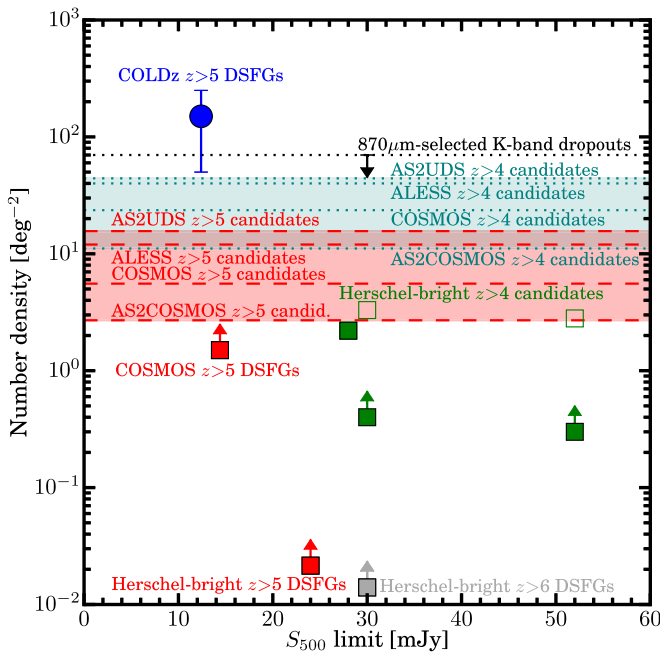
**Figure 12.** Number densities of high-redshift dusty galaxy samples down to a given 500 μm flux limit, showing that the values found for COLDz $z > 5$ DSFGs (blue points; GOODS-North field only) are high even when compared to lower-$z$ DSFG samples. The green and gray squares show red Herschel source samples identified by Riechers et al. (2013), Dowell et al. (2014), Asboth et al. (2016), and Ivison et al. (2016). The open symbols show the full samples, and the filled symbols show the estimated fractions or lower limits of $z > 4$ ($z > 6$) sources where applicable. The red symbols show lower limits at $z > 5$ based on the spectroscopically confirmed sources in Table 6, using the full size of the COSMOS field (2 deg$^2$) and the HerMES fields from which sources were selected (325 deg$^2$ total). The dotted black line shows "$K$-band dropout" galaxies identified at 870 μm for reference (Dudzevičiūtė et al. 2020), many of which are likely at $z \sim 3$–4 (the line thus is an upper limit for $z > 4$). The dotted teal and dashed red lines and shaded areas are candidate $z > 4$ and $z > 5$ DSFGs in the COSMOS, ALESS, AS2UDS, and $S_{870} > 6.2$ mJy AS2COSMOS samples, selected at 1.1 mm, 870 μm, 850, and 850 μm, respectively (Simpson et al. 2014, 2020; Miettinen et al. 2017; Dudzevičiūtė et al. 2020). The COLDz and COSMOS samples are not selected at 500 μm; the symbols are shown at the lowest detected 500 μm flux in the samples instead of a formal flux limit.

lower-redshift DSFGs (e.g., Simpson et al. 2014; Dudzevičiūtė et al. 2020), with the lowest value found for the source showing the highest gas excitation.

### 5.4. [C II]/FIR and [C II]/CO Luminosity Ratios

To further investigate the differences in conditions for star formation among the three COLDz $z > 5$ DSFGs, we consider their [CII]($^2P_{3/2} \rightarrow ^2P_{1/2}$)/FIR and [CII]($^2P_{3/2} \rightarrow ^2P_{1/2}$)/CO($J = 1 \rightarrow 0$) luminosity ratios (e.g., Stacey et al. 1991, 2010). We adopt the CO($J = 1 \rightarrow 0$) fluxes from the LVG modeling. We find [C II]/FIR ratios of $L_{\rm C II}/L_{\rm FIR} = (2.5 \pm 0.5)$, $(0.6 \pm 0.1)$, and $(1.3 \pm 0.3) \times 10^{-3}$ for GN10, AzTEC-3, and HDF 850.1, respectively, i.e., a factor of $\sim$4 variation. These values are consistent with what is expected for luminous starburst galaxies (e.g., Graciá-Carpio et al. 2011). The differences between sources mirror those seen in the CO line ladders, indicating lower [C II]/FIR ratios with increasing CO excitation. In GN10, the CO($J = 6 \rightarrow 5$) emission interestingly appears to show a comparable extent to the 1.2 mm continuum emission (see Figure 4) and, thus, is more compact than the [C II] emission. Thus, the source-averaged CO excitation may be comparatively low, but it may

be significantly higher in the nuclear region with the highest $\Sigma_{\rm SFR}$. Given the larger spatial extent of the [C II] emission, the [C II]/FIR ratio likely also is substantially lower in this region than the source average, consistent with the apparent global trend between [C II]/FIR and CO excitation.

We also find [C II]/CO ratios of $L_{\rm C II}/L_{\rm CO(1-0)} \simeq 4150 \pm 650$,[51] $2400 \pm 300$, and $4500 \pm 1800$ for GN10, AzTEC-3, and HDF 850.1, respectively, i.e., a factor of $\sim$2 variation. These values are consistent with expectations for starburst galaxies at lower redshifts (e.g., Stacey et al. 2010, and references therein).[52] The lowest ratio is found for AzTEC-3, i.e., the source with the highest gas excitation (but the two lower-excitation sources show comparable values), the highest dust temperature (see Table 6), and the highest peak $\Sigma_{\rm SFR}$. This may suggest a reduced [C II] line strength due to a stronger, more intense interstellar radiation field, but it could also be due to dust extinction of the [C II] line emission or a low brightness temperature contrast between the [C II] and 158 μm dust emission in the nuclear starburst region.

### 5.5. Dust Temperatures

We find that the COLDz $z > 5$ DSFGs exhibit a broad range in dust temperatures. HDF 850.1 ($z = 5.18$) has a comparatively low $T_{\rm dust} = (35 \pm 5)$ K (Walter et al. 2012), while GN10 ($z = 5.30$) shows a moderate $T_{\rm dust} = (50 \pm 9)$ K, especially when compared to the relatively high $T_{\rm dust} = (92^{+15}_{-16})$ K displayed by AzTEC-3 ($z = 5.30$; Riechers et al. 2014a).[53]

It is interesting to place these galaxies into the more general context of all currently known $z > 5$ DSFGs available in the literature (see Table 6 and the top panels of Figure 11).[54] The full $z > 5$ literature sample contains other sources in the same category as HDF 850.1, with relatively modest $T_{\rm dust} = 33$–46 K such as CRLE ($z = 5.67$; Pavesi et al. 2018a) and the gravitationally lensed HLS0918 ($z = 5.24$; Rawle et al. 2014), SPT 2319–55, 2353–50, 0243–49, and 0311–58 ($z = 5.29$, 5.58, 5.70, and 6.90; Strandet et al. 2016, 2017), and G09-83808 ($z = 6.03$; Fudamoto et al. 2017), sources with higher $T_{\rm dust} = 50$–59 K like GN10 such as ADFS-27 ($z = 5.66$; Riechers et al. 2017), ID 85001929 ($z = 5.85$; Jin et al. 2019), HFLS3 ($z = 6.34$; Riechers et al. 2013), and the gravitationally lensed HLock-102 ($z = 5.29$; Riechers et al. 2013; Dowell et al. 2014) and SPT 0346–52 and 2351–57 ($z = 5.66$ and 5.81; Strandet et al. 2016), and sources with high $T_{\rm dust} > 60$ K closer to AzTEC-3 like the strongly lensed HELMS_RED_4 ($z = 5.16$; $T_{\rm dust} = 67 \pm 6$ K; Asboth et al. 2016; D. Riechers et al. 2020, in preparation).

All currently known $z > 5$ DSFGs have relatively high dust temperatures (median value: $50.1 \pm 8.0$ K based on 17 galaxies,[55] with an average value of 50.3 K) in comparison to

---

[51] Adopting the measured CO($J = 1 \rightarrow 0$) luminosity instead of that inferred from the LVG modeling would yield a ratio of $\simeq$5400 for GN10.

[52] We caution that a direct comparison in terms of physical properties to lower redshifts (as is typically done with photon dominated region models calculated at $z = 0$) is not straight forward due to the reduction in the intensity of low-$J$ CO line emission at $z > 5$ due to the warmer CMB.

[53] Note that an optically thin fitting procedure suggests a more modest dust temperature of $(53 \pm 5)$ K compared to the general fitting result adopted here, but it also yields a worse fit to the data.

[54] Jin et al. (2019) report ID 20010161, a source with a candidate redshift of $z = 5.051$ based on a single emission line. While the identification is plausible, we do not include it in the current data compilation until the redshift is confirmed.

[55] Uncertainties are given as the median absolute deviation.

the bulk of the population at $z \sim 2$–3 ($32 \pm 1$ K, i.e., $\sim 1.57 \pm 0.25$ times lower; e.g., Swinbank et al. 2014; see also Simpson et al. 2017; Dudzevičiūtė et al. 2020).[56] Given the heterogenous selection and some differences in the fitting methods used, we investigate to what degree they could be responsible for this difference, but we find no trends that would be sufficient to explain this difference. We then explore if the higher $T_{dust}$ in the $z > 5$ sample is due to a trend with redshift or $L_{FIR}$ and find that the latter is likely sufficient to explain the observed differences to lower-redshift samples.

### 5.5.1. Potential Biases due to Gravitational Lensing, Selection Wavelength, or SED Fitting Method

Removing all strongly lensed and cluster-lensed galaxies from the full $z > 5$ sample to investigate potential differential lensing bias, we find a median value of $(52.7 \pm 6.7)$ K based on eight galaxies. This value is higher than the full sample median and, thus, does not provide direct evidence for preferential magnification of higher $T_{dust}$ regions in the lensed subsample. Removing all galaxies selected at wavelengths shorter than 850 $\mu$m to investigate potential SED peak selection bias, we find $(46.0 \pm 4.7)$ K based on 10 galaxies. We thus do not find significant evidence that the different selection methods strongly bias the median $T_{dust}$ for this $z > 5$ sample. Comparing sources that used the same SED fitting method as GN10 and AzTEC-3 (eight galaxies; see Table 6 caption for details) to the SPT sample (six galaxies), which was fitted with a common but somewhat different method (using graybody-only fits with fixed $\beta_{IR} = 2$ and $\lambda_0 = 100$ $\mu$m; e.g., Weiß et al. 2013), we find median values of $(55.6 \pm 4.5)$ and $(46.0 \pm 4.2)$ K, respectively. The former subsample is selected at shorter wavelengths (except one serendipitous discovery), while the latter contains a higher fraction of strongly and cluster-lensed systems (25% versus 83%). Thus, the different median $T_{dust}$ cannot be directly attributed to differences in the fitting methods, but our study would be consistent with it playing a role. Overall, we thus find that the median value appears not to be significantly biased toward high values based on the heterogenous composition of the sample, while keeping in mind that even the combination of all current selection methods could entirely miss $z > 5$ DSFGs in undersampled regions of the parameter space.

### 5.5.2. Comparison to Proposed $T_{dust}$–$z$ Relations

Using the median redshift of the sample of 5.66, we find expected median values of $T_{dust}$ of 37.3 and 54.6 K when applying the $T_{dust}$–$z$ relations by Magnelli et al. (2014), their Equation (4), and Schreiber et al. (2018), their Equation (15),[57] for galaxies on the star-forming main sequence (Figure 11, top left panel). At face value, the Magnelli et al. relation appears consistent with the lowest $T_{dust}$ sources, but the $z > 5$ sample would need to exhibit median star formation rates that are a factor of $\sim 90$ higher ($\sim 240$ when only considering unlensed and weakly lensed systems) than those of main-sequence galaxies at the same redshift with the

same $M_{\star}$ for this relation to agree with the median $T_{dust}$ value of our sample. While most of the current sample is likely to be in excess of the main sequence, there is no evidence for a difference of more than a factor of several in SFR compared to the main sequence. As such, current observations of $z > 5$ DSFGs would appear to be in favor of a stronger evolution in $T_{dust}$ with redshift than indicated by this relation when assuming that redshift is the main property responsible for explaining the observed differences, unless systematic effects in the sample selection and SED fitting methods are more significant than currently known. On the other hand, a significant fraction of the $z > 5$ sample appears to be in reasonable agreement with expectations based on the Schreiber et al. relation, but the predicted median value is higher than that observed for the sample as a whole.[58] At least half of the sample has a lower $T_{dust}$ than expected from this relation.

Both of the proposed $T_{dust}$–$z$ relations have to be extrapolated significantly in redshift to match our sample, such that the observed mismatches are likely consistent with the true uncertainties of these relations. In particular, the $T_{dust}$ of main-sequence galaxies at $z > 5$ is currently only poorly constrained by observations (e.g., Pavesi et al. 2016), such that it remains unclear that an offset in SFR from the main sequence can currently be meaningfully translated to expected differences in $T_{dust}$ for dusty starbursts at these redshifts. Also, the increasing CMB temperature toward $z > 5$ provides a natural cutoff at low $T_{dust}$, both due to a reduced brightness temperature contrast and due to a higher contribution to dust heating (e.g., da Cunha et al. 2013). This effect leads to an overall change in SED shape and increase in the measured $T_{dust}$ with redshift but is not accounted for in current extrapolations of the $T_{dust}$–$z$ relations. On the other hand, it has recently been suggested that previously proposed $T_{dust}$–$z$ relations could be an observational artifact due to selection effects (Dudzevičiūtė et al. 2020). If there were to be no trend in $T_{dust}$ with redshift, another explanation would be required to explain the high median $T_{dust}$ of the $z > 5$ sample.

### 5.5.3. Investigation of $T_{dust}$–$L_{FIR}$ Relations

We find a trend between $T_{dust}$ and $L_{FIR}$ in our sample (Figure 11), which spans about an order of magnitude in intrinsic $L_{FIR}$ and a factor of 2.8 in $T_{dust}$. The data are consistent with an overall increase of $L_{FIR}$ with $T_{dust}$. For $z > 5$ DSFGs with $T_{dust} < 50.1$ K (i.e., below the sample median), we find a median $L_{FIR} = (7.3 \pm 3.9) \times 10^{12} L_{\odot}$, but for those with $>50.1$ K, we find $(11.0 \pm 5.0) \times 10^{12} L_{\odot}$, as is consistent with the general trends found for lower-redshift DSFG samples (e.g., da Cunha et al. 2015; Simpson et al. 2017; Dudzevičiūtė et al. 2020). Taken at face value, this trend may at least partially, and perhaps entirely, explain the high median $T_{dust}$ of the current $z > 5$ DSFG sample as being due to their relatively high median $L_{FIR}$. Indeed, the three intrinsically least-luminous sources in the sample with an average $L_{FIR} = (3.4 \pm 0.7) \times 10^{12} L_{\odot}$ have an average $T_{dust} = (38 \pm 4)$ K, which is much closer to lower-redshift samples with comparable $L_{FIR}$, like ALESS and AS2UDS.[59] In the simplest scenario, the higher $T_{dust}$ in the $z > 5$ DSFG sample thus could be due to their high

---

[56] Luminosity-averaged values of $T_{dust}$ from energy balance modeling for ALESS galaxies are higher, with an average of $(43 \pm 2)$ K (da Cunha et al. 2015). Here, we adopt those from Swinbank et al., since their derivation is more consistent with the methods used for the $z > 5$ DSFG sample.

[57] Value obtained after scaling by their Equation (6) to obtain modified blackbody temperatures.

[58] The relation also suggests 38.7 K at $z \sim 2.5$, which is $\sim 20\%$ higher than the ALESS sample median.

[59] For reference, the $z \sim 2$–3 ALESS sample has a median $L_{FIR} = (3.0 \pm 0.3) \times 10^{12} L_{\odot}$ at $T_{dust} = (32 \pm 1)$ K Swinbank et al. 2014).

median SFRs. This subject thus warrants further study based on the detailed dust properties of larger galaxy samples in the future.

### 5.6. Number Densities and Space Densities

The overall population of DSFGs was found to be sufficient to explain the early formation of most luminous local and intermediate redshift elliptical galaxies, under the assumption that DSFGs are their intensely star-forming progenitors (e.g., Simpson et al. 2014). On the other hand, the highest-redshift luminous DSFGs are the likely progenitors of some of the most massive compact "quiescent" galaxies at $z > 2$ (e.g., Toft et al. 2014). As such, a comparison of their space densities to such galaxies can help us to understand the duty cycles, formation mechanisms, and buildup of massive galaxies through cosmic history. Thus, it is important to better understand the reliability of current constraints on their space densities. The COLDz survey provides a unique selection method that significantly differs from traditional DSFG surveys, which provides new insights compared to previous estimates.

Searching the COLDz data, we have detected three luminous $z > 5$ DSFGs in $CO(J = 2 \rightarrow 1)$ emission in an area of $\sim 60\ arcmin^2$, compared to four independently confirmed sources detected in $CO(J = 1 \rightarrow 0)$ at $z = 2.0\text{-}2.8$ (one of which is a DSFG) in the same area. On the one hand, the co-moving volume covered by the survey is $\sim 6.4$ times larger for searches of $CO(J = 2 \rightarrow 1)$ emission at $z = 4.9\text{-}6.7$ compared to those of $CO(J = 1 \rightarrow 0)$, at a comparable excitation-corrected $L'_{CO}$ limit (P18, R19). Also, one of the fields was chosen to include AzTEC-3 at $z = 5.298$, which thus needs to be removed from comparisons to avoid potential bias.[60] As such, there are significantly fewer serendipitously discovered CO-rich galaxies per unit volume in the higher-redshift bin. On the other hand, once AzTEC-3 is removed from further consideration, the two other sources alone still imply a significant excess in the CO luminosity function at $z \sim 5\text{-}7$ compared to (admittedly uncertain) model expectations (R19; their Figure 4). Also, given other recent studies such as the serendipitous discovery of another luminous $z > 5$ DSFG in the COSMOS field (Pavesi et al. 2018a), such sources may indeed be more common than expected based on previous predictions. As such, a closer look at these expectations is warranted.

*COLDz Number Density and Space Density*—Conservatively restricting the analysis to the GOODS-North field (i.e., excluding AzTEC-3 and its environment), the two detected sources alone correspond to a number density of $\sim (150 \pm 100)\ deg^{-2}$ for $z > 5$ DSFGs, or a space density of $(1.0 \pm 0.7) \times 10^{-5}\ Mpc^{-3}$, within the volume probed in $CO(J = 2 \rightarrow 1)$ emission by COLDz ($\sim 200{,}000\ Mpc^3$ in GOODS-North alone; R19).[61]

*Comparison to Bright Samples from Large-area Surveys*— At bright flux levels (i.e., down to a limit of $S_{500} > 52\ mJy$ at 500 μm), Asboth et al. (2016) find 477 candidate $z > 4$ DSFGs in an area of $274\ deg^2$ based on the selection of red Herschel sources (i.e., sources with $S_{250} < S_{350} < S_{500}$). Based on a

power-law fit to their sample, they find a number density of $2.8\ deg^{-2}$. Follow-up observations of a subsample of 188 sources at longer wavelengths suggest that at least 21, or $\sim 11\%$, are highly probable to be at $z > 4$ (Duivenvoorden et al. 2018). This corresponds to a number density of $> 0.3\ deg^{-2}$. Applying a similar selection down to a limit of $S_{500} > 30\ mJy$ over an area of $21\ deg^2$, Dowell et al. (2014) find a number density of $3.3\ deg^{-2}$ based on 38 such sources, of which at least $\sim 11\%$ are spectroscopically confirmed to be at $z > 4$. This corresponds to a number density of $> 0.4\ deg^{-2}$. Based on the $z = 6.34$ DSFG HFLS3 alone, Riechers et al. (2013) estimate that the number density of such sources may drop to values as low as $0.014\ deg^{-2}$ at $z > 6$. For a sample of 109 out of 708 sources found with similar selection criteria ($S_{500}/S_{250} \geqslant 1.5$ and $S_{500}/S_{350} \geqslant 0.85$ and $28 < S_{500} < 73\ mJy$ (with the exception of one source at $S_{500} = 118\ mJy$) selected over $\sim 600\ deg^2$, Ivison et al. (2016) find that about one-third of their candidates (or $\sim 2.2\ deg^{-2}$ when correcting for completeness) are likely at $z > 4$. This leads them to infer a space density of $\sim 6 \times 10^{-7}\ Mpc^{-3}$ for $z > 4$ DSFGs after applying a duty cycle correction. All of these estimates likely imply number densities of $< 1\ deg^{-2}$ for $z > 5$ DSFGs down to $S_{500} > 28\ mJy$ (Figure 12). Indeed, the number density of spectroscopically confirmed $z > 5$ red Herschel sources in the HerMES fields provides a lower limit of only $(0.021 \pm 0.008)\ deg^{-2}$ down to $S_{500} > 24\ mJy$. In addition, some simulations appear to suggest that the number densities of red Herschel sources could be biased toward high values due to selection effects introduced by the noise level and limited resolution of the Herschel data (e.g., Béthermin et al. 2017). If significant, this would render current space density estimates as upper limits.

With $S_{500} = (12.4 \pm 2.8)$, $(14.4 \pm 8.0)$, and $< 14\ mJy$ for GN10, AzTEC-3, and HDF 850.1 (Table 6; Walter et al. 2012; Riechers et al. 2014a; Liu et al. 2018), respectively, all of the COLDz $z > 5$ DSFGs would have been missed by all of these surveys by factors of $> 2\text{-}4$ in $S_{500}$ (Figure 12; see also Figure 11 for a comparison to other $z > 5$ samples in $L_{FIR}$).[62] However, the more than two-orders-of-magnitude difference in the implied space and number densities likely either suggests that such sources are overrepresented in the COLDz survey area due to large-scale structure even after neglecting AzTEC-3, or that the counts fall very steeply with flux in the $10 \lesssim S_{500} \lesssim 30\ mJy$ regime at $z > 5$, or that current selection methods underlying these previous estimates are more incomplete than currently thought. Substantially larger survey areas than are accessible with surveys like COLDz would be required to distinguish between these possibilities. Until such surveys are available, further insight may be gained through a comparison to samples selected over smaller areas, but down to lower flux levels, than the bright samples discussed so far.

*Comparison to Faint Samples*—Targeted studies of DSFG populations down to $S_{870} \gtrsim 1\ mJy$ (e.g., Simpson et al. 2014; i.e., typically a factor of a few fainter than our $z > 5$ sample with $S_{870/890} = (12.0 \pm 1.4)$, $(8.7 \pm 1.5)$, and $(7.8 \pm 1.0)\ mJy$ for GN10, AzTEC-3, and HDF 850.1, respectively; Wang et al. 2007; Younger et al. 2007; Cowie et al. 2009; see Table 6) appear to indicate an order-of-magnitude or more higher space densities

---

[60] The redshift of HDF 850.1 was known at the time the COLDz survey was carried out, but the field was chosen based on the availability of the deep HST/WFC3-IR CANDELS data, not the presence of this source. Thus, it is not excluded from the space density discussion, since it should not introduce a bias.
[61] Quoted uncertainties here and in the following paragraphs are the standard deviation of a Poisson distribution given the number of sources detected.

[62] These surveys, however, may contain strongly lensed analogs of COLDz sources (Figure 11).

($>5 \times 10^{-6}\,\mathrm{Mpc}^{-3}$; Cooke et al. 2018)[63] for $4 < z < 5$ DSFGs than are found for the typically order-of-magnitude or more brighter Ivison et al. (2016) sample.[64] This lower limit provides a closer match to the space density implied by the COLDz data at face value, but it likely still falls short given the lower redshift and lower flux limit of this comparison sample.[65] On the other hand, interferometric follow-up surveys of flux-limited DSFG samples such as ALESS and AS2UDS find number densities of "$K$-band dropout" sources of $\sim 0.02\,\mathrm{arcmin}^{-2}$, or $\sim 70\,\mathrm{deg}^{-2}$ (Figure 12; e.g., Simpson et al. 2014, 2017; Dudzevičiūtė et al. 2020; also see discussion of similar sources, e.g., by Dannerbauer et al. 2004; Frayer et al. 2004; Franco et al. 2018). These sources may be considered analogs of HDF 850.1 and GN10 in some respects, but they typically have lower $870\,\mu\mathrm{m}$ fluxes and currently mostly lack spectroscopic confirmation and molecular gas mass measurements. Also, many of them are consistent with $z \sim 3$–4 (see discussion in Dudzevičiūtė et al. 2020), such that the true number density of "COLDz analogs" among them is likely significantly lower.[66] Based on largely photometric redshifts, the Atacama Large sub/Millimeter Array (ALMA)-COSMOS, ALESS, and AS2UDS samples selected at 1.1 mm, $870\,\mu\mathrm{m}$, and $850\,\mu\mathrm{m}$ provide space density estimates of $(24 \pm 6)$, $(40 \pm 13)$, and $(42 \pm 7)\,\mathrm{deg}^{-2}$ for candidate $z > 4$ DSFGs, and $(5.6 \pm 2.8)$, $(12 \pm 7)$, and $(16 \pm 4)\,\mathrm{deg}^{-2}$ for $z > 5$ candidates, respectively (Simpson et al. 2014; Miettinen et al. 2017; Dudzevičiūtė et al. 2020). Taking the full photometric redshift probability functions into account results in space density estimates of $(11 \pm 1)$ and $(2.7 \pm 0.4)\,\mathrm{deg}^2$ down to $S_{870} > 6.2\,\mathrm{mJy}$ at $z > 4$ and $z > 5$, respectively, based on the AS2COSMOS survey (Simpson et al. 2020). These samples suggest that the space densities of DSFGs decline by factors of $\sim 3$–4 from $z = 4$ to 5 and that, at most, $\sim 1\%$–3% of the $850\,\mu\mathrm{m}$–1.1 mm-selected DSFGs at the currently achieved flux limits[67] appear to be at $z > 5$. Moreover, spectroscopic follow-up of two of the three $z > 5$ candidates in the ALESS survey finds them to be at $4 < z < 5$, reducing the true ALESS $z > 5$ space density estimate by a factor of three (Danielson et al. 2017). Adopting instead the spectroscopically confirmed $z > 5$ DSFGs found across the full COSMOS field provides a lower limit on their space density of only $>(1.5 \pm 0.9)\,\mathrm{deg}^{-2}$, i.e., $\lesssim 3$–4 times below the estimate based on the Miettinen et al. (2017) sample. As such, the space density of $z > 5$ DSFGs in COLDz appears to remain high by factors of $\sim 6$–55 when compared to faint DSFG samples, but the differences are significantly reduced relative to the comparison to bright DSFG samples. A higher completeness in spectroscopic confirmation of faint DSFGs will be critical to allow for a more detailed comparison, especially in the

$S_{870} \gtrsim 5\,\mathrm{mJy}$ regime probed by the current COLDz $z > 5$ detections.[68]

*Potential Role of Selection Effects*—A possible concern for the comparisons between the COLDz and continuum surveys (beyond the increased impact of gravitational lensing on the brighter populations) is that samples selected at a single sub/ millimeter wavelength may be incomplete at a given $L_{\mathrm{FIR}}$ due to selection effects, in particular, those related to dust temperature or optical depth, which could lead to an underestimate in the volume density of luminous $z > 5$ DSFGs. On the one hand, samples selected at short wavelengths, e.g., at $500\,\mu\mathrm{m}$ (i.e., $\lesssim 80\,\mu\mathrm{m}$ rest frame at $z > 5$) and below, could miss sources with low dust temperatures or high dust optical depths at the highest redshifts, for which the dust SED peak shifts to significantly longer wavelengths than $500\,\mu\mathrm{m}$. An example of such sources is "$870\,\mu\mathrm{m}$ risers", which are required to either be extremely luminous or strongly gravitationally lensed to remain detectable at $\leqslant 500\,\mu\mathrm{m}$ (Riechers et al. 2017). Indeed, despite its moderately high dust temperature, GN10 has an $870\,\mu\mathrm{m}$ flux that is just below the "$870\,\mu\mathrm{m}$ riser" selection criterion. On the other hand, samples selected at long wavelengths, e.g., 2 mm (i.e., $\lesssim 330\,\mu\mathrm{m}$ rest frame at $z > 5$) and above, may be anticipated to be more complete at the highest redshifts (see, e.g., Staguhn et al. 2014, or similar discussion by Casey et al. 2018), but they could miss sources at high dust temperatures. As an example, a recent sensitive 2 mm survey in COSMOS finds several dusty sources that are claimed to be at a relatively high median redshift compared to shorter-wavelength selected samples as expected, but it missed AzTEC-3 (i.e., the highest-significance CO detection in the COLDz survey and the most distant DSFG currently known in the area surveyed at 2 mm) due to its relatively high dust temperature (Magnelli et al. 2019).[69] Surveys at $870\,\mu\mathrm{m}$ (i.e., $\lesssim 150\,\mu\mathrm{m}$ in the rest frame) are less incomplete due to variations in $T_{\mathrm{dust}}$ at a given $L_{\mathrm{FIR}}$ at $z > 5$ than at lower redshifts (see, e.g., discussion by Simpson et al. 2017; Dudzevičiūtė et al. 2020), but they are also affected. Such selection effects can be largely addressed by a comprehensive multiwavelength selection of DSFGs, but they can contribute to the uncertainties in the current estimates of the space density of $z > 5$ DSFGs.

*Potential Contribution of Cosmic Variance due to Clustering* —In principle, the COLDz survey may have led to the identification of an unexpectedly high number of $z > 5$ DSFGs due to cosmic variance in the survey fields. On the one hand, the fields containing AzTEC-3 and HDF 850.1 are known to contain overdensities in star-forming galaxies (e.g., Capak et al. 2011; Walter et al. 2012). In particular, the AzTEC-3 proto-cluster environment (which was removed from all comparisons of space densities) corresponds to one of the highest matter density peaks currently known in the very early universe (e.g., Capak et al. 2011; Smolčić et al. 2017). Also, the redshift difference between the close-by HDF 850.1 and GN10 is only $\mathrm{d}z \simeq 0.12$ (i.e., $\Delta v \simeq 5800\,\mathrm{km\,s}^{-1}$), which corresponds to a co-moving distance of 61.4 Mpc. As such, there already is evidence for large-scale structure, which, in principle, could include both DSFGs in GOODS-North. On the other hand, the redshift difference between GN10 and AzTEC-3 is only

---

[63] Also see Aravena et al. (2010) for comparable estimates at $z = 3$–5 based on single-dish 1.2 mm-selected sources.

[64] The Ivison et al. (2016) sample has single-dish fluxes of $S_{850} = 8$–71 mJy, including upper limits consistent with this range. Thus, it reaches down to the long wavelength fluxes of the COLDz $z > 5$ sample, despite having substantially higher fluxes at its prime selection wavelength of $500\,\mu\mathrm{m}$.

[65] Simpson et al. (2017) estimate a co-moving space density of $\sim 10^{-5}\,\mathrm{Mpc}^{-3}$ for AS2UDS DSFGs with a median $S_{870} = (8.0 \pm 0.4)$ mJy. While more comparable in $S_{870}$ to the COLDz $z > 5$ DSFG sample, only one of their sources has an estimated photometric redshift of $z > 5$.

[66] The Simpson et al. (2017) AS2UDS sample contains two "$K$-band dropout" sources with $S_{870} > 8.0$ mJy but no redshift estimates, which could be the closest analogs to sources like GN10 and HDF 850.1.

[67] There appears to be a trend that the brightest $S_{870}$-selected DSFGs tend to be found at higher redshifts (e.g., Younger et al. 2007; Simpson et al. 2020).

[68] Values after accounting for the gravitational magnification of HDF 850.1.

[69] GN10 and HDF 850.1, however, are solidly and tentatively detected in a 2 mm survey in GOODS-North, consistent with their lower dust temperatures (Staguhn et al. 2014).

d$z \simeq 0.005$ (i.e., $\Delta v \simeq 240$ km s$^{-1}$, or 2.5 Mpc co-moving distance) and, thus, much smaller, but they are located in very different parts of the sky. As such, a physical connection between these sources is not considered to be possible. Thus, the modest redshift difference between GN10 and HDF 850.1 does not necessarily imply a physical connection (and indeed, would require a rather large correlation length). Moreover, it remains plausible to infer that modest overdensities such as the one associated with HDF 850.1 may simply be highlighted by the presence of DSFGs and, thus, a common feature of the environments of such sources at $z > 5$ (see also, e.g., Pavesi et al. 2018b), rather than representing regions on the sky that contain unusually high densities of DSFGs (which are also known to exist at $z > 4$, but perhaps are much less common; e.g., Oteo et al. 2018, Miller et al. 2018, but also see Robson et al. 2014). From these considerations, it remains unclear that the field selection alone is sufficient to explain the apparent excess in CO-bright galaxies at $z > 5$ in the COLDz volume.

## 6. Summary and Conclusions

We have detected CO($J = 2 \rightarrow 1$) emission toward three $z > 5$ massive dusty starburst galaxies by searching the $\sim 60$ arcmin$^2$ VLA COLDz survey data (see P18, R19, for a complete description), including a new secure redshift identification of the "optically dark" source GN10 at $z = 5.303$. Despite star formation rates of $\sim 500$–$1000\, M_\odot$ yr$^{-1}$, two of the sources (which are separated by only $\sim 5'$ on the sky) remain undetected at rest-frame ultraviolet to optical wavelengths, below an observed-frame wavelength of 3.6 $\mu$m, due to dust obscuration. Molecular line scans such as COLDz thus are an ideal method to determine the redshifts for such sources, which will remain challenging to study in their stellar light at least until the launch of the James Webb Space Telescope (JWST).

By carrying out a multiwavelength analysis including new NOEMA and VLA observations of GN10, AzTEC-3, and HDF 850.1, we find a broad range of physical properties among this CO-selected $z > 5$ DSFG sample, including a factor of $\sim 2.5$ difference in dust temperatures ($T_{\rm dust} = 35$–$92$ K), a range of a factor of $\sim 3$ in gas masses ($M_{\rm gas} = 2.2$–$7.1 \times 10^{10}\, M_\odot$) and gas-to-dust ratios (65–215), a factor of up to $\sim 30$ difference in SFR surface densities ($\Sigma_{\rm SFR} = 60$–$1800\, M_\odot$ yr$^{-1}$ kpc$^{-2}$), factors of $\sim 4$ and $\sim 2$ difference in the $L_{\rm C\,II}/L_{\rm FIR}$ and $L_{\rm C\,II}/L_{\rm CO(1-0)}$ ratios (0.6–$2.5 \times 10^{-3}$ and 2400–4500, respectively), and significant differences in CO line excitation and the implied gas densities and kinetic temperatures. In particular, we find a trend that appears to suggest a decrease in $L_{\rm C\,II}/L_{\rm FIR}$ with increasing CO excitation. We also find that the gas depletion times vary by a factor of $\sim 3$ across the sample ($\tau_{\rm dep} = 22$–$70$ Myr), consistent with short starburst phases. Given the high inferred $\Sigma_{\rm SFR}$, we cannot rule out a contribution of a heavily obscured AGN to the dust heating and/or gas excitation in these compact systems.

At the resolution of the current follow-up data, GN10 appears to consist of a compact, $\sim 1.6$ kpc diameter, at least moderately optically thick "maximum starburst" nucleus embedded in a more extended, $\sim 6.4$ kpc diameter rotating cold gas disk. This finding is qualitatively consistent with those for lower-redshift DSFG samples (e.g., Riechers et al. 2011c; Ivison et al. 2011; Calistro Rivera et al. 2018). AzTEC-3 appears to consist of a compact, optically thick $\sim 0.9$ kpc region exhibiting $\sim 75\%$ of the dust luminosity, embedded in a more extended, $\sim 3.9$ kpc diameter gas reservoir, which makes it an even more extreme nuclear starburst than GN10. HDF 850.1, on the other hand, appears to exhibit more moderate properties for a massive starburst, with a $\sim 3 \times$ lower SFR than AzTEC-3 spread across a $\sim 6.7$ kpc diameter cold gas reservoir, which contains two kinematic components (Neri et al. 2014).

By placing the COLDz $z > 5$ DSFGs into context with all other $z > 5$ DSFGs currently known, we find that their dust temperatures are typically a factor of $\sim 1.5$ higher than the bulk of the population at $z \sim 2$–3. On the one hand, such a trend is expected if $T_{\rm dust}$–$z$ relations proposed in the literature were to hold (e.g., Magnelli et al. 2014; Schreiber et al. 2018), but the level of increase in $T_{\rm dust}$ with redshift is not captured well by these relations (which require a significant extrapolation in redshift). We investigate potential biases due to preferential gravitational magnification, sample selection wavelength, and SED fitting methods, but find no clear evidence that the median $T_{\rm dust}$ is biased toward high values due to the heterogenous composition of the parent sample. At the same time, it cannot be ruled out that currently employed selection methods miss $z > 5$ DSFGs in undersampled regions of the parameter space. On the other hand, the sample shows a trend suggesting an increase in $L_{\rm FIR}$ toward higher $T_{\rm dust}$. Given their typically very high dust luminosities, this trend is consistent with findings for lower-$z$ DSFG samples (e.g., da Cunha et al. 2015; Simpson et al. 2017) without requiring any redshift evolution. This perhaps suggests that the observed trends in $T_{\rm dust}$ could be mostly, if not entirely, due to the relatively high median $L_{\rm FIR}$ (and thus, SFR) of the current $z > 5$ DSFG sample.

If the COLDz survey area is representative, the space density of $z > 5$ DSFGs could be significantly higher than previously thought based on observations and simulations of the brightest DSFGs found in large-area sub/millimeter surveys. These sources appear to produce a significant bright-end excess to the CO luminosity function compared to models (R19; their Figure 4). This appears consistent with recent serendipitous discoveries of other $z > 5$ DSFGs in targeted studies, but statistics at the sub/millimeter flux levels of our sample are currently too limited to allow for firm conclusions. Future large-area molecular line scan surveys with VLA, ALMA, and ultimately, Next Generation Very Large Array (ngVLA; e.g., Bolatto et al. 2017) will be required to put these findings on a statistically more solid footing.

## Appendix A
## GN10 Line Parameters

Here, we provide a table including the full line parameters from Gaussian fitting to the line profiles for GN10 (Table A1). We also provide a figure showing the upper-limit spectrum for the HCN, HCO$^+$, and HNC $J = 1 \rightarrow 0$ lines (Figure A1).

**Table A1**
GN10 Line Parameters

| Line | | $S_\nu$ ($\mu$Jy) | $dv_{\mathrm{FWHM}}$ (km s$^{-1}$) | $v_0$[a] (km s$^{-1}$) | $I_{\mathrm{line}}$ (Jy km s$^{-1}$) |
|---|---|---|---|---|---|
| CO($J = 1 \rightarrow 0$) | | $74 \pm 13$ | $687 \pm 144$ | $-23 \pm 60$ | $0.054 \pm 0.017$ |
| CO($J = 2 \rightarrow 1$) | | $544 \pm 63$ | $512 \pm 72$ | $0 \pm 30$ | $0.295 \pm 0.035$ |
| CO($J = 5 \rightarrow 4$) | | $1046 \pm 205$ | $772 \pm 220$ | $-27 \pm 71$ | $0.86 \pm 0.20$ |
| CO($J = 6 \rightarrow 5$) | | $719 \pm 144$ | $681 \pm 173$ | $-78 \pm 70$ | $0.52 \pm 0.11$ |
| [CII]($^2P_{3/2} \rightarrow {}^2P_{1/2}$) | (A) | $(24.7 \pm 1.6) \times 10^3$ | $617 \pm 67$ | $-173 \pm 24$ | $17.6 \pm 1.9$[b] |
| | (B) | $(6.0 \pm 4.2) \times 10^3$ | $227 \pm 243$ | $-875 \pm 128$ | |
| HCN($J = 1 \rightarrow 0$) | | | $(512)$[c] | | $<0.017$ |
| HCO$^+$($J = 1 \rightarrow 0$) | | | $(512)$[c] | | $<0.017$ |
| HNC($J = 1 \rightarrow 0$) | | | $(512)$[c] | | $<0.017$ |
| CCH($N = 1 \rightarrow 0$) | | | $(512)$[c] | | $<0.025$[d] |

**Notes.**
[a] Velocity offset relative to CO($J = 2 \rightarrow 1$) redshift and uncertainty from Gaussian fitting.
[b] Summed over both components. Component (A) alone is $(16.2 \pm 1.4)$ Jy km s$^{-1}$.
[c] Fixed to CO($J = 2 \rightarrow 1$) line width.
[d] We conservatively assume equal strength of the hyperfine-structure transitions to obtain this limit. Assuming that the three strongest components dominate would yield a $3\sigma$ limit of $<0.021$ Jy km s$^{-1}$.
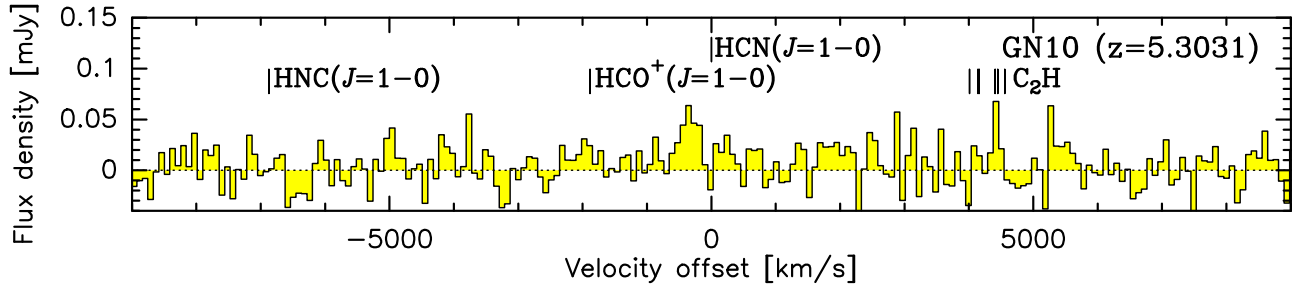


**Figure A1.** VLA line limit spectrum of GN10 ($z = 5.3031$; histogram). The spectrum is shown at a resolution of 85 km s$^{-1}$ (4 MHz), referenced to the expected redshift of the HCN($J = 1 \rightarrow 0$) line. Velocities where the peaks of the HCN, HCO$^+$, and HNC $J = 1 \rightarrow 0$ lines are expected to appear are indicated, as well as the hyperfine-structure transitions of the CCH($N = 1 \rightarrow 0$) line.
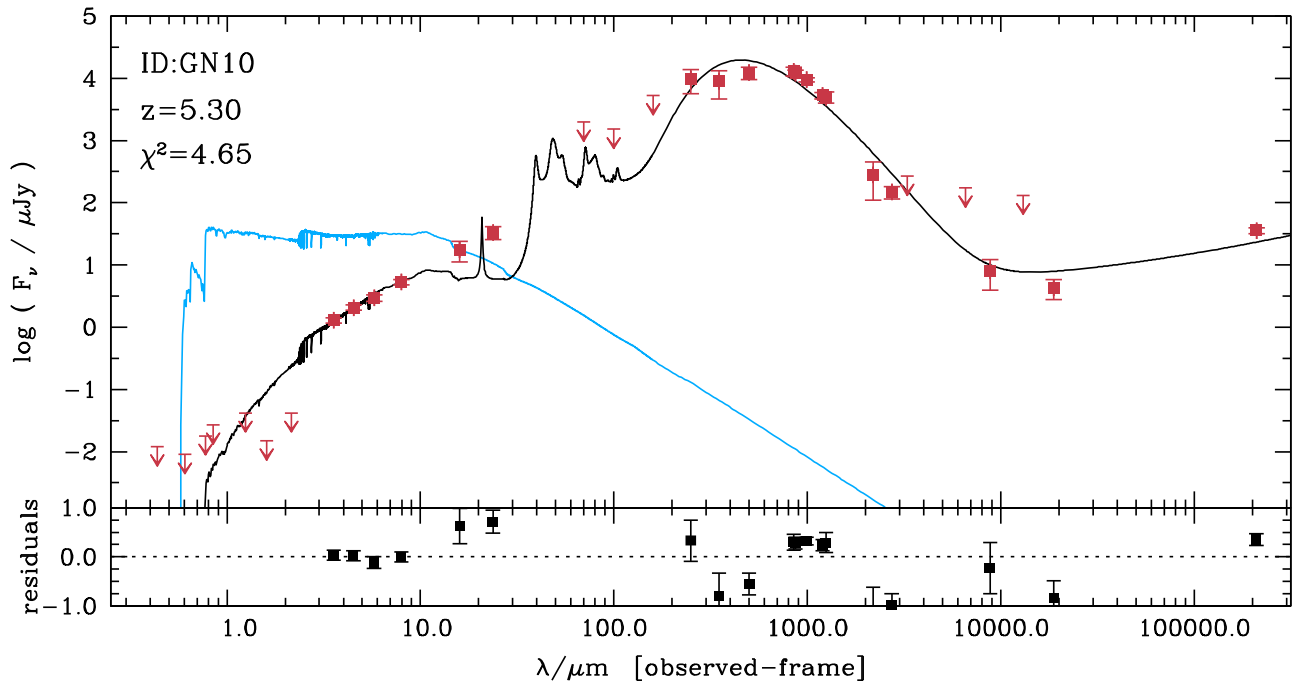
**Figure B1.** Spectral energy distribution of GN10 (top panel; red symbols), overlaid with the best-fit MAGPHYS model (black line) and unattenuated stellar light emission spectrum before dust reprocessing (blue line), and the residuals after subtracting the best-fit model (bottom panel).

**Table B1**
GN10 MAGPHYS SED Modeling Parameters

| Fit Parameter | Unit | Value[a] |
|---|---|---|
| $T_{\rm dust}$ | K | $41.7^{+5.0}_{-1.6}$ |
| $M_{\rm dust}$ | $10^9\,M_\odot$ | $0.58^{+0.06}_{-0.04}$ |
| $L_{\rm dust}$ | $10^{13}\,L_\odot$ | $1.26^{+0.15}_{-0.16}$ |
| $\mathrm{SFR}_{\rm total}$ | $M_\odot\,{\rm yr}^{-1}$ | $1020^{+150}_{-150}$ |
| $M_\star^e$ | $10^{11}\,M_\odot$ | $2.19^{+1.28}_{-0.93}$ |

**Note.**
[a] Median values are given. Lower and upper error bars are stated as the 16th and 84th percentiles, respectively.

## Appendix B
## GN10 MAGPHYS SED Fit

In addition to CIGALE, we have also used the MAGPHYS code (da Cunha et al. 2015) to fit the full optical to radio wavelength photometry of GN10. The fit to the spectral energy distribution is shown in Figure B1, and the resulting physical parameters are provided in Table B1. MAGPHYS suggests a dust luminosity $L_{\rm dust}$ that is ~25% higher than the $L_{\rm IR}$ found from MBB fitting but consistent within the uncertainties. It also finds a total SFR that is comparable to the $\mathrm{SFR}_{\rm IR}$ found from the MBB fit, consistent with the expectation that dust-obscured star formation dominates the SFR of GN10. $M_{\rm dust}$ is about half the value found from the MBB fit, and $T_{\rm dust}$ is ~20% lower (but consistent within the uncertainties). These differences are likely due to the fact that MAGPHYS uses multiple dust components in the fitting. In particular, $T_{\rm dust}$ corresponds to a luminosity-averaged value, calculated over multiple dust components. We adopt the values from the MBB fit in the main text to enable a more straight forward comparison to other $z > 5$ sources, for which similar methods were used. We also record these alternative values here to allow for comparison to other

samples modeled with MAGPHYS (e.g., da Cunha et al. 2015; Dudzevičiūtė et al. 2020; Simpson et al. 2020). MAGPHYS suggests approximately two times the $M_\star$ found by CIGALE. We adopt the value determined using CIGALE in the main text, as CIGALE provides a better fit to the break between 2.2 and 3.6 $\mu$m and to the 16–24 $\mu$m photometry.[70] We consider the two values to be consistent within the expected uncertainties in determining $M_\star$ for highly obscured $z > 5$ galaxies like GN10.

## Appendix C
## 1.2 mm Continuum Imaging of GN20.2a and b

As part of the NOEMA 1.2 mm observations of GN10 (project ID: T0B7; PI: Riechers), we also observed GN20.2a ($z = 4.0508$) and GN20.2b ($z = 4.0563$), two member galaxies of the GN20 proto-cluster environment (e.g., Daddi et al. 2009b; Hodge et al. 2013; Tan et al. 2014) in track sharing, leading to nearly the same amount of on-source time and $u - v$ coverage (8936 visibilities).[71] The pointing was centered between the two galaxies. From circular Gaussian fitting to the visibility data, we find primary beam-corrected 1.2 mm fluxes of $(3.85 \pm 0.71)$ and $(4.24 \pm 0.95)$ mJy and source diameters of $0\rlap{.}''21 \pm 0\rlap{.}''08$ and $0\rlap{.}''36 \pm 0\rlap{.}''09$ for GN20.2a[72] and b,[73] corresponding to surface areas of $(1.74 \pm 0.63)$ and $(5.06 \pm 1.24)\,{\rm kpc}^2$, respectively. The 1.2 mm fluxes thus correspond to source-averaged rest-

---

[70] We adopt the de-blended photometry throughout, but we caution that uncertainties due to de-blending are significant for photometry in the latter wavelength range. JWST will be critical for overcoming these uncertainties.
[71] We also observed GN20 ($z = 4.0553$) as part of this project in a second setup. Results from these data were reported by Hodge et al. (2015).
[72] Two-dimensional Gaussian fits suggest that GN20.2a is not resolved along its minor axis ($<0\rlap{.}''11$, or $<0.8$ kpc), with a best-fit major axis diameter of $0\rlap{.}''30$ (2.1 kpc), but the fit does not converge well. As such, this estimate is considered to be a weak constraint at best.
[73] For GN20.2b, a two-dimensional Gaussian fit suggests a size of $(0\rlap{.}''42 \pm 0\rlap{.}''11) \times (0\rlap{.}''28 \pm 0\rlap{.}''14)$, or $(3.0 \pm 0.8) \times (2.0 \pm 1.0)\,{\rm kpc}^2$.
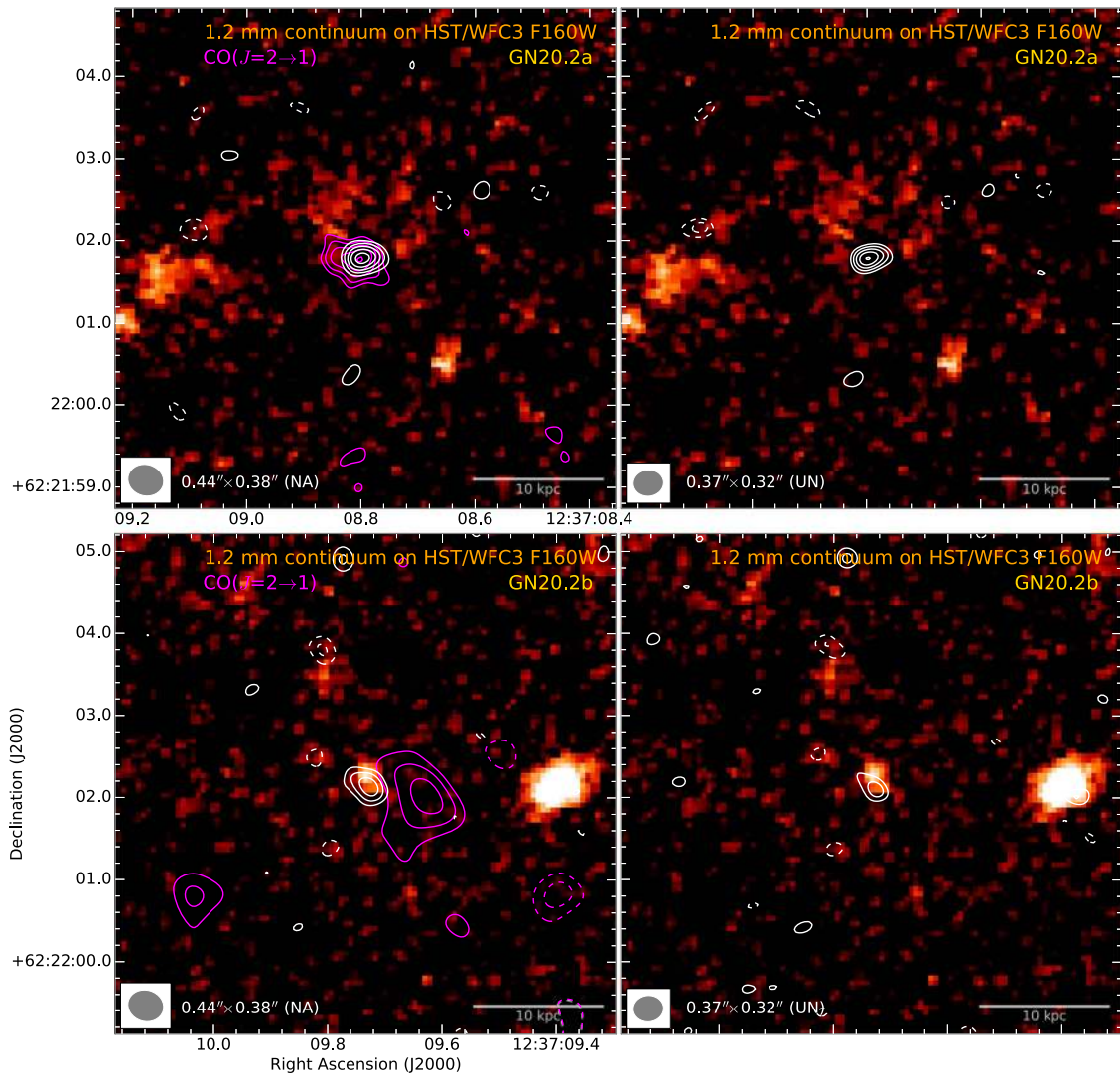
**Figure C1.** Rest-frame FIR continuum contour maps at an observed-frame wavelength of 1.2 mm overlaid on an HST/WFC3 F160W continuum image toward GN20.2a (top panels) and GN20.2b (bottom panels). Contours start at $\pm 3\sigma$, and they are shown in steps of $1\sigma = 0.35$ (left panels; imaged using natural baseline weighting) and 0.41 mJy beam$^{-1}$ (right panels; imaged using uniform weighting), respectively. In the left panels, magenta CO($J = 2 \rightarrow 1$) contours tapered to $0\rlap{.}''38$ (GN20.2a) and $0\rlap{.}''77$ (GN20.2b; Hodge et al. 2013) resolution are shown for comparison. The contour steps are the same, where $1\sigma = 20$ and 28 $\mu$Jy beam$^{-1}$ for GN20.2a and b, respectively. The synthesized beam size for the 1.2 mm observations is indicated in the bottom left corner of each panel.

frame brightness temperatures of $T_b = (8.5 \pm 1.9)$ and $(3.2 \pm 0.7)$ K, respectively. These modest values suggest that both sources have significant substructures on scales below the resolution of our observations. Both sources thus appear marginally resolved by our observations (Figure C1).

Using the infrared luminosities measured by Tan et al. (2014), we find infrared luminosity surface densities of $\Sigma_{IR} = (2.6 \pm 1.0)$ and $(0.8 \pm 0.2) \times 10^{12} L_\odot$ kpc$^{-2}$ and SFR surface densities of $\Sigma_{SFR} = (260 \pm 100)$ and $(80 \pm 20)$ $M_\odot$ yr$^{-1}$ kpc$^{-2}$ for GN20.2a and b, respectively. This suggests that the star formation activity in GN20.2b is almost as intense as that in the central region of GN20 ($\Sigma_{SFR} = (120 \pm 10) M_\odot$ yr$^{-1}$ kpc$^{-2,\text{hodge15}}$), while GN20.2a appears to be a more intense starburst, approaching the activity level of "maximum starbursts".

The dust continuum emission in GN20.2a appears to be more compact than the CO($J = 2 \rightarrow 1$) emission imaged by Hodge et al. (2013), which has an extent of $(0\rlap{.}''7 \pm 0\rlap{.}''1) \times (0\rlap{.}''4 \pm 0\rlap{.}''1)$. The dust and cold molecular

gas emissions appear to peak at the same position, such that the rest-frame 237 $\mu$m luminosity associated with the intense starburst is likely dominantly emerging from the regions containing the highest-density gas. The dust emission in GN20.2b also appears to be more compact than the CO($J = 2 \rightarrow 1$) emission, which has an extent of $(1\rlap{.}''1 \pm 0\rlap{.}''4) \times (0\rlap{.}''7 \pm 0\rlap{.}''4)$ as measured by Hodge et al. (2013). Interestingly, the gas and dust emissions appear to be spatially offset by $<1''$, with the dust emission peaking much closer to the likely near-infrared counterpart of the dusty galaxy. This may indicate the presence of multiple galaxy components, where the brightest CO-emitting component identified by Hodge et al. (2013) is not the same as that dominating the dust emission and stellar light. Another, perhaps less likely possibility is that the dust-emitting component is not at the redshift of the GN20 proto-cluster. On the other hand, the CO($J = 6 \rightarrow 5$) emission appears to peak at a position that is more consistent with the 1.2 mm dust continuum peak and the stellar light, albeit observed at about a

two-times-lower linear spatial resolution (Tan et al. 2014). More sensitive CO observations are required to further investigate the nature of this offset.

## ORCID iDs

Dominik A. Riechers  https://orcid.org/0000-0001-9585-1462
Jacqueline A. Hodge  https://orcid.org/0000-0001-6586-8845
Riccardo Pavesi  https://orcid.org/0000-0002-2263-646X
Emanuele Daddi  https://orcid.org/0000-0002-3331-9590
Roberto Decarli  https://orcid.org/0000-0002-2662-8803
Rob J. Ivison  https://orcid.org/0000-0001-5118-1313
Chelsea E. Sharon  https://orcid.org/0000-0002-6250-5608
Ian Smail  https://orcid.org/0000-0003-3037-257X
Fabian Walter  https://orcid.org/0000-0003-4793-7880
Manuel Aravena  https://orcid.org/0000-0002-6290-3198
Peter L. Capak  https://orcid.org/0000-0003-3578-6843
Christopher L. Carilli  https://orcid.org/0000-0001-6647-3861
Elisabete da Cunha  https://orcid.org/0000-0001-9759-4797
Helmut Dannerbauer  https://orcid.org/0000-0001-7147-3575
Mark Dickinson  https://orcid.org/0000-0001-5414-5131
Roberto Neri  https://orcid.org/0000-0002-7176-4046

## References

Andreani, P., Cimatti, A., Loinard, L., & Röttgering, H. 2000, A&A, 354, L1
Andrews, B. H., & Thompson, T. A. 2011, ApJ, 727, 97
Aravena, M., Younger, J. D., Fazio, G. G., et al. 2010, ApJL, 719, L15
Asboth, V., Conley, A., Sayers, J., et al. 2016, MNRAS, 462, 1989
Bennett, C. L., Larson, D., Weiland, J. L., & Hinshaw, G. 2014, ApJ, 794, 135
Bertoldi, F., Carilli, C., Aravena, M., et al. 2007, ApJS, 172, 132
Béthermin, M., De Breuck, C., Sargent, M., & Daddi, E. 2015, A&A, 576, L9
Béthermin, M., Wu, H.-Y., Lagache, G., et al. 2017, A&A, 607, A89
Blain, A. W., Barnard, V. E., & Chapman, S. C. 2003, MNRAS, 338, 733
Blain, A. W., Smail, I., Ivison, R. J., Kneib, J.-P., & Frayer, D. T. 2002, PhR, 369, 111
Bolatto, A. D., Chatterjee, S., Casey, C. M., et al. 2017, arXiv:1711.09960
Bolatto, A. D., Wolfire, M., & Leroy, A. K. 2013, ARA&A, 51, 207
Bothwell, M. S., Smail, I., Chapman, S. C., et al. 2013, MNRAS, 429, 3047
Brisbin, D., Miettinen, O., Aravena, M., et al. 2017, A&A, 608, A15
Buchner, J., Georgakakis, A., Nandra, K., et al. 2014, A&A, 564, A125
Calabrò, A., Daddi, E., Puglisi, A., et al. 2019, A&A, 623, A64
Calzetti, D. 2001, PASP, 113, 1449
Capak, P., Carilli, C. L., Lee, N., et al. 2008, ApJL, 681, L53
Capak, P. L., Riechers, D., Scoville, N. Z., et al. 2011, Natur, 470, 233
Carilli, C. L., Daddi, E., Riechers, D., et al. 2010, ApJ, 714, 1407
Carilli, C. L., & Walter, F. 2013, ARA&A, 51, 105
Casey, C. M., Narayanan, D., & Cooray, A. 2014, PhR, 541, 45
Casey, C. M., Zavala, J. A., Spilker, J., et al. 2018, ApJ, 862, 77
Chabrier, G. 2003, PASP, 115, 763
Chapman, S. C., Blain, A. W., Smail, I., & Ivison, R. J. 2005, ApJ, 622, 772
Cooke, E. A., Smail, I., Swinbank, A. M., et al. 2018, ApJ, 861, 100
Coppin, K. E. K., Chapman, S. C., Smail, I., et al. 2010, MNRAS, 407, L103
Cowie, L. L., Barger, A. J., Wang, W.-H., & Williams, J. P. 2009, ApJL, 697, L122
Cox, P., Krips, M., Neri, R., et al. 2011, ApJ, 740, 63
da Cunha, E., Groves, B., Walter, F., et al. 2013, ApJ, 766, 13
da Cunha, E., Walter, F., Smail, I. R., et al. 2015, ApJ, 806, 110
Daddi, E., Dannerbauer, H., Krips, M., et al. 2009a, ApJL, 695, L176
Daddi, E., Dannerbauer, H., Liu, D., et al. 2015, A&A, 577, A46
Daddi, E., Dannerbauer, H., Stern, D., et al. 2009b, ApJ, 694, 1517
Danielson, A. L. R., Swinbank, A. M., Smail, I., et al. 2011, MNRAS, 410, 1687
Danielson, A. L. R., Swinbank, A. M., Smail, I., et al. 2017, ApJ, 840, 78
Dannerbauer, H., Lehnert, M. D., Lutz, D., et al. 2002, ApJ, 573, 473
Dannerbauer, H., Lehnert, M. D., Lutz, D., et al. 2004, ApJ, 606, 664
Dannerbauer, H., Walter, F., & Morrison, G. 2008, ApJL, 673, L127
Davis, T. A., Alatalo, K., Bureau, M., et al. 2013, MNRAS, 429, 534
Decarli, R., Walter, F., Carilli, C., et al. 2014, ApJ, 782, 78
Dickinson, M. & GOODS Team 2004, BAAS, 36, 1614
Dowell, C. D., Conley, A., Glenn, J., et al. 2014, ApJ, 780, 75
Downes, D., Neri, R., Greve, A., et al. 1999, A&A, 347, 809
Dudzevičiūtė, U., Smail, I., Swinbank, A. M., et al. 2020, MNRAS, 494, 3828
Duivenvoorden, S., Oliver, S., Scudder, J. M., et al. 2018, MNRAS, 477, 1099
Dunne, L., Eales, S. A., & Edmunds, M. G. 2003, MNRAS, 341, 589
Engel, H., Tacconi, L. J., Davies, R. I., et al. 2010, ApJ, 724, 233
Feroz, F., Hobson, M. P., & Bridges, M. 2009, MNRAS, 398, 1601
Flower, D. R. 2001, JPhB, 34, 2731
Foreman-Mackey, D., Hogg, D. W., Lang, D., & Goodman, J. 2013, PASP, 125, 306
Franco, M., Elbaz, D., Béthermin, M., et al. 2018, A&A, 620, A152
Frayer, D. T., Reddy, N. A., Armus, L., et al. 2004, AJ, 127, 728
Fudamoto, Y., Ivison, R. J., Oteo, I., et al. 2017, MNRAS, 472, 2028
Giavalisco, M., Ferguson, H. C., Koekemoer, A. M., et al. 2004, ApJL, 600, L93
Graciá-Carpio, J., Sturm, E., Hailey-Dunsheath, S., et al. 2011, ApJL, 728, L7
Greve, T. R., Bertoldi, F., Smail, I., et al. 2005, MNRAS, 359, 1165
Grogin, N. A., Kocevski, D. D., Faber, S. M., et al. 2011, ApJS, 197, 35
Gullberg, B., Smail, I., Swinbank, A. M., et al. 2019, MNRAS, 490, 4956
Güsten, R., Philipp, S. D., Weiß, A., & Klein, B. 2006, A&A, 454, L115
Hodge, J. A., Carilli, C. L., Walter, F., Daddi, E., & Riechers, D. 2013, ApJ, 776, 22
Hodge, J. A., Riechers, D., Decarli, R., et al. 2015, ApJL, 798, L18
Hodge, J. A., Smail, I., Walter, F., et al. 2019, ApJ, 876, 130
Hodge, J. A., Swinbank, A. M., Simpson, J. M., et al. 2016, ApJ, 833, 103
Hughes, D. H., Serjeant, S., Dunlop, J., et al. 1998, Natur, 394, 241
Ivison, R. J., Lewis, A. J. R., Weiss, A., et al. 2016, ApJ, 832, 78
Ivison, R. J., Papadopoulos, P. P., Smail, I., et al. 2011, MNRAS, 412, 1913
Jin, S., Daddi, E., Magdis, G. E., et al. 2019, ApJ, 887, 144
Kennicutt, R. C. J. 1998, ApJ, 498, 541
Laird, E. S., Nandra, K., Pope, A., & Scott, D. 2010, MNRAS, 401, 2763
Liu, D., Daddi, E., Dickinson, M., et al. 2018, ApJ, 853, 172
Liu, D., Gao, Y., Isaak, K., et al. 2015, ApJL, 810, L14
Magdis, G. E., Daddi, E., Elbaz, D., et al. 2011, ApJL, 740, L15
Magnelli, B., Karim, A., Staguhn, J., et al. 2019, ApJ, 877, 45
Magnelli, B., Lutz, D., Saintonge, A., et al. 2014, A&A, 561, A86
Miettinen, O., Delvecchio, I., Smolčić, V., et al. 2017, A&A, 606, A17
Miller, T. B., Chapman, S. C., Aravena, M., et al. 2018, Natur, 556, 469
Neri, R., Downes, D., Cox, P., & Walter, F. 2014, A&A, 562, A35
Nguyen, H. T., Schulz, B., Levenson, L., et al. 2010, A&A, 518, L5
Noll, S., Burgarella, D., Giovannoli, E., et al. 2009, A&A, 507, 1793
Oteo, I., Ivison, R. J., Dunne, L., et al. 2018, ApJ, 856, 72
Oteo, I., Ivison, R. J., Negrello, M., et al. 2017a, arXiv:1709.04191
Oteo, I., Zhang, Z.-Y., Yang, C., et al. 2017b, ApJ, 850, 170
Pavesi, R., Riechers, D. A., Capak, P. L., et al. 2016, ApJ, 832, 151
Pavesi, R., Riechers, D. A., Faisst, A. L., Stacey, G. J., & Capak, P. L. 2019, ApJ, 882, 168
Pavesi, R., Riechers, D. A., Sharon, C. E., et al. 2018a, ApJ, 861, 43
Pavesi, R., Sharon, C. E., Riechers, D. A., et al. 2018b, ApJ, 864, 49
Pope, A., Borys, C., Scott, D., et al. 2005, MNRAS, 358, 149
Pope, A., Scott, D., Dickinson, M., et al. 2006, MNRAS, 370, 1185
Ranalli, P., Comastri, A., & Setti, G. 2003, A&A, 399, 39
Rawle, T. D., Egami, E., Bussmann, R. S., et al. 2014, ApJ, 783, 59
Riechers, D. A. 2011, ApJ, 730, 108
Riechers, D. A., Bradford, C. M., Clements, D. L., et al. 2013, Natur, 496, 329
Riechers, D. A., Capak, P. L., Carilli, C. L., et al. 2010, ApJL, 720, L131
Riechers, D. A., Carilli, C. L., Capak, P. L., et al. 2014a, ApJ, 796, 84
Riechers, D. A., Carilli, L. C., Walter, F., et al. 2011a, ApJL, 733, L11
Riechers, D. A., Cooray, A., Omont, A., et al. 2011b, ApJL, 733, L12
Riechers, D. A., Hodge, J., Walter, F., Carilli, C. L., & Bertoldi, F. 2011c, ApJL, 739, L31
Riechers, D. A., Leung, T. K. D., Ivison, R. J., et al. 2017, ApJ, 850, 1
Riechers, D. A., Pavesi, R., Sharon, C. E., et al. 2019, ApJ, 872, 7
Riechers, D. A., Pope, A., Daddi, E., et al. 2014b, ApJ, 786, 31
Riechers, D. A., Walter, F., Carilli, C. L., et al. 2006, ApJ, 650, 604
Riechers, D. A., Walter, F., Carilli, C. L., & Bertoldi, F. 2007, ApJL, 671, L13
Rivera, G. C., Hodge, J. A., Smail, I., et al. 2018, ApJ, 863, 56
Robson, E. I., Ivison, R. J., Smail, I., et al. 2014, ApJ, 793, 11
Salomé, P., Guélin, M., Downes, D., et al. 2012, A&A, 545, A57
Schreiber, C., Elbaz, D., Pannella, M., et al. 2018, A&A, 609, A30
Scott, K. S., Austermann, J. E., Perera, T. A., et al. 2008, MNRAS, 385, 2225
Serra, P., Amblard, A., Temi, P., et al. 2011, ApJ, 740, 22

Silva, L., Granato, G. L., Bressan, A., & Danese, L. 1998, ApJ, 509, 103
Simpson, J. M., Smail, I., Dudzeviciute, U., et al. 2020, arXiv:2003.05484
Simpson, J. M., Smail, I., Swinbank, A. M., et al. 2015, ApJ, 799, 81
Simpson, J. M., Smail, I., Swinbank, A. M., et al. 2017, ApJ, 839, 58
Simpson, J. M., Swinbank, A. M., Smail, I., et al. 2014, ApJ, 788, 125
Smolčić, V., Aravena, M., Navarrete, F., et al. 2012, A&A, 548, A4
Smolčić, V., Miettinen, O., Tomičić, N., et al. 2017, A&A, 597, A4
Stacey, G. J., Geis, N., Genzel, R., et al. 1991, ApJ, 373, 423
Stacey, G. J., Hailey-Dunsheath, S., Ferkinhoff, C., et al. 2010, ApJ, 724, 957
Stach, S. M., Smail, I., Swinbank, A. M., et al. 2018, ApJ, 860, 161
Staguhn, J. G., Kovács, A., Arendt, R. G., et al. 2014, ApJ, 790, 77
Strandet, M. L., Weiss, A., De Breuck, C., et al. 2017, ApJL, 842, L15
Strandet, M. L., Weiss, A., Vieira, J. D., et al. 2016, ApJ, 822, 80
Swinbank, A. M., Simpson, J. M., Smail, I., et al. 2014, MNRAS, 438, 1267
Tamura, Y., Mawatari, K., Hashimoto, T., et al. 2019, ApJ, 874, 27
Tan, Q., Daddi, E., Magdis, G., et al. 2014, A&A, 569, A98
Thompson, T. A., Quataert, E., & Murray, N. 2005, ApJ, 630, 167
Toft, S., Smolčić, V., Magnelli, B., et al. 2014, ApJ, 782, 68
Vieira, J. D., Crawford, T. M., Switzer, E. R., et al. 2010, ApJ, 719, 763
Wagg, J., Hughes, D. H., Aretxaga, I., et al. 2007, MNRAS, 375, 745
Walter, F., Decarli, R., Carilli, C., et al. 2012, Natur, 486, 233
Wang, W.-H., Barger, A. J., & Cowie, L. L. 2009, ApJ, 690, 319
Wang, W.-H., Cowie, L. L., van Saders, J., Barger, A. J., & Williams, J. P. 2007, ApJL, 670, L89
Weiß, A., De Breuck, C., Marrone, D. P., et al. 2013, ApJ, 767, 88
Weiß, A., Downes, D., Neri, R., et al. 2007, A&A, 467, 955
Weiß, A., Downes, D., Walter, F., & Henkel, C. 2005a, A&A, 440, L45
Weiß, A., Ivison, R. J., Downes, D., et al. 2009, ApJL, 705, L45
Weiß, A., Walter, F., & Scoville, N. Z. 2005b, A&A, 438, 533
Wilson, C. D., Petitpas, G. R., Iono, D., et al. 2008, ApJS, 178, 189
Younger, J. D., Fazio, G. G., Huang, J.-S., et al. 2007, ApJ, 671, 1531
Zavala, J. A., Montaña, A., Hughes, D. H., et al. 2018, NatAs, 2, 56
Zhang, Z.-Y., Papadopoulos, P. P., Ivison, R. J., et al. 2016, RSOS, 3, 160025